

# **Coupling Textural, Magnetic, and Modeling Techniques to Understand Precambrian Paleoenvironments**

Thesis by  
Sarah Pearl Slotznick

In Partial Fulfillment of the Requirements for  
the degree of  
Doctor of Philosophy



CALIFORNIA INSTITUTE OF TECHNOLOGY  
Pasadena, California

2016  
(Defended May 19, 2016)

© 2016

Sarah Pearl Slotznick



## ACKNOWLEDGEMENTS

First and foremost, I would like to thank my advisors Woody Fischer and Joe Kirschvink for their intellectual guidance through my graduate school career. Woody helped me develop these projects through formative discussions, was always available for a quick chat when large or small questions popped up, and always made certain I remembered the forest, not simply the trees. Joe encouraged me to explore my interests wherever they took me, gave me free rein of his laboratory, and helped develop other important academic skills, in addition to research, by encouraging my teaching and mentoring of undergraduate researchers, visitors, and Ge124b students.

I would also like to acknowledge the many collaborators and co-authors who aided me during the projects detailed in this dissertation. Don Winston, Jerry Zieg, and John Grotzinger facilitated my exploration of the Belt Supergroup, and shared their detailed knowledge of the region in the field from years of work in Montana, without which this work would not have been possible. Sam Webb allowed me to be one of the first users on his new beamline and promptly answered my numerous questions whether they be frantic texts for troubleshooting at midnight or analysis concerns weeks later. Mike Jackson and Bruce Moskowitz at the Institute for Rock Magnetism taught me how to handle the MPMS and VSM as well as aiding me substantially in data interpretation. John Eiler taught me that all rocks are metamorphic.

This dissertation required four field seasons in Montana, and my field assistants filled incredibly important roles. Tim Lyons and UCR students helped me initially explore the geology of Glacier National Park from an academic viewpoint. The 2013 Agouron Field Course participants, especially JC Creveling and Ted Present, tolerated long drives and monotonous metamorphosed rocks to help me complete a 275 mile sampling transect across western Montana as well as providing intellectual conversations that aided my critical thinking about the Belt Supergroup. Austin Chadwick and Steven Skinner provided tremendous aid

hauling rocks while climbing mountains, often the same mountain over and over again, while remaining cheerful and ready to discuss new field observations. I'd like to thank Tess Puig, Kathy Lima, Julie Lee, Alice Oh, Jennifer Leonardini, Janice Grancich, Lisa Christiansen, Heather Steele, Mark Garcia, Chi Ma, Yunbin Guan, Dian Buchness, Liz Boyd, and Marcia Hudson for their administrative and technical support helping these field seasons and research projects happen as well as guiding me through my graduate school years.

Alex Sessions, my academic advisor, helped guide me through the challenges of required classes. I had several mentors in my first few years here at Caltech who helped steer my trajectory as a graduate student, including Lauren Edgar, June Wicks, Daniel Stolper, Anne Dekas, Maggie Osborne, and Katie Snell. Lab group members Kristin Bergmann, Jena Johnson, Lewis Ward, Jim Hemp, Kyle Bradley, Usha Lingappa, Lizzy Trower, Joe "Vinny" Biasi, and Jennifer Buz continuously showed me new exciting research in the broad field of Geobiology, helped provide isotopic support for my work, kept me company at the synchrotron and through the analysis process, and constantly troubleshooted issues with the ultra-high resolution scanning SQUID magnetic microscope to keep it running.

My first-year pit crew—Stephen Cox, Morgan Raven, Elizabeth Trembath-Reichert, David Case, Jeff Prancevic, Jena Johnson—kept me company during the challenging first year and in the equally challenging years that followed. Kirsten Siebach, my officemate, dealt with my less-than-neat organization methods, was always willing to help me make decisions, even insignificant ones, and commiserated with me through the past 2 months while working on our theses. Alison Piasecki, Giuliana Viglione, Frank Sousa, Jason Price, Sean Mullin, and many others in the division provided much-needed office visits and traveled with me to explore the regional geology of the southwestern United States.

My friends outside of the GPS Division—first-year cohort Aero-ME-BioChem, EXPLiCIT, Bookclub, Material Science, GHC, 157<sup>th</sup>—have made my

time here at Caltech much more enjoyable by providing much needed breaks from research. My roommates—Jackie Villadsen, Sunita Darbe, and Chengyun Hau—and my boyfriend Steven Skinner played a vital role in keeping me optimistic and happy throughout my time in graduate school by always being available during tough times, no matter the time of day. Lastly, I'd like to thank my family for their continuous support of my geologic career; from encouraging my scientific interests at a young age, giving me an appreciation for travel and exploration, supporting me through my 25-year student career, and even proof-reading this thesis, they have always been there for me.

## ABSTRACT

The oxygenation of our planet is perhaps the greatest transition in its history, dramatically affecting geochemical cycles and the evolution of life. Major first-order questions still remain about late Archean and Proterozoic environments, even as newly developed geochemical techniques provide additional constraints and create subtle conundrums. I apply a new approach to classic localities to understand Precambrian redox character and paleoenvironmental conditions by combining textural observations from optical and electron microscopy, isotopic measurements, and (synchrotron-based) x-ray spectroscopy with scanning magnetic microscopy and bulk rock magnetic experiments. Models paired with data from the literature provide additional context for these measurement results.

The first portion of this dissertation focuses on understanding the predominant microbial metabolism recorded in the 2.72 Ga Tumbiana Formation stromatolites. I proposed that these stromatolites formed in shallow, anoxic waters and record a global signature of unique autotrophy distinct from younger systems dominated by oxygenic photosynthesis. The next portion of this dissertation uses the redox sensitivity of iron as a tool to investigate paleoredox conditions of the 1.45 Ga lower Belt Supergroup during a potentially transitional time-period in surface environments. Observations of primary mineralogy in early diagenetic pyrite and detrital iron oxides suggest an oxygenated water-column overlying anoxic, sulfidic pore-fluids very similar to the modern. The final portion of this dissertation assesses the effects of prevalent secondary overprints on the use of iron as a paleoredox proxy. Theoretical data-driven models combined with trends from the Belt Supergroup highlight the mobility of iron during progressive burial metamorphism as well as in diagenetic transformations and reactions with infiltrating fluids. Applying coupled techniques, specifically including textural methods, is vital for untangling

secondary alterations from primary records of environmental conditions during the Precambrian.

**PUBLISHED CONTENT AND CONTRIBUTIONS**

Slotznick, S. P., and Fischer, W. W., 2016, Examining Archean methanotrophy: Earth and Planetary Science Letters, v. 441, p. 52-59. doi: 10.1016/j.epsl.2016.02.013

S.P.S. participated in development of the project, made petrographic observations, prepared samples, interpreted results, constructed the model, and wrote much of the manuscript.

Slotznick, S. P., Zieg, J., Webb, S. M., Kirschvink, J. L., and Fischer, W. W., 2015, Iron Mineralogy and Redox Chemistry of the Mesoproterozoic Newland Formation in the Helena Embayment, Belt Supergroup, Montana: Northwest Geology, v. 44, p. 55-72.

S.P.S. participated in conception of the project, collected samples from Montana, measured samples using coupled techniques, analyzed data, interpreted results, and wrote much of the manuscript.

Slotznick, S. P., Winston, D., Webb, S. M., Kirschvink, J. L., and Fischer, W. W., 2016, Iron mineralogy and redox conditions during deposition of the Mid-Proterozoic Appekunny Formation, Belt Supergroup, Glacier National Park: Geological Society of America Special Papers, v. 522, doi: 10.1130/2016.2522(09).

S.P.S. participated in conception of the project, collected samples from Montana, made field observations, measured stratigraphic sections, measured samples using coupled techniques, analyzed data, interpreted results, and wrote much of the manuscript.

## TABLE OF CONTENTS

Acknowledgements.....	iii
Abstract .....	vi
Published Content and Contributions.....	viii
Table of Contents.....	ix
List of Tables .....	xii
List of Figures.....	xiii
 Chapter 1: Introduction.....	 1
1.1 Background.....	2
1.2 Dissertation Summary .....	3
1.3 Figures .....	8
1.4 References .....	9
 Chapter 2: Examining Archean Methanotrophy .....	 17
2.1 Abstract.....	18
2.2 Introduction .....	18
2.3 Geological background and methods.....	21
2.4 Results .....	24
2.5 Results in context of Archean carbonate chemistry .....	27
2.6 Alternative Carbon Fixation Pathways .....	29
2.7 Acknowledgements .....	31
2.8 Figures .....	32
2.9 Supplemental Tables .....	36
2.10 Supplemental Figures.....	38
2.11 References .....	43
 Chapter 3: Iron Mineralogy and Redox Chemistry of the Mesoproterozoic Newland Formation in the Helena Embayment, Belt Supergroup, MT .....	 52
3.1 Introduction .....	53
3.2 Geologic Setting.....	56
3.2.1 Black Butte Deposit .....	57
3.3 Methods .....	58
3.4 Results .....	60
3.4.1 Rotational Remanent Magnetization (RRM).....	60
3.4.2 Coercivity of Remanence Acquisition.....	61
3.4.3 Lowrie-Fuller Test .....	62
3.4.4 Fuller Test of NRM.....	63
3.4.5 KappaBridge Thermal Susceptibility .....	63
3.4.2 X-ray Spectroscopy.....	64
3.5 Discussion and Conclusions.....	65
3.6 Acknowledgements .....	67
3.7 Tables.....	69

3.8 Figures .....	71
3.9 References .....	80
Chapter 4: Iron Mineralogy and Redox Conditions During the Deposition of the Mid-Proterozoic Appekunny Formation, Belt Supergroup,	
Glacier National Park .....	87
4.1 Abstract.....	88
4.2 Introduction .....	88
4.3 Geologic Setting.....	92
4.4 Sample Descriptions and Field Relationships .....	95
4.5 Sampling Analytical Methods.....	102
4.6 Results .....	104
4.7 Discussion.....	111
4.8 Conclusion.....	117
4.9 Acknowledgements .....	118
4.10 Tables.....	119
4.11 Figures .....	121
4.12 Supplemental Tables .....	134
4.13 References .....	135
Chapter 5: Iron Mineralogy, Secondary Overprints, and Paleoredox Conditions During Deposition of the Mid-Proterozoic Belt Supergroup.....	
5.1 Abstract.....	148
5.2 Introduction .....	148
5.3 Geology of the Belt Supergroup .....	150
5.4 Coupled Textural and Bulk Methods.....	151
5.5 Metamorphic Transformations and Diagenetic Overprints.....	153
5.6 Primary Mineralogy and Paleoredox .....	158
5.7 Concluding Remarks .....	161
5.8 Acknowledgements .....	163
5.9 Figures .....	164
5.10 Supplemental Tables .....	170
5.11 Supplemental Figures.....	179
5.12 References .....	209
Chapter 6: How Metamorphism Affects Iron Mineralogy and the Iron Speciation Redox Proxy: a Data-Driven Theoretical Study .....	
6.1 Abstract.....	220
6.2 Introduction .....	221
6.3 Background.....	222
6.3.1 Development of the Iron Speciation Proxy .....	222
6.3.2 Sequential Extraction Pools .....	225
6.3.3 Previous Adjustments and Models for Metamorphism.....	226
6.4 Approach .....	227
6.4.1 Locality Selection.....	227



6.4.1.1 Waits River and Gile Mountain Fms., Vermont .....	228
6.4.1.2 Waterville and Sangerville-Vassalboro Fms., Maine .....	230
6.4.2 Model.....	231
6.5 Case Example Results and Discussion .....	233
6.5.1 Pyrrhotite Pool Placement.....	233
6.5.2 Lithological Controls and Diagenesis.....	234
6.5.3 Increasing Grade and Metamorphic Reactions.....	236
6.6 Conclusions .....	241
6.7 Acknowledgements .....	242
6.8 Tables.....	243
6.9 Figures .....	247
6.10 Supplemental Figures.....	258
6.11 References .....	262

## LIST OF TABLES

S2.1 Carbon Isotopic Signatures From Phanerozoic AOM Sites.....	36
S2.2 Isotopic Data From the Tumbiana Formation .....	37
3.1 Detailed Sample Data.....	69
3.2 Minerals in Black Butte Deposit Newland Formation Samples .....	70
4.1 Mineral Identifications .....	119
4.2 Elemental Abundances from XRF Microprobe.....	120
S4.1 Detailed Sample Data for Glacier National Park Samples.....	134
S5.1 Detailed Sample Data for Belt Supergroup Samples .....	170
S5.2 Mineralogy of Samples from the Belt Supergroup .....	172
S5.3 Mineral Compositions of Select Samples.....	175
S5.4 Elemental Abundances from XRF Microprobe.....	177
S5.5 Hysteresis Parameters and Calculated Magnetite Content.....	178
6.1 Sequential Extraction Methods and Targeted Minerals .....	243
6.2 Minerals identified in the Maine and Vermont Formations .....	244
6.3 Example Metamorphic Reactions .....	245

## LIST OF FIGURES

1.1 Redox Conditions and Evolution from Rock Record.....	8
2.1 Geologic Map of Tumbiana Formation Outcrops .....	32
2.2 Stromatolite Petrography .....	33
2.3 Carbon, Oxygen, and Clumped Isotope Data .....	34
2.4 C Isotope and Carbonate Chemistry Model.....	35
S2.1 Stratigraphic Column at Study Locality .....	38
S2.2 Additional Stromatolite Petrography .....	39
S2.3 Secondary Iron Oxides in Microscopy and UHRSSM .....	40
S2.4 Carbonate Chemistry Model of Saturation State.....	42
3.1 Regional and Geologic Map with General Stratigraphy .....	71
3.2 Stratigraphic Columns of Black Butte Deposit Drill Cores .....	72
3.3 Rock Magnetic Data from Newland Formation Shales.....	73
3.4 UHRSSM Images and Multiple Energy S XRF maps .....	74
3.5 KappaBridge results for a Representative Sample .....	76
3.6 Synchrotron S K-Edge XANES Spectra.....	77
3.7 High-Energy XRF Maps of Metal Abundances .....	78
4.1 Mapped Sampling Localities and General Stratigraphy.....	121
4.2 Stratigraphic Columns of the Appekunny Formation .....	123
4.3 Photographs of Appekunny Formation Lithotypes .....	125
4.4 Bulk Rock Magnetic Techniques.....	127
4.5 Synchrotron S and Fe XANES Spectra and EDS spectra .....	129
4.6 XRF Maps of Elemental Abundance .....	131
4.7 Backscatter Electron and Scanning Electron Images .....	132
5.1 Map with Sample Localities, Iron Mineralog, and Isograds .....	164
5.2 Belt Stratigraphy.....	165
5.3 Images of Textures from Lower Belt Samples .....	166
5.4 Detailed Textural Analysis of GP12-8.....	167
5.5 Rock Magnetic Measurements.....	168
S5.1 Photographs of Lower Belt Outcrops .....	179
S5.2 Coercivity of Remanence Spectra and RRM .....	181

S5.3 Additional MPMS Measurements .....	183
S5.4 Example Hysteresis Loops.....	185
S5.5 End-Member S XANES Spectra .....	187
S5.6 High-Energy XRF Maps for East Glacier National Park.....	189
S5.7 High-Energy XRF Maps for West Glacier National Park .....	191
S5.8 High-Energy XRF Maps for Helena Embayment .....	193
S5.9 High-Energy XRF Maps for Prichard Formation .....	194
S5.10 Detailed Textural Analysis of BS13-2.....	195
S5.11 Detailed Textural Analysis of GP12-1 .....	197
S5.12 Detailed Textural Analysis of GP14-32 .....	199
S5.13 Additional Textural Analyses of GP12-8 .....	200
S5.14 Detailed Textural Analysis of GP14-6 .....	201
S5.15 Detailed Textural Analysis of GP14-27 .....	202
S5.16 Detailed Textural Analysis of BS13-37.....	203
S5.17 Detailed Textural Analysis of PP13-11 and BS13-39.....	204
S5.18 Detailed Textural Analysis of BS13-31.....	206
S5.19 Textures in Black Butte Newland Formation Samples .....	208
6.1 Iron Speciation Cross Plot.....	247
6.2 Bar Graph of Paper Using Iron Speciation .....	248
6.3 Waits River and Gile Mtn Fms. in Iron Speciation Crossplot.....	249
6.4 Waits River and Gile Mtn Fms. Detailed $Fe_{HR}/Fe_T$ .....	250
6.5 Waits River and Gile Mtn Fms. Detailed $Fe_{py}/Fe_{HR}$ .....	251
6.6 Waterville and Sangerville-Vassalboro Frms. in Crossplot .....	252
6.7 Waterville and Sangerville-Vassalboro Frms. Detailed $Fe_{HR}/Fe_T$ .....	253
6.8 Waterville and Sangerville-Vassalboro Frms. Detailed $Fe_{py}/Fe_{HR}$ .....	254
6.9 Waits River and Gile Mtn Fms. Iron Pools by Grade .....	255
6.10 Waterville and Sangerville-Vassalboro Frms. Iron Pools by Grade	256
6.11 Example Metamorphic Reactions in Iron Speciaiton Crossplot .....	257
S6.1 Waits River and Gile Mtn Fms. Trace Comparison Pyr in $Fe_{carb}$ .....	258
S6.2 Waits River and Gile Mtn Fms. Trace Comparison Pyr in $Fe_{py}$ .....	259
S6.3 Waterville and S-V Frms. Trace Comparison Pyr in $Fe_{carb}$ .....	260
S6.4 Waterville and S-V Frms. Trace Comparison Pyr in $Fe_{py}$ .....	261

# Chapter 1

## Introduction

## 1.1 Background

The rise of atmospheric oxygen and subsequent oxygenation of oceans and lakes was a dramatic environmental shift that changed our planet and the life inhabiting it. A major rise in oxygen occurred ~2.35 billion years ago (Ga) in an event called the Great Oxidation Event (GOE) (Bekker et al., 2004; Farquhar et al., 2000). Although some scientists believed the GOE was spurred by the biological innovation of oxygenic photosynthesis (e.g. Johnson et al., 2013; Kopp et al., 2005; Williamson et al., 2011), oxygen would have been toxic to many organisms and required radical changes of evolutionary pathways for early life (Fischer et al., 2016; Sleep and Bird, 2008).

Before the GOE, atmospheric oxygen was constrained to low levels by mass-independent fractionation of sulfur isotopes ( $<0.001\%$  present atmospheric levels) (Farquhar et al., 2000; Pavlov and Kasting, 2002) and by detrital redox-sensitive mineral grains ( $<0.015\%$  present atmospheric levels) (Johnson et al., 2014). During this anoxic time period, transition metals were prevalent in the oceans and heavily utilized by microbes for nutrients, energy, and chemical building blocks (Eck and Dayhoff, 1966; Schoepp-Cothenet et al., 2012; Williams and Frausto Da Silva, 2003; Zerkle et al., 2005). However, transitions in redox state of the Earth's atmosphere and oceans after the GOE changed the proportions of metals used in early organisms (Williams and Frausto Da Silva, 2003; Zerkle et al., 2005). The changing redox conditions also affected the evolution of complex eukaryote cells. Oxygen is required in making certain biological compounds (e.g. sterols) contained in all eukaryotes (e.g. Brocks et al., 2003; Fischer, 2016; Raymond and Blankenship, 2004) and almost all eukaryotes today contain mitochondria. Although acquired late in the development of eukaryotic cells (Pittis and Gabaldón, 2016), mitochondria perform the oxidative-phosphorylation reactions that allow the aerobic metabolisms observed in most modern eukaryotes today (Embley and Martin, 2006). Better understanding of aqueous environmental conditions during the Archean and Proterozoic, especially oxygen

and sulfur levels, will allow better understanding of the constraints and pacing of evolution.

Several different techniques have been applied in recent years to understand the paleoenvironment during these critical periods for development of life on Earth. Much of the focus has been on redox conditions; therefore, many new methods have been developed focusing on transition metals as a window into redox processes on the ancient Earth. Observations of iron mineralogy in sedimentary rocks have been utilized for over 50 years to understand changes in redox during the time period surrounding the GOE (e.g. Cloud, 1968; Holland, 1984), and a new geochemical proxy called iron speciation builds upon the fundamental redox sensitivity of iron to more quantitatively provide redox determinations of water column chemistry from ancient rocks (Poulton and Canfield, 2005, 2011). Iron speciation studies have revealed a hitherto unobserved complexity in paleoenvironmental conditions with redox character varying from oxic to ferruginous (anoxic) to euxinic ( $\text{H}_2\text{S}$ -rich, anoxic) over short time periods, between geographic locations, and within single basins (Fig. 1.1A) (e.g. Canfield et al., 2013; Gilleaudeau and Kah, 2015; Sperling et al., 2015). If correct, this would fundamentally change our canonical understanding of Precambrian time (Fig. 1.1B) and force re-evaluation of environmental constraints on the evolution of life. In this dissertation, I use distinct multi-part techniques in a new approach for understanding Precambrian paleoenvironments at key evolutionary stages.

## **1.2 Dissertation Summary**

The oldest fossil evidence for life on Earth occurs in disputed microfossils from the 3.45 Ga Apex Chert and the 3.43 Ga Strelley Pool Formation (Brasier et al., 2015; Schopf, 1993; Wacey et al., 2012) as well as in the stromatolites of the Strelley Pool Formation (Allwood et al., 2006; Hofmann et al., 1999; Lowe, 1980) (Fig. 1.1C). However, these stromatolites are possibly abiogenic based on their regular laminae and surface normal accretion (Grotzinger and Knoll, 1999;

Lowe, 1994). The oldest non-disputed biologically-mediated stromatolites are those from the 2.72 Ga Tumbiana Formation, Fortescue Group, Western Australia which show trapped-and-bound detrital grains, organic carbon globules, and laminae that vary systematically in thickness (Awramik and Buchheim, 2009; Coffey et al., 2013; Flannery and Walter, 2012; Lepot et al., 2009; Wacey et al., 2010) (Fig. 1.1C). In Chapter 2 of this dissertation, I discuss work targeting these stromatolites to understand the microbial metabolic processes they record and the surrounding environmental conditions before the GOE.

The Tumbiana Formation contains a unique organic carbon isotope signature that is very depleted in  $^{13}\text{C}$  compared to younger samples; it is the type section of a global isotopic signature called the Fortescue Excursion (Eigenbrode and Freeman, 2006; Fischer et al., 2009; Hayes et al., 1983; Hayes et al., 1999; Schidlowski et al., 1983; Schoell and Wellmer, 1981). Early work suggested the excursion could be due biological cycling of methane in an “Age of Global Methanotrophy” before the rise of oxygen (Hayes, 1994; Schoell and Wellmer, 1981). Later developments suggested the methanotrophy could be anaerobic in nature (Hinrichs, 2002); however, molecular biomarkers were found in the Fortescue Group that suggested the presence of cyanobacteria and oxygenic photosynthesis, although later they were proposed to be from secondary migrating fluids or surface contamination (Brocks et al., 2003; Brocks et al., 1999; French et al., 2015; Rasmussen et al., 2008). Therefore, further studies have variably chosen aerobic or anaerobic photosynthetic metabolic processes paired with methanotrophy to explain the carbonate isotopic signal (Coffey et al., 2013; Eigenbrode and Freeman, 2006; Stüeken et al., 2015; Thomazo et al., 2009; Yoshiya et al., 2012). I combined textural petrographic observations, magnetic microscopy, microscale isotopic sampling, and modeling of the Archean carbonate system with literature values of Phanerozoic methanotrophy to highlight that these samples, although slightly affected by surface weathering, preserve a real signal that is not suggestive of methanotrophy, neither aerobic nor anaerobic in nature. Instead I propose that an alternative metabolism, the reductive acetyl Coenzyme A (CoA)



pathway, could be responsible for the inorganic and organic carbon isotope signatures captured in the Tumbiana stromatolites. The reductive acetyl CoA pathway is a primitive carbon fixation metabolism that can also generate energy or be paired with other catabolic pathways, and it is currently used by a number of anaerobic microbes including acetogens, methanogens, and sulfate reducers (Fuchs, 2011; Martin, 2012; Nitschke and Russell, 2012). The reductive acetyl CoA pathway is restricted to anaerobic metabolisms due to oxygen-sensitive enzymes and incredibly reducing potentials, suggesting that the shallow-water stromatolites were deposited in an anoxic environment. The Tumbiana Formation stromatolites represent a completely distinct biological system in an anoxic Archean world with foreign microbial processes dominating the ecosystem.

About 500 million years after the GOE, fossil evidence for eukaryotes begins to appear in the rock record (Fig. 1.1C) (Knoll et al., 2006). The delayed appearance of eukaryotic fossils after the rise of oxygen and slow evolution from single celled eukaryotes to multicellularity to animals have been the subjects of intense debate beyond the scope of this work; however, environmental factors such as redox conditions and oxygen levels have often been suggested to determine the timing of these evolutionary events (e.g. Anbar and Knoll, 2002; Kah and Bartley, 2011). Eukaryotes mark their appearance in the rock record through large complex microfossils (e.g. Bergmann et al., 2013; Javaux et al., 2004; Lamb et al., 2009; Xiao et al., 1997; Yan and Liu, 1993) and the first body macrofossils. *Grypania spiralis* macrofossils are found in the 1.85 Ga iron formations of Canada and the United States (Han and Runnegar, 1992; Knoll et al., 2006) as well as in the Mesoproterozoic Gaoyuzhuang Formation in China and the 1.45 Ga Greyson Formation of the Belt Supergroup in Montana (Walcott, 1899; Walter et al., 1976; Walter et al., 1990). The lower Belt Supergroup contains other diverse macro- and microfossils, a few of which have been interpreted to be eukaryotes (Adam et al., 2014; Fedonkin and Yochelson, 2002; Horodyski, 1993; Horodyski et al., 1989; Retallack et al., 2013). In Chapters 3, 4, and 5, I investigate the formations in which these putative eukaryotes were found

to understand the redox conditions and paleoenvironment of shallow waters as well as in deeper parts of the mid-Proterozoic Belt Basin.

The Belt Supergroup is a classic, well-studied mid-Proterozoic stratigraphic sequence due to its incredible preservation, expanded thickness, and large areal extent with outcrops exposed in Montana, Idaho, Washington, Alberta, and British Columbia. Many previous studies have focused on understanding the redox character and depositional environment of the lower Belt strata within the Belt Supergroup; initial work using iron mineralogy, sedimentological features, and sulfur and carbon isotopes and abundances suggested euxinic deep waters with oxic waters in persistent stratification (Gellatly and Lyons, 2005; Huebschman, 1973; Luepke and Lyons, 2001; Lyons et al., 2000). A recent study using iron speciation instead interpreted that ferruginous conditions dominated during lower Belt deposition, and that ferruginous conditions were an important redox state throughout much of the Proterozoic (Planavsky et al., 2011; Poulton and Canfield, 2011). A further study on the lower Belt Supergroup using nitrogen isotopes has expanded this view by suggesting shallow waters were oxic in a stratified basin (Stüeken, 2013). I chose to investigate the redox nature of the Belt Basin by similarly utilizing iron mineralogy and chemistry, but in a new approach combining textural observations from field geology, optical microscopy, magnetic microscopy, and (synchrotron) microprobe x-ray spectroscopy with bulk rock magnetic measurements. I sampled the lower Belt Group across a range of well-characterized metamorphic conditions from sub-biotite to garnet zone (Duke and Lewis, 2010) in order to understand not only the primary mineralogy for redox interpretations, but also how iron mineralogy changes after deposition in diagenetic and metamorphic reactions and how these overprints could be untangled. My analyses found that extensive recrystallization and diagenetic/metamorphic transformations had occurred, even in the best-preserved parts of the Belt Basin. However, primary mineralogy was preserved in recrystallized early diagenetic pyrite and sulfate as well as detrital iron oxides such as magnetite and hematite. I suggest that the Belt Basin was primarily oxic

with suboxic, anoxic, and/or sulfidic pore waters similar to modern environments. This work helps connect eukaryote development to conditions in which they are known to thrive.

One concern when utilizing iron mineralogy for paleoredox interpretations is that subsequent diagenetic and metamorphic alterations of iron minerals could occur and blur environmental information. In Chapters 5 and 6, I investigate these questions by studying transformations of the iron mineralogy within the same sedimentary rock formations across a range of metamorphic conditions from  $<300^{\circ}\text{C}$  (sub-biotite zone) to  $>575^{\circ}\text{C}$  (kyanite or sillimanite zone). Using data from the literature on Paleozoic siliciclastic and carbonate sequences in Maine and Vermont, it is clear that increasing metamorphic grade can affect paleoredox proxies by moving iron from carbonates, oxides, and sulfides to silicate minerals. In lower grade rocks, pyrrhotite formation and diagenetic iron carbonate formation are important transformations that severely affect proxies and, without detailed geological observations, require unsupported assumptions of metamorphic reactions to untangle. Interestingly, these theoretical modeled results match trends observed in the lower Belt rocks of Montana and Idaho across the sub-biotite and biotite zone. A definitive pyrrhotite-siderite isograd was mapped in the sub-biotite zone with additional appearances of iron silicates and oxides as metamorphic grade increased. Even in the best-preserved strata, Fe-rich carbonates, nano-phase pyrrhotite, and base-metal sulfides were observed, highlighting the mobility of iron in secondary diagenetic transformations. Utilization of textural methods to observe cross-cutting relationships and relative timing of mineralization is vital when studying Earth History using the sedimentary rock record. All Precambrian sedimentary rocks have been metamorphosed, so studies investigating environmental conditions and their ties to evolutionary biology must take this under consideration. Coupling textural, magnetic, and modeling techniques has allowed me to peel away secondary overprints to provide a window into Precambrian paleoenvironments.

### 1.3 Figures

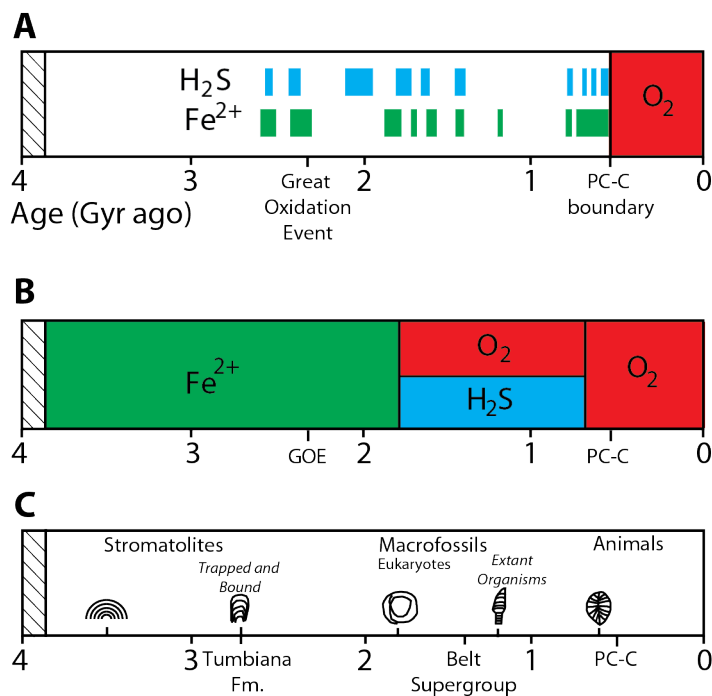


Figure 1.1: A) Recent views of redox from geochemical proxies, specifically iron speciation, using an outdated compilation (Planavsky et al., 2011) where  $\text{Fe}^{2+}$  stands for ferruginous conditions,  $\text{H}_2\text{S}$  for euxinic, and  $\text{O}_2$  for oxic. B) Canonical views of Precambrian redox conditions (Canfield, 1998; Cloud, 1968). C) Evolution of life summary based on the fossil record (references in text; Knoll et al., 2006). Abbreviations: PC-C—Precambrian-Cambrian boundary, GOE—Great Oxidation Event, Fm.—Formation. Region with dashed lines marks the end of the sedimentary rock record on Earth. Parts A and B modified from Planavsky et al. (2011).

## 1.4 References

- Adam, Z., Mogk, D., Skidmore, M., and Butterfield, N., Microfossils from the Greyson Formation, Lower Belt Supergroup: Support for early Mesoproterozoic biozonation, *in* Proceedings Geological Society of America Abstracts with Programs 2014, Volume 46, p. 71.
- Allwood, A. C., Walter, M. R., Kamber, B. S., Marshall, C. P., and Burch, I. W., 2006, Stromatolite reef from the Early Archaean era of Australia: *Nature*, v. 441, no. 7094, p. 714-718.
- Anbar, A. D., and Knoll, A., 2002, Proterozoic ocean chemistry and evolution: a bioinorganic bridge?: *science*, v. 297, no. 5584, p. 1137-1142.
- Awramik, S. M., and Buchheim, H. P., 2009, A giant, Late Archean lake system: The Meentheena Member (Tumbiana Formation; Fortescue Group), Western Australia: *Precambrian Research*, v. 174, no. 3, p. 215-240.
- Bekker, A., Holland, H., Wang, P.-L., Rumble, D., Stein, H., Hannah, J., Coetzee, L., and Beukes, N., 2004, Dating the rise of atmospheric oxygen: *Nature*, v. 427, no. 6970, p. 117-120.
- Bergmann, K. D., Grotzinger, J. P., and Fischer, W. W., 2013, Biological influences on seafloor carbonate precipitation: *Palaios*, v. 28, no. 2, p. 99-115.
- Brasier, M. D., Antcliffe, J., Saunders, M., and Wacey, D., 2015, Changing the picture of Earth's earliest fossils (3.5–1.9 Ga) with new approaches and new discoveries: *Proceedings of the National Academy of Sciences*, v. 112, no. 16, p. 4859-4864.
- Brocks, J. J., Buick, R., Summons, R. E., and Logan, G. A., 2003, A reconstruction of Archean biological diversity based on molecular fossils from the 2.78 to 2.45 billion-year-old Mount Bruce Supergroup, Hamersley Basin, Western Australia: *Geochimica et Cosmochimica Acta*, v. 67, no. 22, p. 4321-4335.
- Brocks, J. J., Logan, G. A., Buick, R., and Summons, R. E., 1999, Archean molecular fossils and the early rise of eukaryotes: *Science*, v. 285, no. 5430, p. 1033-1036.
- Canfield, D., 1998, A new model for Proterozoic ocean chemistry: *Nature*, v. 396, no. 6710, p. 450-453.
- Canfield, D. E., Ngombi-Pemba, L., Hammarlund, E. U., Bengtson, S., Chaussidon, M., Gauthier-Lafaye, F., Meunier, A., Riboulleau, A., Rollion-Bard, C., and Rouxel, O., 2013, Oxygen dynamics in the aftermath of the Great

Oxidation of Earth's atmosphere: Proceedings of the National Academy of Sciences, v. 110, no. 42, p. 16736-16741.

Cloud, P. E., 1968, Atmospheric and Hydrospheric Evolution on the Primitive Earth: Science, v. 160, no. 3829, p. 729-736.

Coffey, J., Flannery, D., Walter, M., and George, S., 2013, Sedimentology, stratigraphy and geochemistry of a stromatolite biofacies in the 2.72 Ga Tumbiana Formation, Fortescue Group, Western Australia: Precambrian Research, v. 236, p. 282-296.

Duke, E. F., and Lewis, R. S., 2010, Near infrared spectra of white mica in the Belt Supergroup and implications for metamorphism: American Mineralogist, v. 95, no. 7, p. 908-920.

Eck, R., and Dayhoff, M. O., 1966, Evolution of the structure of ferredoxin based on living relics of primitive amino acid sequences: Science, v. 152, p. 363-366.

Eigenbrode, J. L., and Freeman, K. H., 2006, Late Archean rise of aerobic microbial ecosystems: Proceedings of the National Academy of Sciences, v. 103, no. 43, p. 15759-15764.

Embley, T. M., and Martin, W., 2006, Eukaryotic evolution, changes and challenges: Nature, v. 440, no. 7084, p. 623-630.

Farquhar, J., Bao, H., and Thiemens, M., 2000, Atmospheric influence of Earth's earliest sulfur cycle: Science, v. 289, no. 5480, p. 756-758.

Fedonkin, M. A., and Yochelson, E. L., 2002, Middle Proterozoic (1.5 Ga) Horodyskia moniliformis Yochelson and Fedonkin, the oldest known tissue-grade colonial eucaryote: Smithsonian Contributions to Paleobiology, v. 94, p. 29.

Fischer, W., Schroeder, S., Lacassie, J., Beukes, N., Goldberg, T., Strauss, H., Horstmann, U., Schrag, D., and Knoll, A., 2009, Isotopic constraints on the Late Archean carbon cycle from the Transvaal Supergroup along the western margin of the Kaapvaal Craton, South Africa: Precambrian Research, v. 169, no. 1, p. 15-27.

Fischer, W. W., 2016, Breathing room for early animals: Proceedings of the National Academy of Sciences, v. 113, no. 7, p. 1686-1688.

Fischer, W. W., Hemp, J., and Valentine, J. S., 2016, How did life survive Earth's great oxygenation?: Current Opinion in Chemical Biology, v. 31, p. 166-178.

Flannery, D., and Walter, M., 2012, Archean tufted microbial mats and the Great Oxidation Event: new insights into an ancient problem: Australian Journal of Earth Sciences, v. 59, no. 1, p. 1-11.

French, K. L., Hallmann, C., Hope, J. M., Schoon, P. L., Zumberge, J. A., Hoshino, Y., Peters, C. A., George, S. C., Love, G. D., and Brocks, J. J., 2015, Reappraisal of hydrocarbon biomarkers in Archean rocks: Proceedings of the National Academy of Sciences, v. 112, no. 19, p. 5915-5920.

Fuchs, G., 2011, Alternative pathways of carbon dioxide fixation: insights into the early evolution of life?: Annual review of microbiology, v. 65, p. 631-658.

Gellatly, A. M., and Lyons, T. W., 2005, Trace sulfate in mid-Proterozoic carbonates and the sulfur isotope record of biospheric evolution: *Geochimica et Cosmochimica Acta*, v. 69, no. 15, p. 3813-3829.

Gilleaudeau, G. J., and Kah, L. C., 2015, Heterogeneous redox conditions and a shallow chemocline in the Mesoproterozoic ocean: evidence from carbon–sulfur–iron relationships: *Precambrian Research*, v. 257, p. 94-108.

Grotzinger, J. P., and Knoll, A. H., 1999, Stromatolites in Precambrian carbonates: evolutionary mileposts or environmental dipsticks?: Annual review of earth and planetary sciences, v. 27, no. 1, p. 313-358.

Han, T.-M., and Runnegar, B., 1992, Megascopic eukaryotic algae from the 2.1-billion-year-old Negaunee Iron-Formation, Michigan: *Science*, v. 257, no. 5067, p. 232-235.

Hayes, J., 1994, Global methanotrophy at the Archean-Proterozoic transition: Early life on Earth, v. 84, p. 220-236.

Hayes, J., Wedeking, K., and Kaplan, I., 1983, Precambrian organic geochemistry- Preservation of the record: Earth's earliest biosphere: Its origin and evolution(A 84-43051 21-51). Princeton, NJ, Princeton University Press, 1983, p. 93-134.

Hayes, J. M., Strauss, H., and Kaufman, A. J., 1999, The abundance of  $^{13}\text{C}$  in marine organic matter and isotopic fractionation in the global biogeochemical cycle of carbon during the past 800 Ma: *Chemical Geology*, v. 161, no. 1, p. 103-125.

Hinrichs, K. U., 2002, Microbial fixation of methane carbon at 2.7 Ga: Was an anaerobic mechanism possible?: *Geochemistry, geophysics, geosystems*, v. 3, no. 7, p. 1-10.

Hofmann, H., Grey, K., Hickman, A., and Thorpe, R., 1999, Origin of 3.45 Ga coniform stromatolites in Warrawoona group, Western Australia: *Geological Society of America Bulletin*, v. 111, no. 8, p. 1256-1262.

Holland, H. D., 1984, The chemical evolution of the atmosphere and oceans, Princeton University Press.

Horodyski, R. J., 1993, Paleontology of Proterozoic shales and mudstones: examples from the Belt Supergroup, Chuar Group and Pahrump Group, western USA: *Precambrian Research*, v. 61, no. 3, p. 241-278.

Horodyski, R. J., Winston, D., and Whipple, J. W., 1989, Paleontology of the middle Proterozoic belt supergroup, *in* Winston, D., Horodyski, R. J., and Whipple, J. W., eds., Middle Proterozoic Belt Supergroup, Western Montana: Great Falls, Montana to Spokane, Washington: 28th International Geological Congress, Field Trip Guidebook T334, p. 7-26.

Huebschman, R. P., 1973, Correlation of fine carbonaceous bands across a Precambrian stagnant basin: *Journal of Sedimentary Research*, v. 43, no. 3, p. 688-699.

Javaux, E. J., Knoll, A. H., and Walter, M. R., 2004, TEM evidence for eukaryotic diversity in mid - Proterozoic oceans: *Geobiology*, v. 2, no. 3, p. 121-132.

Johnson, J. E., Gerpheide, A., Lamb, M. P., and Fischer, W. W., 2014, O<sub>2</sub> constraints from Paleoproterozoic detrital pyrite and uraninite: *Geological Society of America Bulletin*, v. 126, no. 5-6, p. 813-830.

Johnson, J. E., Webb, S. M., Thomas, K., Ono, S., Kirschvink, J. L., and Fischer, W. W., 2013, Manganese-oxidizing photosynthesis before the rise of cyanobacteria: *Proceedings of the National Academy of Sciences*, v. 110, no. 28, p. 11238-11243.

Kah, L. C., and Bartley, J. K., 2011, Protracted oxygenation of the Proterozoic biosphere: *International Geology Review*, v. 53, no. 11-12, p. 1424-1442.

Knoll, A. H., Javaux, E. J., Hewitt, D., and Cohen, P., 2006, Eukaryotic organisms in Proterozoic oceans: *Philosophical Transactions of the Royal Society B: Biological Sciences*, v. 361, no. 1470, p. 1023-1038.

Kopp, R. E., Kirschvink, J. L., Hilburn, I. A., and Nash, C. Z., 2005, The Paleoproterozoic snowball Earth: a climate disaster triggered by the evolution of oxygenic photosynthesis: *Proceedings of the National Academy of Sciences of the United States of America*, v. 102, no. 32, p. 11131-11136.

Lamb, D., Awramik, S., Chapman, D., and Zhu, S., 2009, Evidence for eukaryotic diversification in the ~ 1800 million-year-old Changzhougou Formation, North China: *Precambrian Research*, v. 173, no. 1, p. 93-104.



Lepot, K., Benzerara, K., Rividi, N., Cotte, M., Brown, G. E., and Philippot, P., 2009, Organic matter heterogeneities in 2.72 Ga stromatolites: alteration versus preservation by sulfur incorporation: *Geochimica et Cosmochimica Acta*, v. 73, no. 21, p. 6579-6599.

Lowe, D. R., 1980, Stromatolites 3,400-myr old from the archaean of Western Australia: *Nature*, v. 284, no. 5755, p. 441-443.

-, 1994, Abiological origin of described stromatolites older than 3.2 Ga: *Geology*, v. 22, no. 5, p. 387-390.

Luepke, J. J., and Lyons, T. W., 2001, Pre-Rodinian (Mesoproterozoic) supercontinental rifting along the western margin of Laurentia: geochemical evidence from the Belt-Purcell Supergroup: *Precambrian Research*, v. 111, no. 1, p. 79-90.

Lyons, T. W., Luepke, J. J., Schreiber, M. E., and Zieg, G. A., 2000, Sulfur geochemical constraints on Mesoproterozoic restricted marine deposition: lower Belt Supergroup, northwestern United States: *Geochimica et Cosmochimica Acta*, v. 64, no. 3, p. 427-437.

Martin, W. F., 2012, Hydrogen, metals, bifurcating electrons, and proton gradients: the early evolution of biological energy conservation: *FEBS letters*, v. 586, no. 5, p. 485-493.

Nitschke, W., and Russell, M. J., 2012, Redox bifurcations: mechanisms and importance to life now, and at its origin: *Bioessays*, v. 34, no. 2, p. 106-109.

Pavlov, A., and Kasting, J., 2002, Mass-independent fractionation of sulfur isotopes in Archean sediments: strong evidence for an anoxic Archean atmosphere: *Astrobiology*, v. 2, no. 1, p. 27-41.

Pittis, A. A., and Gabaldón, T., 2016, Late acquisition of mitochondria by a host with chimaeric prokaryotic ancestry: *Nature*, v. 531, no. 7592, p. 101-104.

Planavsky, N. J., McGoldrick, P., Scott, C. T., Li, C., Reinhard, C. T., Kelly, A. E., Chu, X., Bekker, A., Love, G. D., and Lyons, T. W., 2011, Widespread iron-rich conditions in the mid-Proterozoic ocean: *Nature*, v. 477, no. 7365, p. 448-451.

Poulton, S. W., and Canfield, D. E., 2005, Development of a sequential extraction procedure for iron: implications for iron partitioning in continentally derived particulates: *Chemical Geology*, v. 214, no. 3, p. 209-221.

-, 2011, Ferruginous conditions: a dominant feature of the ocean through Earth's history: *Elements*, v. 7, no. 2, p. 107-112.

Rasmussen, B., Fletcher, I. R., Brocks, J. J., and Kilburn, M. R., 2008, Reassessing the first appearance of eukaryotes and cyanobacteria: *Nature*, v. 455, no. 7216, p. 1101-1104.

Raymond, J., and Blankenship, R. E., 2004, Biosynthetic pathways, gene replacement and the antiquity of life: *Geobiology*, v. 2, no. 4, p. 199-203.

Retallack, G. J., Dunn, K. L., and Saxby, J., 2013, Problematic Mesoproterozoic fossil *Horodyskia* from Glacier National Park, Montana, USA: *Precambrian Research*, v. 226, p. 125-142.

Schidlowski, M., Hayes, J., and Kaplan, I., 1983, Isotopic inferences of ancient biochemistries- Carbon, sulfur, hydrogen, and nitrogen: Earth's earliest biosphere: Its origin and evolution(A 84-43051 21-51). Princeton, NJ, Princeton University Press, 1983, p. 149-186.

Schoell, M., and Wellmer, F.-W., 1981, Anomalous  $^{13}\text{C}$  depletion in early Precambrian graphites from Superior Province, Canada.

Schoepp-Cothenet, B., van Lis, R., Philippot, P., Magalon, A., Russell, M. J., and Nitschke, W., 2012, The ineluctable requirement for the trans-iron elements molybdenum and/or tungsten in the origin of life: *Scientific reports*, v. 2.

Schopf, J. W., 1993, Microfossils of the Early Archean Apex chert: new evidence of the antiquity of life: *Science*, v. 260, no. 5108, p. 640-646.

Sleep, N. H., and Bird, D. K., 2008, Evolutionary ecology during the rise of dioxygen in the Earth's atmosphere: *Philosophical Transactions of the Royal Society of London B: Biological Sciences*, v. 363, no. 1504, p. 2651-2664.

Sperling, E. A., Wolock, C. J., Morgan, A. S., Gill, B. C., Kunzmann, M., Halverson, G. P., Macdonald, F. A., Knoll, A. H., and Johnston, D. T., 2015, Statistical analysis of iron geochemical data suggests limited late Proterozoic oxygenation: *Nature*, v. 523, no. 7561, p. 451-454.

Stüeken, E., Buick, R., and Schauer, A., 2015, Nitrogen isotope evidence for alkaline lakes on late Archean continents: *Earth and Planetary Science Letters*, v. 411, p. 1-10.

Stüeken, E. E., 2013, A test of the nitrogen-limitation hypothesis for retarded eukaryote radiation: nitrogen isotopes across a Mesoproterozoic basinal profile: *Geochimica et Cosmochimica Acta*, v. 120, p. 121-139.

Thomazo, C., Ader, M., Farquhar, J., and Philippot, P., 2009, Methanotrophs regulated atmospheric sulfur isotope anomalies during the Mesoarchean

(Tumbiana Formation, Western Australia): *Earth and Planetary Science Letters*, v. 279, no. 1, p. 65-75.

Wacey, D., Gleeson, D., and Kilburn, M., 2010, Microbialite taphonomy and biogenicity: new insights from NanoSIMS: *Geobiology*, v. 8, no. 5, p. 403-416.

Wacey, D., Menon, S., Green, L., Gerstmann, D., Kong, C., McLoughlin, N., Saunders, M., and Brasier, M., 2012, Taphonomy of very ancient microfossils from the ~ 3400Ma Strelley Pool Formation and ~ 1900Ma Gunflint Formation: New insights using a focused ion beam: *Precambrian Research*, v. 220, p. 234-250.

Walcott, C. D., 1899, Pre-Cambrian fossiliferous formations: *Geological Society of America Bulletin*, v. 10, no. 1, p. 199-244.

Walter, M., Oehler, J. H., and Oehler, D. Z., 1976, Megascopic algae 1300 million years old from the Belt Supergroup, Montana: a reinterpretation of Walcott's *Helminthoidichnites*: *Journal of Paleontology*, v. 50, p. 872-881.

Walter, M., Rulin, D., and Horodyski, R. J., 1990, Coiled carbonaceous megafossils from the Middle Proterozoic of Jixian (Tianjin) and Montana: *American Journal of Science*, v. 290, p. 133-148.

Williams, R. P. J., and Frausto Da Silva, J. J. R., 2003, Evolution was chemically constrained: *Journal of Theoretical Biology*, v. 220, no. 3, p. 323-343.

Williamson, A., Conlan, B., Hillier, W., and Wydrzynski, T., 2011, The evolution of Photosystem II: insights into the past and future: *Photosynthesis research*, v. 107, no. 1, p. 71-86.

Xiao, S., Knoll, A. H., Kaufman, A. J., Yin, L., and Zhang, Y., 1997, Neoproterozoic fossils in Mesoproterozoic rocks? Chemostratigraphic resolution of a biostratigraphic conundrum from the North China Platform: *Precambrian Research*, v. 84, no. 3, p. 197-220.

Yan, Y.-z., and Liu, Z.-l., 1993, Significance of eukaryotic organisms in the microfossil flora of Changcheng system: *Acta Micropalaeontol. Sin.*, v. 10, p. 167-180.

Yoshiya, K., Nishizawa, M., Sawaki, Y., Ueno, Y., Komiya, T., Yamada, K., Yoshida, N., Hirata, T., Wada, H., and Maruyama, S., 2012, In situ iron isotope analyses of pyrite and organic carbon isotope ratios in the Fortescue Group: Metabolic variations of a Late Archean ecosystem: *Precambrian Research*, v. 212, p. 169-193.

Zerkle, A. L., House, C. H., and Brantley, S. L., 2005, Biogeochemical signatures through time as inferred from whole microbial genomes: *American Journal of Science*, v. 305, no. 6-8, p. 467-502.

## Chapter 2

# Examining Archean Methanotrophy

*Originally published in:*

*Slotznick, S. P., and Fischer, W. W., 2016, Examining Archean methanotrophy:*

*Earth and Planetary Science Letters*, v. 441, p. 52-59. doi:

*10.1016/j.epsl.2016.02.013*

## 2.1 Abstract

The carbon isotope ratios preserved in sedimentary rocks can be used to fingerprint ancient metabolisms. Organic carbon in Late Archean samples stands out from that of other intervals with unusually low  $\delta^{13}\text{C}$  values ( $\sim -45$  to  $-60\text{‰}$ ). It was hypothesized that these light compositions record ecosystem-wide methane cycling and methanotrophy, either of the aerobic or anaerobic variety. To test this idea, we studied the petrography and carbon and oxygen isotope systematics of well-known and spectacular occurrences of shallow water stromatolites from the 2.72 Ga Tumbiana Formation of Western Australia. We examined the carbonate cements and kerogen produced within the stromatolites, because methanotrophy is expected to leave an isotopic fingerprint in these carbon reservoirs. Mathematical modeling of Archean carbonate chemistry further reveals that methanotrophy should still have a discernible signature preserved in the isotopic record, somewhat diminished from those observed in Phanerozoic sedimentary basins due to higher dissolved inorganic carbon concentrations. These stromatolites contain kerogen with  $\delta^{13}\text{C}_{\text{org}}$  values of  $\sim -50\text{‰}$ . By microsampling different regions and textures within the stromatolites, we determined that the isotopic compositions of the authigenic calcite cements show a low degree of variation and are nearly identical to values estimated for seawater at this time; the lack of low and variable  $\delta^{13}\text{C}_{\text{carb}}$  values implies that methanotrophy does not explain the low  $\delta^{13}\text{C}_{\text{org}}$  seen in the coeval kerogen. These observations do not support a methanotrophy hypothesis, but instead hint that the Late Archean may constitute an interval wherein autotrophs employed markedly different biochemical processes of energy conservation and carbon fixation.

## 2.2 Introduction

It is widely recognized that organic matter contained in sedimentary successions of Late Archean age (circa 2.5 to 2.9 Ga) has unusually  $^{13}\text{C}$ -depleted isotopic compositions ( $\delta^{13}\text{C}_{\text{org}} \sim -45$  to  $-60\text{‰}$  PDB) compared to younger intervals (Phanerozoic  $\delta^{13}\text{C}_{\text{org}} \sim -22$  to  $-32\text{‰}$  PDB) (Eigenbrode and Freeman, 2006;

Fischer et al., 2009; Schoell and Wellmer, 1981; Thomazo et al., 2009). From its discovery in ultra-mature Late Archean kerogens from the Superior Province and the Tumbiana Formation of the Fortescue Group, Western Australia, it was hypothesized that this isotopic signal reflects the enhanced paleoenvironmental cycling of methane (Hayes, 1994; Schoell and Wellmer, 1981).

Oxidation and assimilation of methane by methanotrophic organisms yields exceptionally  $^{13}\text{C}$ -depleted biomass. Recognizing this, Hayes (1994) introduced the concept of a Late Archean “Age of Global Methanotrophy”, to explain the  $\delta^{13}\text{C}$  values seen in Archean organic matter. This was originally envisioned as aerobic methanotrophy (Hayes, 1994), but later based on two discoveries—microbial consortia capable of anaerobic oxidation of methane (AOM) in modern anoxic environments (Boetius et al., 2000) and the widespread mass independent fractionation of sulfur isotopes in Archean basins (Farquhar et al., 2000)—Hinrichs (2002) updated the idea to include AOM, expanding on a point made similarly by Schoell and Wellmer (1981) on the basis of modern sedimentary pore fluid biogeochemical profiles. By comparing accumulation rates of methane oxidation from modern methane seeps, anoxic coastal sediment, and the Tumbiana Formation, Hinrichs (2002) showed that AOM processes could reasonably explain the Archean isotopic signal, possibly even under the condition of lower seawater sulfate concentrations. Subsequent studies developed biogeochemical variations on this theme again involving oxygenic photosynthesis or anoxygenic photosynthetic pathways, but these hypotheses all draw on abundant ecosystem methanotrophy in large part to explain the  $^{13}\text{C}$ -depleted kerogen, with the disappearance of this isotopic signal in younger Precambrian strata due to either a decline in atmospheric methane or changes in the relative abundance of electron acceptors for methanotrophy (Coffey et al., 2013; Eigenbrode and Freeman, 2006; Stüeken et al., 2015; Thomazo et al., 2009; Yoshiya et al., 2012).

Despite its attractiveness, there are several outstanding issues with the global methanotrophy hypothesis that could benefit from further testing. 1) While substantially more  $^{13}\text{C}$ -depleted than expected by carboxylation from the Calvin

cycle, the isotopic composition of Late Archean organic matter is not unique for methanotrophs and is consistent with other biochemical pathways (Blaser et al., 2013; Fischer et al., 2009; Gelwicks et al., 1989). 2) Sulfate levels may have been sufficiently low as to greatly limit the extent of sulfate reduction-driven AOM in Late Archean marine basins (Crowe et al., 2014), though methane oxidation might have been instead accomplished anaerobically via ferric iron phases (Beal et al., 2009) or high-valent nitrogen-bearing compounds (Haroon et al., 2013). Finally, 3) existing data from Archean carbonates with exceptionally low  $\delta^{13}\text{C}_{\text{org}}$  values do not host isotopic and textural features one might expect of carbonates produced in environments of prevalent methanotrophy.

Fortunately, environments in which methanotrophy is a principal part of the carbon mass flux leave isotopic signatures not just in the organic phases present, but also in the carbonate phases produced; this forms the logic for an approach to test the global methanotrophy hypothesis. Both aerobic methanotrophy and AOM increase dissolved inorganic carbon (DIC) in the environment and strongly alter the carbon isotope ratios by adding isotopically light DIC. Furthermore, AOM also generates a strong flux of alkalinity and thus promotes the precipitation of carbonates as described by the following net reaction:  $\text{CH}_4 + \text{SO}_4^{-2} + \text{Ca}^{+2} \rightarrow \text{CaCO}_3 + \text{H}_2\text{S} + \text{H}_2\text{O}$  (Michaelis et al., 2002). Authigenic carbonates formed by methanotrophic processes have been widely observed in modern marine sediments (e.g. Luff and Wallmann, 2003; Marlow et al., 2014) and can be readily preserved in the geological record where they have been recognized on the basis of isotopic and textural features in Phanerozoic strata, and perhaps as old as 635 Ma (Bristow and Grotzinger, 2013; Peckmann and Thiel, 2004). AOM creates both carbonate and organic matter with remarkably low  $\delta^{13}\text{C}$  values (Bristow and Grotzinger, 2013)(Table S2.1). We compiled a comprehensive C isotope dataset from AOM sites preserved in Phanerozoic basins (Table S2.1); the data illustrate that  $\delta^{13}\text{C}_{\text{carb}}$  values can be down to -59‰ and  $\delta^{13}\text{C}_{\text{org}}$  values can be as low as -133‰, with typical  $\delta^{13}\text{C}$  values both substantially more variable and much lower overall than Archean values.



To test the methanotrophy hypothesis, we closely examined the petrographic textures and isotopic compositions of kerogen and authigenic carbonate cements in stromatolites collected from the Late Archean Tumbiana Formation—an archive that has become an effective stratotype for  $^{13}\text{C}$ -depleted Archean organic matter (Eigenbrode and Freeman, 2006; Hayes, 1994; Thomazo et al., 2009). These rocks are well suited for this analysis because they contain both kerogen and authigenic calcite cements preserved in stromatolitic laminations. We measured the carbonate cements that precipitated in the stromatolites at a finer texture-specific scale than has been done previously to look for any evidence of AOM, and combined traditional C and O isotope ratio measurements on the carbonate cements with clumped isotope analyses to evaluate the impacts of post-depositional processes on these materials. Finally we interpret the data in the context of a model of Archean carbonate chemistry, and discuss other potential metabolisms that might better explain the observations, such as the possibility that the  $^{13}\text{C}$ -depleted Archean kerogens reflect an entirely different mode of biochemical carboxylation.

### **2.3 Geological background and methods**

The Tumbiana Formation was deposited at  $2721 \pm 4$  Ma during an interval of rifting and subsidence, and onlaps the Pilbara craton (Blake et al., 2004). It ranges in thickness from a few meters up to 320 m, and is lithologically diverse, consisting of conglomerates, shale, mudstones, siltstones, sandstones, breccias, basalts, tuff, and limestone (Thorne and Trendall, 2001). It is notably laterally variable containing many different facies that have been proposed to represent either lacustrine (Awramik and Buchheim, 2009; Buick, 1992; Coffey et al., 2013) or shallow marine settings (Sakurai et al., 2005; Thorne and Trendall, 2001); notably however, these facies all reflect shallow water paleoenvironments. This contrasts with typical methanotrophic environments both today and in Phanerozoic basins (typically slope/deep marine or within sedimentary pore fluids, (Campbell et al., 2002; Campbell, 2006; Marlow et al., 2014; Michaelis et al., 2002) making the highly  $^{13}\text{C}$ -depleted kerogens in the Tumbiana Formation intriguing and unique.

Samples were collected from outcrops of the Meentheena Member of the Tumbiana Formation at the Redmont/Knossos Area, Western Australia (22°02'44" S, 118°59'34" E) (Fig. 2.1). The Meentheena Member constitutes the uppermost sequence of the Tumbiana Formation, and is composed of a 30 to 50 m thick unit of interbedded carbonate (mainly limestone) and immature siliciclastic and volcanoclastic lithologies. The unit also contains spectacular occurrences of a diversity of well-preserved stromatolites (Awramik and Buchheim, 2009; Coffey et al., 2013; Flannery and Walter, 2012)—the lithologies targeted in this study. In the sampling locality, the exposure of the Meentheena Member outcrop is 11 m thick (Fig. S2.1). Here the Meentheena Member contains trough cross-stratified and wave-rippled sandstones and grainstones from coarse to very fine-grained, the latter of which become interbedded with stromatolites up section. Associated with mudcracks, these stromatolites developed in an intertidal environment that deepens to dominantly subtidal facies upsection (Sakurai et al., 2005).

Outcrop samples were cut into slabs and polished to reveal textures and provide fresh surfaces for analysis. Petrographic thin sections were made from book-matched surfaces of the slabs sampled for isotopic analysis, and imaged using light and electron microscopy. Scanning electron microscopy (SEM) and X-ray dispersive spectroscopy (EDS) were performed using a combined ZEISS 1550VP Field Emission SEM and Oxford INCA Energy 300 X-ray dispersive spectrometer at Caltech.

Powders for carbonate  $\delta^{13}\text{C}$  and  $\delta^{18}\text{O}$  isotopic analysis were collected using a micro-rotary drill with a 2 mm bit. Diverse textures (stromatolite with abundant grains, stromatolite with abundant cement, intercolumn sediment, across areas of differential recrystallization) were sampled in order to create a detailed cm-scale isotope ratio map of textures within these ancient microbial structures, and uncover the effects of diagenesis. Samples for organic  $\delta^{13}\text{C}$  measurements were made on 5 to 10 g bulk stromatolite samples targeting organic-rich laminae, and, excluding intercolumn sedimentary fill, cut and then powdered using a mortar and pestle.

Inorganic  $\delta^{13}\text{C}$  and  $\delta^{18}\text{O}$  isotopic measurements were performed at the University of Michigan Stable Isotope Laboratory. Carbonate sample powders were placed in stainless steel combustion boats and baked under vacuum at  $200^\circ\text{C}$  to remove volatiles and water. Samples were then placed in borosilicate reaction vessels and reacted at  $77^\circ\text{C}$  with 4 drops of anhydrous phosphoric acid for 8 minutes in a Finnigan MAT Kiel IV preparation device coupled directly to the inlet of a Finnigan MAT 253 isotope ratio mass spectrometer. For 19 of the 50 samples, replicate splits were measured to assess accuracy and precision. Two NBS standards (NBS 18 and NBS 19) were run with the samples. Oxygen isotope ratio data were corrected for acid fractionation and source mixing by calibration to a best-fit regression line defined by standards. Analytical uncertainty is better than 0.1‰ for both carbon and oxygen isotopes. Data are reported in delta notation relative to VPDB standard.

For clumped isotope analysis at Caltech, sample powders were dried at  $50^\circ\text{C}$ . Five to ten milligrams of sample powder were dissolved in  $90^\circ\text{C}$  phosphoric acid for twenty minutes. The  $\text{CO}_2$  was purified by gas chromatography in the method developed by Passey et al. (2010), and different isotopologues of carbon dioxide (cardinal masses 44 through 49) were measured on a modified Finnigan MAT253 gas-source mass spectrometer. Sample unknowns were analyzed for eight acquisitions in seven cycles, with each cycle bracketed by measurements of reference gas. Raw values for  $\Delta^{47}$  were calculated relative to the reference gas, and then converted to the absolute reference frame by Ghosh et al. (2006) for low-temperature samples ( $<55^\circ\text{C}$ ) and the absolute reference frame by Eiler et al. (2009) for higher temperature samples using the transfer function as in Dennis et al. (2011). From clumped isotope temperatures and oxygen isotope ratio data, we estimated the  $\delta^{18}\text{O}$  of the water from which the carbonates precipitated using the relationship from Kim and O'Neil (1997).

For organic carbon analyses, sample powders were placed in tin combustion boats and decarbonated with hydrochloric acid.  $\delta^{13}\text{C}_{\text{org}}$  values were measured at UC Davis using a PDZ Europa ANCA-GSL elemental analyzer

coupled to a PDZ Europa 20-20 continuous flow isotope ratio mass spectrometer. The samples were combusted at 1020°C with chromium oxide and silvered cobaltous/cobaltic oxide catalysts. Following combustion, the helium carrier and analytes flowed through a water trap. Sample unknowns were calibrated against NIST standard reference materials and analytical uncertainty was better than 0.10‰. Data are reported in delta notation relative to VPDB.

## 2.4 Results

The Tumbiana stromatolites analyzed here are columnar laminated structures ranging in height from 4 cm to 18 cm. They are erect, non-branching with wide-intercolumn fill areas occurring in small clumps or within bioherms consistent with previous descriptions by Coffey et al. (2013) and Awramik and Buchheim (2009). Biological influence in the formation of these structures is suggested by laminae that systematically vary in thickness over the stromatolite apices, a criterion for biogenicity (Buick et al., 1981) (Fig. 2.2A). Additionally, at their edges, these laminae bend beyond the angle of repose and imply trapping and binding by some cohesive agent, such as microbial filaments (Frantz et al., 2015), with subsequent cementation. The laminae are composed of micritic calcite cements, varying in thickness from < 200 µm to 2 mm, alternating with thinner dark siliceous layers, with small amounts of residual kerogen. While some of the carbonate appears to have been recrystallized, this recrystallization varies in coarseness between layers (Figs. 2.2B, S2.2). Microscopy reveals a component of detrital material within the carbonate laminae, often in detrital layers filled with aluminosilicates, apatite, chlorite, and quartz (Figs. 2.2D, S2.2). The fill material deposited between stromatolites varies in composition between hand samples, but is predominantly siliciclastic sediment and carbonate cement with more rare detrital carbonate grains (Figs. 2.2CD, S2.2). It is important to note that petrographic textures of calcite cements and kerogen in laminations both support the interpretation that these phases had authigenic and coeval origins in the stromatolites (Grotzinger and Knoll, 1999; Lepot et al., 2008). Additionally, the

detailed textures of the Tumbiana stromatolites are distinct from Phanerozoic AOM seep carbonates, which are dominated by homogeneous and clotted microcrystalline carbonates, and rarer stromatolitic fabrics with complex and variable carbonate accretion orientations, botryoidal cements, irregular filled cavities, and *in situ* brecciation (Peckmann and Thiel, 2004). In modern methanic carbonates precipitated in anoxic bottom waters, large extensive structures of slabs, pavements, and upward growing chimneys and mounds are observed, but their internal structure is thrombolytic/clotted and distinct from the textures seen in Tumbiana stromatolites (Michaelis et al., 2002; Peckmann et al., 2001b).

$\delta^{13}\text{C}_{\text{carb}}$  and  $\delta^{18}\text{O}$  measurements of the micritic cements reveal a narrow range of values, from -0.93‰ to 1.18‰ (PDB) and -19.00‰ to -14.20‰ (PDB), respectively (Table S2.2). The data are distributed tightly with a mean and standard deviation of  $\delta^{13}\text{C}_{\text{carb}}$   $0.57 \pm 0.38\text{‰}$  ( $1\sigma$ ) and  $\delta^{18}\text{O}_{\text{carb}}$   $-18.40 \pm 0.89\text{‰}$  (Fig. 2.3A). Clumped isotope measurements reveal the impacts of both burial diagenetic and near surface weathering processes. Temperature estimates near the centroid of the  $\delta^{13}\text{C}_{\text{carb}}$  distribution are  $114 \pm 9^\circ\text{C}$ . We interpret this as a diagenetic temperature, which is supported by the very low  $\delta^{18}\text{O}$  values observed. The  $\delta^{18}\text{O}$  composition of the water in equilibrium with the carbonates at these temperatures is  $\sim -3\text{‰}$  VSMOW, consistent with recrystallization in the presence of ice-free marine and to a lesser degree relatively heavy meteoric pore fluids. In areas of the samples where near surface weathering has taken place (marked clearly by the oxidation of ferrous iron in pyrite and carbonate and resulting in the precipitation of secondary oxides, Fig. S2.3), the isotopic data show a trend with clumped temperature, causing  $\delta^{18}\text{O}$  to increase and  $\delta^{13}\text{C}_{\text{carb}}$  to drop (albeit very slightly  $\sim 1\text{‰}$ ). From this we interpret that infiltration and exchange with heavier meteoric waters raised the  $\delta^{18}\text{O}$  values, as average precipitation in Western Australia has  $\delta^{18}\text{O}$  values from -4.07‰ to -6.44‰ VSMOW (Liu et al., 2010) and a mean annual temperature *ca.*  $30^\circ\text{C}$ . Meteoric waters infiltrating the surface rock or near subsurface would be close to ambient air temperature and thus both lower the temperature and increase the  $\delta^{18}\text{O}$  values of the carbonate.

Our measured  $\delta^{13}\text{C}_{\text{carb}}$  values conform with other carbonate isotopic measurements on the Tumbiana Formation throughout the basin in a variety of carbonate facies (e.g. Awramik and Buchheim, 2009; Coffey et al., 2013; Eigenbrode and Freeman, 2006; Thomazo et al., 2009; Yoshiya et al., 2012), and from Late Archean carbonate platforms more broadly (Fischer et al., 2009). When the  $\delta^{13}\text{C}$  data are mapped back onto the sampled stromatolitic surfaces, little variation and no texture-specific pattern is visible among the values aside from the alteration trend discussed above due to surface weathering (Fig. 2.3). Notably, no differences were observed between stromatolitic cements and detrital, intercolumn-filling carbonate. This lack of variation is highly distinct from expectations of carbonates precipitated in methanic environments, which show distinct isotopic signatures for different textures as well as wider variation (5-10‰) within textures at similar length scales (e.g. Campbell et al., 2002; Peckmann et al., 2001b). The results show  $\delta^{13}\text{C}_{\text{carb}}$  values with an isotopic composition very similar to that estimated for dissolved inorganic carbon in Late Archean seawater, not the variable and  $^{13}\text{C}$ -depleted values observed in modern and ancient AOM environments (Table S2.1). While it remains possible that an unwavering mixture of isotopically distinct DIC pools could result in the same near seawater value, this scenario is unlikely based on the low degree of variation between fabrics, paleoenvironments (facies), and global comparisons.

$\delta^{13}\text{C}_{\text{org}}$  measurements show that the kerogen in the stromatolitic laminae is notably  $^{13}\text{C}$ -depleted with values from -49.91‰ to -53.2‰ (PDB), matching well with other organic measurements made on Tumbiana Formation carbonate outcrops in the Redmont area (Coffey et al., 2013; Eigenbrode and Freeman, 2006; Stüeken et al., 2015; Yoshiya et al., 2012). It is important to note that at a bulk-scale sedimentary organic matter can integrate biological sources with distinct isotopic compositions (Freeman et al., 1990); bulk values need to be considered as possible mixtures accordingly. *In situ* ion microprobe measurements of kerogen from the Tumbiana Formation uncovered two populations of  $\delta^{13}\text{C}_{\text{org}}$  values around -52.3‰ and -34.4‰; the former was

interpreted as a signature of methanotrophy while the latter a signal of photoautotrophy (Williford et al., 2016). That our measured bulk  $\delta^{13}\text{C}_{\text{org}}$  values reflect one of these populations suggests that these unusual  $^{13}\text{C}$ -depleted values accurately describe the composition of a microbial community which makes up the majority of the kerogen in the sedimentary rock, and are not spurious values resulting from a mixture of biomass from different populations with isotopic compositions substantially different than bulk observations. Importantly, these community values are substantially lower than those expected from carboxylation using Rubisco and the Calvin cycle (e.g. Guy et al., 1993), but not commonly as low as those observed in known methanotrophic biomass.

## 2.5 Results in the context of Archean carbonate chemistry

Although the  $\delta^{13}\text{C}_{\text{carb}}$  values suggest that methanotrophy was not a dominant metabolic process occurring in the Tumbiana stromatolites, it is important to consider this data in the context of the differing seawater carbonate chemistry that characterized the early Earth (Fischer et al., 2009; Grotzinger and Kasting, 1993; Hotinski et al., 2004). To alleviate the faint young sun paradox, it is thought that the early atmosphere contained a higher concentration of greenhouse gases, specifically  $\text{CO}_2$  (Owen et al., 1979; Sagan and Mullen, 1972). The amount of  $\text{CO}_2$  that existed in the Late Archean atmosphere is not well-constrained and model dependent; most efforts to quantify this found a lower limit of partial pressure of  $\text{CO}_2$  at 0.03 atm with an upper limit at 5 atm (Grotzinger and Kasting, 1993). Seawater in equilibrium with the early atmosphere would have had higher amounts of dissolved inorganic carbonate species (DIC), and would tend to mute the metabolic signal of AOM in authigenic carbonates, all else kept equal (e.g. Bristow and Grotzinger, 2013).

To test this, we constructed a simple mathematical model that describes the carbonate chemistry and carbon isotope systematics of possible AOM environments for any concentration of atmospheric  $\text{CO}_2$  building on similar logic to previous approaches (Bristow and Grotzinger, 2013; Fischer et al., 2009). To

solve the carbonate system we used a range of  $p\text{CO}_2$  and pH values and the Matlab solver developed by Zeebe and Wolf-Gladrow (2001). pH of Late Archean seawater is not known with certainty, but can be constrained to within limits. From basin analysis of carbonate platforms and carbon cycle theory, it appears that the fluid Earth throughout Precambrian time produced carbonates to alleviate fluxes of carbon and alkalinity in a fashion similar to today (Grotzinger and James, 2000; Higgins et al., 2009). Leveraging this carbonate mineral saturation and higher  $p\text{CO}_2$ , it is likely that the pH of seawater was lower (Grotzinger and Kasting, 1993); a more recent model calculates for a  $p\text{CO}_2$  of  $10^5$   $\mu\text{atm}$ , a pH of 6.9 (Halevy et al., 2010). For the Meentheena Member of the Tumbiana Formation, the basin history is not understood sufficiently well to solve the carbonate chemistry with a high degree of confidence—it could be marine (e.g. Sakurai et al., 2005) or lacustrine (e.g. Awramik and Buchheim, 2009) in origin. However from lithological constraints, one can reasonably assume that  $\text{CaCO}_3$  saturation states in this body of water were greater than unity, but were probably less than  $\sim 10$  (Bergmann et al., 2013; Higgins et al., 2009). Because carbonate production was not tied to sources of alkalinity at the mouths of rivers that fed the Fortescue basin, it is also reasonable to assume calcium concentrations were in excess of carbonate ion concentrations (e.g. Higgins et al., 2009). This provides coarse constraints on the more likely solution space for DIC content of the basin waters, and a description of the order-of-magnitude uncertainty in the reconstruction (Figs. 2.4, S2.4).

To calculate the expected isotopic composition of authigenic carbonate, we used a closed box model that depends on a simple isotope mass balance between two pools: seawater DIC ( $\delta^{13}\text{C} = 0\text{‰}$ ) and  $^{13}\text{C}$ -depleted DIC metabolically derived from the oxidation of methane ( $\delta^{13}\text{C} = -60\text{‰}$ ). This simple mixing relationship is observed in authigenic structures above the sediment in the modern anoxic environment of the Black Sea (Michaelis et al., 2002; Peckmann et al., 2001b), as well as increasingly with depth in sediment pore-fluid AOM environments (Bristow and Grotzinger, 2013). Bracketing the ranges of  $\delta^{13}\text{C}$  from



modern AOM environments and assuming a similar relative metabolic fluxes of methane oxidation to organic matter production in Archean environments (Bristow and Grotzinger, 2013), calculations show that an Archean AOM environments should have  $\delta^{13}\text{C}$  values between -2‰ and -30‰ (Fig. 2.4). This calculation assumes a degree of coupling between methane oxidation and DIC and organic carbon production. Although lower global productivity may have characterized the Archean biosphere, the assumption of similar metabolic fluxes only considers rates of AOM needed to produce enough biomass to leave the depleted  $\delta^{13}\text{C}_{\text{org}}$  signature (Hinrichs, 2002); due to poor energetics, anaerobic methanotrophy has characteristically low growth yields and must oxidize substantial amounts of methane to obtain sufficient energy from this process for growth (~99:1; Thauer et al., 2008). Altogether, we observe that the typically  $^{13}\text{C}$ -depleted AOM carbonate values should have been only somewhat muted by higher DIC (Fig. 2.4). Supporting the results of this calculation, we note that low and variable  $\delta^{13}\text{C}$  values have been observed in authigenic carbonates in Archean strata. These are captured by early diagenetic siderite preserved in iron formation and ferruginous shales, and have been widely interpreted as the products of anaerobic microbial metabolism, likely dissimilatory iron reduction (Fischer et al., 2009; Johnson et al., 2013).

Thus despite their highly  $^{13}\text{C}$ -depleted kerogens, Tumbiana stromatolites do not record  $\delta^{13}\text{C}_{\text{carb}}$  values expected for AOM carbonates precipitated under conditions of Archean carbonate chemistry. This result suggests that AOM was not especially prevalent in this paleoenvironment, and that the microbial mats present during the development of these sedimentary structures were not comprised of large proportion of methanotrophs. While it remains possible that either or both aerobic and anaerobic methanotrophy were present as important metabolisms on the early Earth, it appears that neither was responsible for the striking isotopic signature seen in Tumbiana kerogens.

## 2.6 Alternative Carbon Fixation Pathways

If methanotrophy was not responsible for the notably low  $\delta^{13}\text{C}_{\text{org}}$  values in the Tumbiana Formation, what are the alternatives? Under the somewhat delicate assumption that carbon isotope fractionations of biosynthetic pathways have not significantly changed since their inception, one reasonable and attractive possibility is the reductive acetyl Coenzyme A (CoA) pathway (sometimes called the Wood-Ljungdahl pathway), which a number of anaerobic microbes (including acetogens, methanogens, and sulfate reducers) use to synthesize acetyl-CoA from carbon dioxide (Fischer et al., 2009). This is the only known carbon fixation pathway that does carboxylation and at the same time generates ATP (Fuchs 2011), using a clever biochemical energy conservation scheme termed electron bifurcation (Martin, 2012; Nitschke and Russell, 2012; Thauer et al., 2008). Autotrophic acetogens using the reductive acetyl-CoA pathway produce acetate with large fractionations ( $\epsilon = -38\text{‰}$  to  $-68\text{‰}$ ) from substrate DIC, with a large kinetic isotope effect likely associated with the key enzyme of that pathway: carbon-monoxide dehydrogenase (Blaser et al., 2013; Gelwicks et al., 1989). The produced acetate can further fuel heterotrophic metabolisms and propagate this light isotopic signal in the ecosystem. Thus we hypothesize that the low  $\delta^{13}\text{C}$  values of Tumbiana Formation kerogens—and perhaps those observed in Archean strata elsewhere (e.g. Fischer et al., 2009)—reflect the greater predominance of reductive acetyl-CoA pathway as an entry point for  $\text{CO}_2$  into the biosphere. Interestingly, from theory it has been argued that the reductive acetyl-CoA pathway represents the most primitive form of carbon fixation known (Fuchs, 2011; Martin, 2012; Nitschke and Russell, 2012); our observations provide some geological support for this idea.

Finally, the average standard redox potentials for reactions in the reductive acetyl-CoA pathway are more reducing than all other known carboxylation pathways, and the key enzymes involved make extensive use of cofactors that are highly  $\text{O}_2$ -sensitive (Fuchs, 2011). Consequently, this pathway was never evolutionarily adapted for aerobic metabolisms. If it is correct that the unique isotopic signature seen in Tumbiana Formation organic matter reflects

carboxylation via this pathway, it suggests that  $O_2$  levels in these shallow current-swept and well-lit paleoenvironments were sufficiently low to support significant populations of these anaerobic microorganisms.

## **2.7 Acknowledgements**

Support for this work was provided by the Agouron Institute (grant number AI-GC17.09.3), NSF Division of Earth Sciences award EAR-1349858, the NSF Graduate Research Fellowship program (S.P.S.), NASA Earth and Space Fellowship (S.P.S.), and the David and Lucile Packard Foundation (W.W.F.). Thanks to John Grotzinger, Renata Cummins, Daniel Stolper, and Kristin Bergmann for helpful comments and aid with clumped isotope measurements. We also thank John Higgins, Itay Halevy, David Fike, and two anonymous reviewers for helpful feedback that substantially improved the quality of the study.

## 2.8 Figures

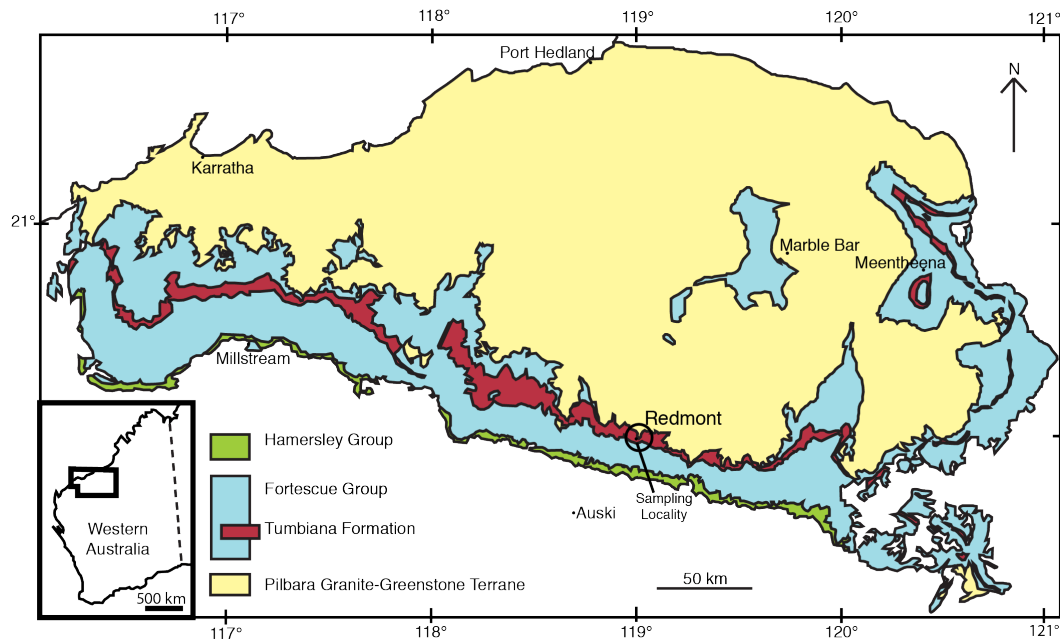


Figure 2.1: General geological map of Tumbiana Formation exposures modified from Sakurai et al. (2005). The Redmont sampling locality is marked.

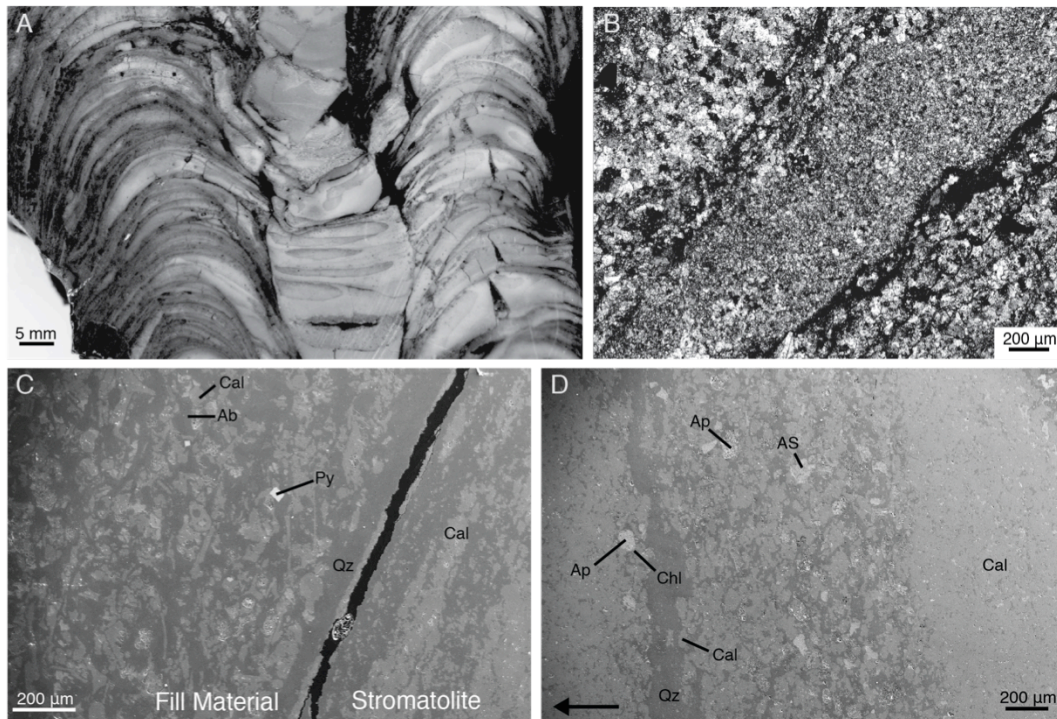


Figure 2.2: (A) Image of TB2f stromatolite. Note the laminae thicken and thin across stromatolite apices. (B) Photomicrograph in transmitted cross-polarized light shows differential coarseness of recrystallization between laminae in TA1b. (C) Scanning electron image of the contact between stromatolite versus fill material in TA1b. (D) Scanning electron image of a layer of detrital sediment within intercolumn fill material in TB2b. Abbreviations for minerals identified using X-ray dispersive spectroscopy: Ab = Albite, Ap = Apatite, AS = Fe, Mg aluminosilicate, Cal = Calcite, Chl = Chlorite, Py = Pyrite, Qz = Quartz. Arrow shows up direction if image is rotated.

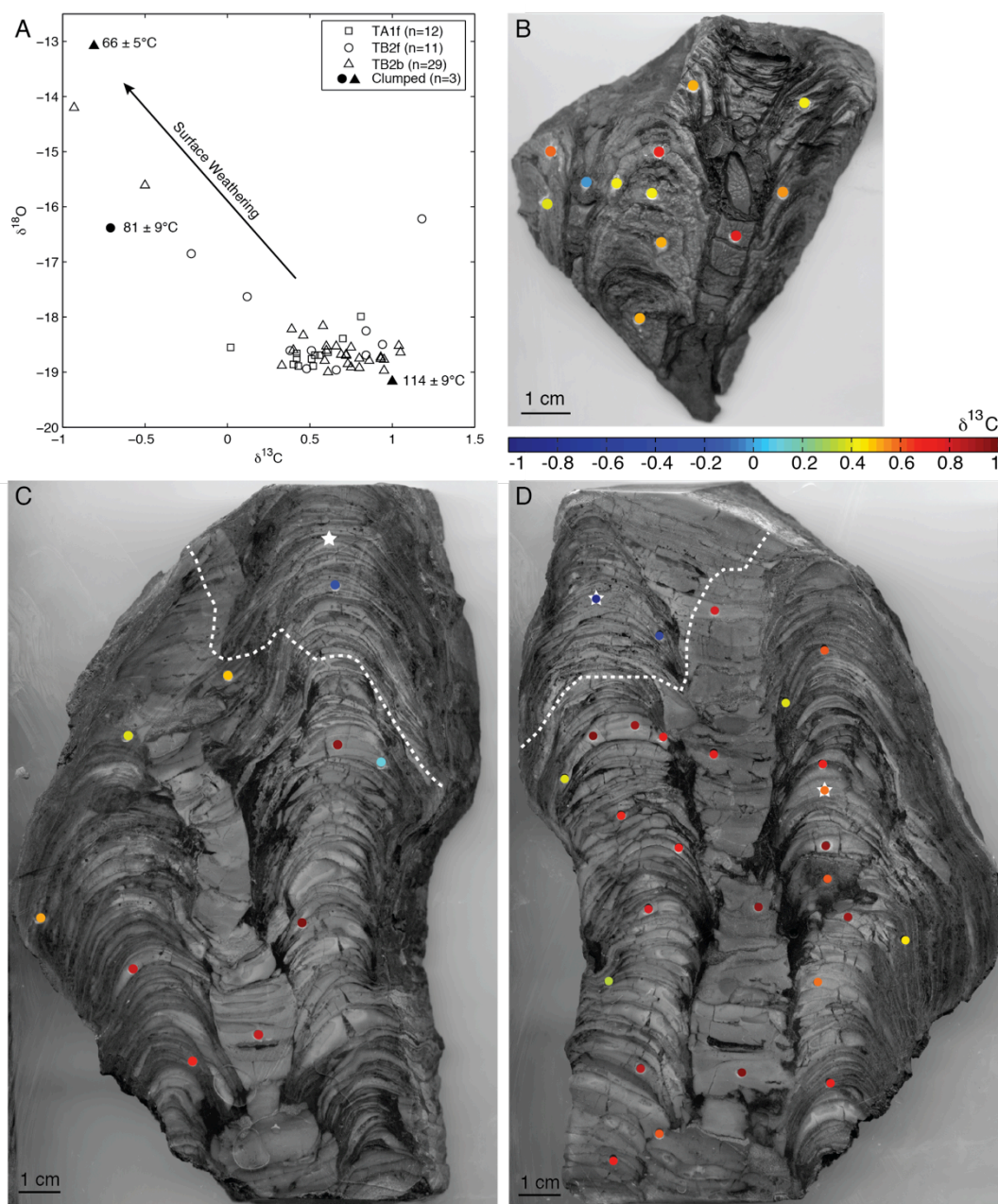


Figure 2.3: Carbon, oxygen, and clumped isotope data from Tumbiana stromatolites. (A) Crossplot of carbon and oxygen isotope ratios from micromilled carbonate textures. Clumped isotope temperature estimates are shown in filled symbols, and record a trend with C and O isotopes in regions of near-surface weathering. Locations of analytical spots and mapped  $\delta^{13}\text{C}_{\text{carb}}$  values for (B) TA1f, (C) TB2f, and (D) TB2b. Colorbar of isotopic values shown in (B) is the same for all samples. White stars indicate locations of clumped isotope spots sampled ~5 mm below the surface. Dashed white lines show area affected by meteoric water infiltration, delimited by presence of secondary iron oxides (Fig. S2.3).



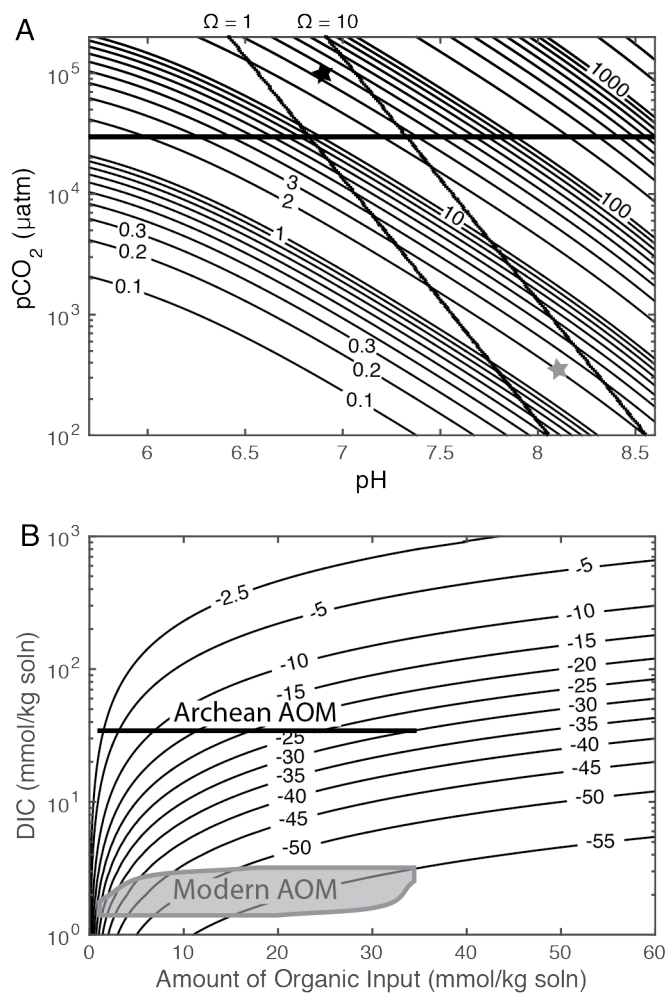


Figure 2.4: Estimates of the C isotopic composition of hypothetical AOM carbonate under conditions of Archean seawater carbonate chemistry. (A) Calculation of DIC in mmol/kg as a function of atmospheric  $\text{CO}_2$  and seawater pH. Horizontal black line marks a lower limit of  $p\text{CO}_2$  from Grotzinger and Kasting (1993). For reference, diagonal black curves mark calculated saturation states ( $\Omega = 1$  and  $\Omega = 10$ ) given modern  $[\text{Ca}^{2+}]$ . Grey star shows modern seawater, and black star is a reasonable Archean seawater estimate using constraints from Halevy et al. (2010). (B) AOM carbonate signature with modern AOM region based off DIC and  $\delta^{13}\text{C}_{\text{carb}}$  values and hypothetical Archean AOM carbonate estimate based off DIC estimates from (A).

## 2.9 Supplemental Tables

**Table S2.1: Examples of carbon isotopic signatures from Phanerozoic AOM sites**

Age	Location	$\delta^{13}\text{C}_{\text{org}}$ (‰ PDB)	$\delta^{13}\text{C}_{\text{carb}}$ (‰ PDB)	Reference*
Modern	Eel River Basin	-15 to -106	-3 to -40	1-3
Modern	Hydrate Ridge	-102 to -128	-24 to -58	4-6
Modern	Black Sea	-27 to -112	-25 to -41	7-9
Modern	Gulf of Mexico	-48 to -99	-18 to -55	10-12
Modern	Aleutian Margin	-124 to -130	-42 to -51	13
Modern	Nankai Trough, Japan	---	-36 to -56	14
Modern	Voring Plateau, Norwegian Sea	-43 to -133	-31 to -59	15-18
Miocene	Marmorito, Italy	-83 to -116	-17 to -50	19-21
Miocene	Pietralunga, Italy	-42 to -109	-22 to -40	22, 23
Oligocene	Lincoln Creek Fm., Washington	-90 to -120	-10 to -51	7, 24
Eocene to Miocene	Scotland District, Barbados	---	-20 to -50	25, 26
Cretaceous	Tepee Buttes, Colorado	---	-40 to -45	27-29
Cretaceous	Canadian Arctic	---	-35 to -50	30
Cretaceous	Hokkaido, Japan	-104 to -129	-41 to -45	31, 32
Cretaceous	Raukumara Peninsula, New Zealand	-37 to -99	7 to -29	33
Cretaceous to Jurassic	California	-31 to -122	-19 to -44	34, 35
Jurassic	Alexander Island, Antarctica	---	-34 to -45	36
Jurassic	Beauvoism, France	-68 to -76	-12 to -27	20
Carboniferous	Harz Mountains, Germany	---	-8 to -32	37
Carboniferous	Ganibobis, Namibia	---	7 to -52	38
Devonian	Holland Mound, Morocco	---	-11 to -22	39, 40

\* References: 1. Hinrichs et al. (2000), 2. Orphan et al. (2002), 3. Orphan et al. (2004), 4. Elvert et al. (1999), 5. Elvert et al. (2001), 6. Greinert et al. (2001), 7. Thiel et al. (2001), 8. Peckmann et al. (2001b), 9. Michaelis et al. (2002), 10. Zhang et al. (2002), 11. Zhang et al. (2003), 12. Roberts and Aharon (1994), 13. Greinert et al. (2002), 14. Sakai et al. (1992), 15. Mazzini et al. (2005), 16. Mazzini et al. (2006), 17. Ivanov et al. (2010), 18. Chevalier et al. (2014), 19. Thiel et al. (1999), 20. Peckmann et al. (1999b), 21. Cavagna et al. (1999), 22. Terzi (1993), 23. Peckmann et al. (2004), 24. Peckmann et al. (2002), 25. Torrini et al. (1990), 26. Gill et al. (2005), 27. Kauffman et al. (1996), 28. Shapiro and Fricke (2002), 29. Shapiro (2004), 30. Beauchamp and Savard (1992), 31. Hikida et al. (2003), 32. Ogihara (2008), 33. Kiel et al. (2013), 34. Campbell et al. (2002), 35. Birgel et al. (2006), 36. Kelly et al. (1995), 37. Peckmann et al. (2001a), 38. Himmler et al. (2008), 39. Peckmann et al. (1999a), 40. Peckmann et al. (2005)



Table S2.2: Isotopic Data from the Tumbiana Formation

Specimen name	Sample	$\delta^{13}\text{C}_{\text{carb}}$ (PDB)	$\delta^{13}\text{O}_{\text{carb}}$ (PDB)	Weathered	$\delta^{13}\text{O}_{\text{water}}$ (SMOW)	Temperature $\pm 1\sigma$	$\delta^{13}\text{C}_{\text{org}}$ (PDB)
TA1f, 1	TA1f	0.81	-17.99	0	--	--	--
TA1f, 2	TA1f	0.56	-18.69	0	--	--	--
TA1f, 3	TA1f	0.51	-18.76	0	--	--	--
TA1f, 4	TA1f	0.70	-18.39	0	--	--	--
TA1f, 5	TA1f	0.42	-18.75	0	--	--	--
TA1f, 6	TA1f	0.53	-18.69	0	--	--	--
TA1f, 7	TA1f	0.52	-18.89	0	--	--	--
TA1f, 8	TA1f	0.02	-18.55	0	--	--	--
TA1f, 9	TA1f	0.61	-18.64	0	--	--	--
TA1f, 10	TA1f	0.42	-18.66	0	--	--	--
TA1f, 11	TA1f	0.40	-18.86	0	--	--	--
TA1f, 12	TA1f	0.43	-18.89	0	--	--	--
TB2b, 2	TB2b	0.95	-18.97	0	--	--	--
TB2b, 3	TB2b	1.04	-18.52	0	--	--	--
TB2b, 4	TB2b	0.75	-18.91	0	--	--	--
TB2b, 5	TB2b	0.93	-18.76	0	--	--	--
TB2b, 6	TB2b	1.05	-18.64	0	--	--	--
TB2b, 7	TB2b	0.39	-18.22	0	--	--	--
TB2b, 8	TB2b	0.66	-18.53	0	--	--	--
TB2b, 9	TB2b	-0.93	-14.20	1	--	--	--
TB2b, 10	TB2b	-0.50	-15.61	1	--	--	--
TB2b, 11	TB2b	0.40	-18.60	0	--	--	--
TB2b, 12	TB2b	0.60	-18.61	0	--	--	--
TB2b, 13	TB2b	0.69	-18.68	0	--	--	--
TB2b, 14	TB2b	0.59	-18.79	0	--	--	--
TB2b, 15b	TB2b	0.95	-18.77	0	--	--	--
TB2b, 16	TB2b	0.60	-18.53	0	--	--	--
TB2b, 17	TB2b	0.46	-18.33	0	--	--	--
TB2b, 18	TB2b	0.93	-18.73	0	--	--	--
TB2b, 19	TB2b	0.58	-18.16	0	--	--	--
TB2b, 20	TB2b	0.73	-18.85	0	--	--	--
TB2b, 21	TB2b	0.33	-18.88	0	--	--	--
TB2b, 22	TB2b	0.86	-18.79	0	--	--	--
TB2b, 23	TB2b	0.61	-19.00	0	--	--	--
TB2b, 24	TB2b	0.80	-18.92	0	--	--	--
TB2b, 25	TB2b	0.80	-18.75	0	--	--	--
TB2b, 26	TB2b	0.72	-18.68	0	--	--	--
TB2b, 27	TB2b	0.72	-18.70	0	--	--	--
TB2b, 28	TB2b	0.75	-18.55	0	--	--	--
TB2f, 1	TB2f	0.94	-18.50	0	--	--	--
TB2f, 2	TB2f	-0.22	-16.85	1	--	--	--
TB2f, 3	TB2f	1.18	-16.22	0	--	--	--
TB2f, 4	TB2f	0.84	-18.25	0	--	--	--
TB2f, 5	TB2f	0.84	-18.69	0	--	--	--
TB2f, 6	TB2f	0.66	-18.96	0	--	--	--
TB2f, 7	TB2f	0.51	-18.61	0	--	--	--
TB2f, 8	TB2f	0.48	-18.94	0	--	--	--
TB2f, 9	TB2f	0.12	-17.63	0	--	--	--
TB2f, 10	TB2f	0.38	-18.61	0	--	--	--
Clump1	TB2b	1.00	-19.17	0	-3.10	114 $\pm$ 9	--
Clump2	TB2b	-0.81	-13.08	1	-5.07	56 $\pm$ 5	--
Clump3	TB2f	-0.71	-16.38	1	-4.60	81 $\pm$ 9	--
Org_TA1	TA1 (f&b)	--	--	--	--	--	-53.2
Org_TB2, 1	TB2 (f&b)	--	--	--	--	--	-49.91
Org_TB2, 2	TB2 (f&b)	--	--	--	--	--	-52.07

## 2.10 Supplemental Figures

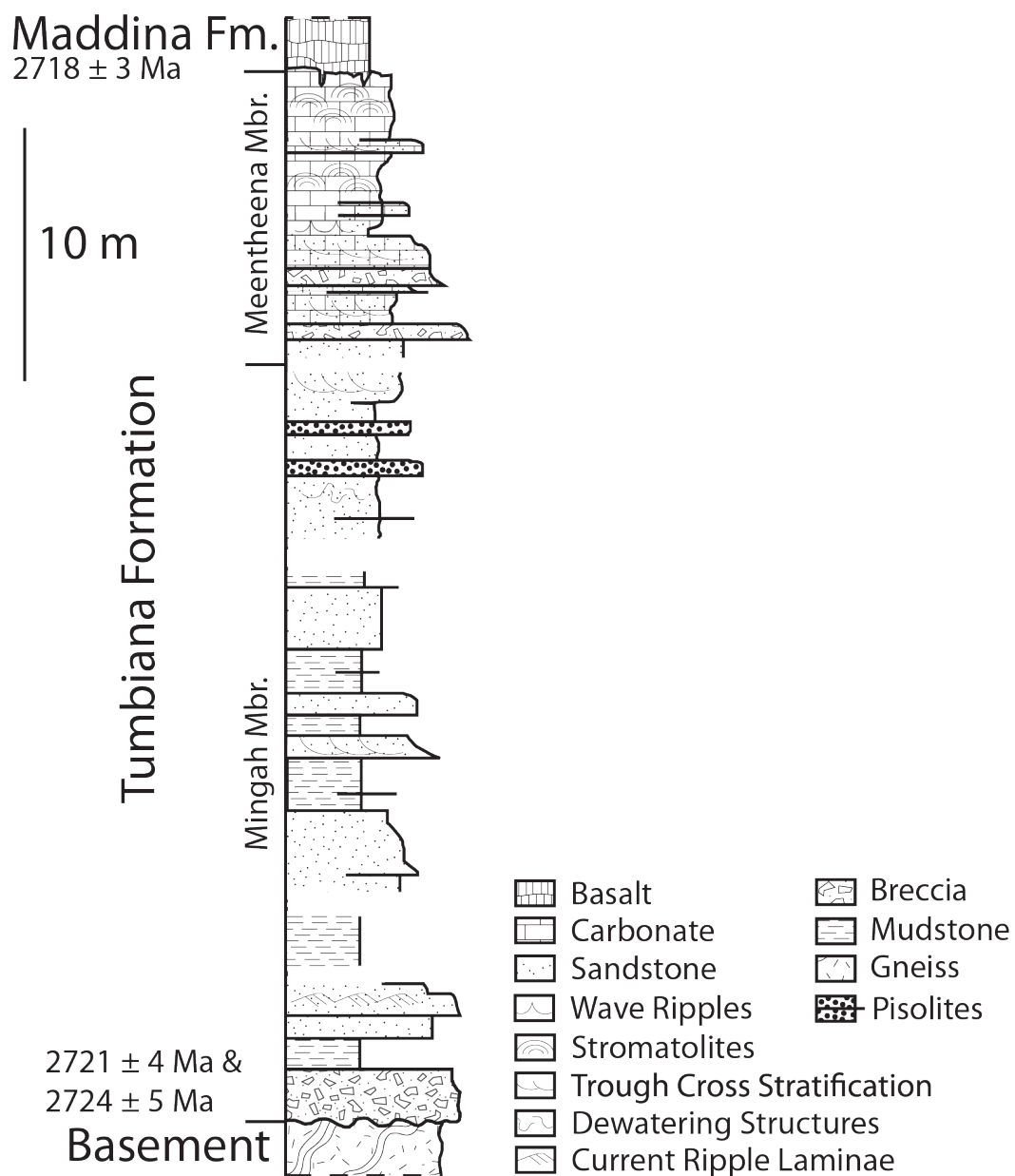


Figure S2.1: Stratigraphic column of the study locality, modified from Sakurai et al. (2005) with age constraints from Blake et al. (2004).

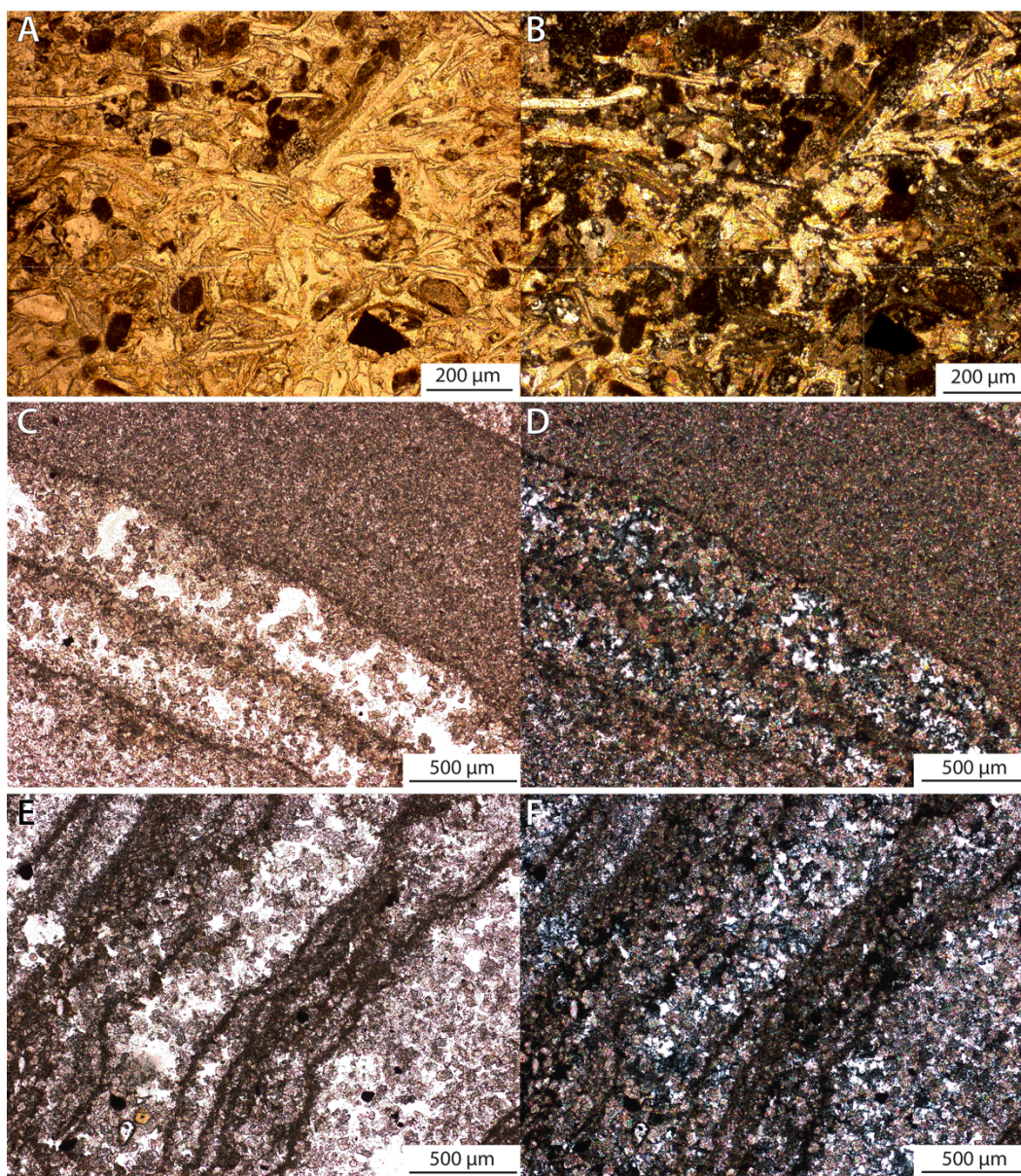


Figure S2.2: Plane-polarized (A) and cross-polarized (B) transmitted light microscope images of fill material in TA1b highlighting rare detrital carbonate grains with siliciclastic detrital minerals and carbonate cement. Plane-polarized (C) and cross-polarized (D) transmitted light microscope images of stromatolitic layers in TB2b highlighting proportion of carbonate versus siliciclastic minerals in variably recrystallized laminae. Plane-polarized (E) and cross-polarized (F) transmitted light microscope images of stromatolitic laminae in TB2b with “trapped-and-bound” detrital minerals beyond the angle of repose.



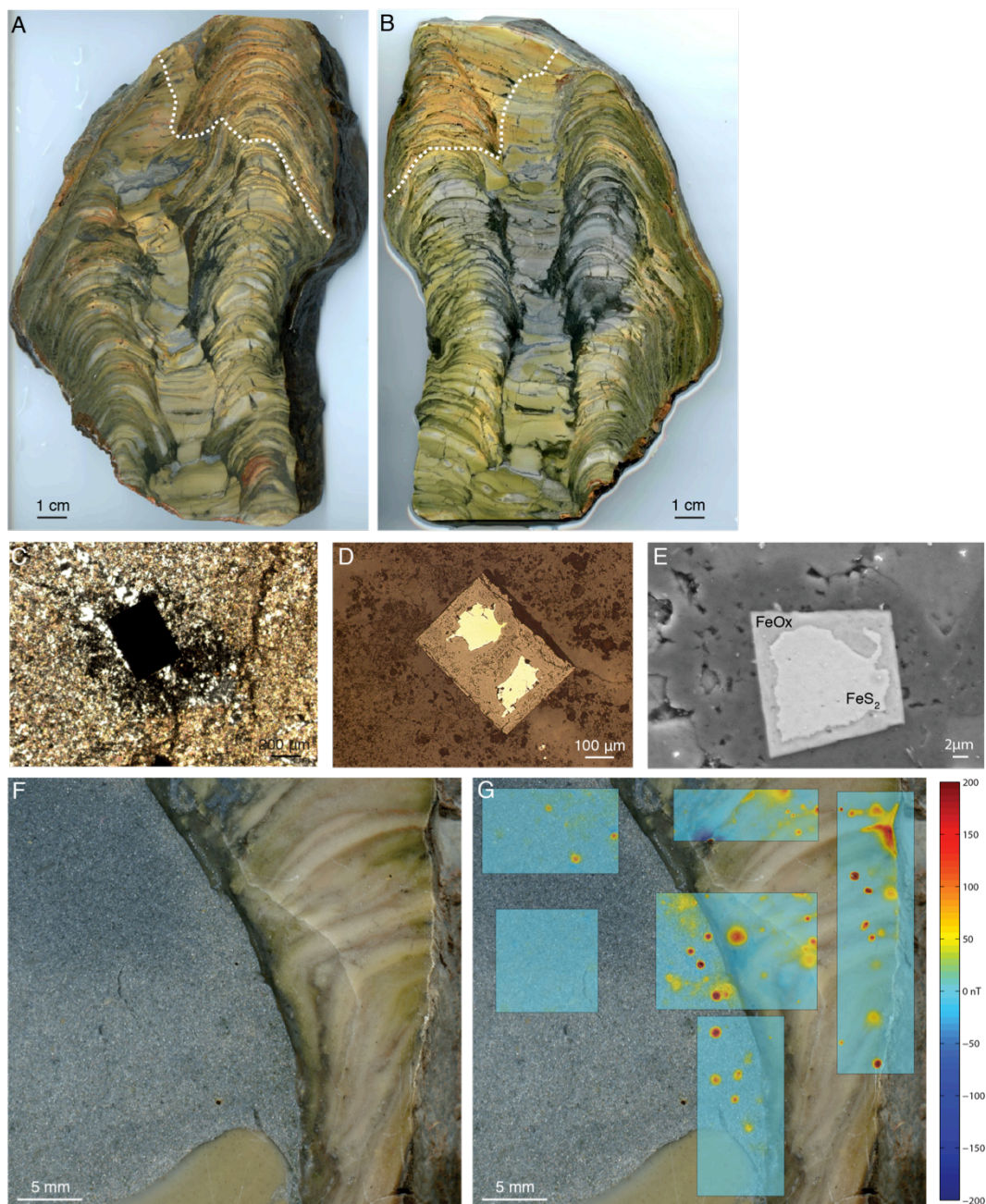


Figure S2.3: Color photograph showing secondary iron oxides forming from near surface oxidation of ferrous iron in pyrite and carbonate for (A) TB2f (B) TB2b. C) Transmitted cross-polarized light microscope image of a euhedral opaque mineral on TB2b thin section. D) Reflected light photomicrograph of same crystal highlighting brighter iron sulfide core with iron oxide rim, interpreted as oxidation during near-surface weathering. E) Scanning electron microscope image highlighting another euhedral pyrite (FeS<sub>2</sub>) core with iron oxide (FeOx) rim on

TA1b, confirmed by X-ray dispersive spectroscopy. Ultra-high resolution scanning SQuID microscopy (UHRSSM) of small regions on TA2f was performed at the Caltech Paleomagnetism Laboratory after giving the sample a strong magnetization perpendicular to slab surface showing magnetic dipoles in warm colors (G) with a resolution of 40 or 80  $\mu\text{m}$ . These dipoles represent magnetic minerals and match the locations of the dark euhedral phases (F). We interpret these as oxidized pyrite similar to those seen in petrographic work and interpret the magnetic signal to be derived from secondary iron oxides.

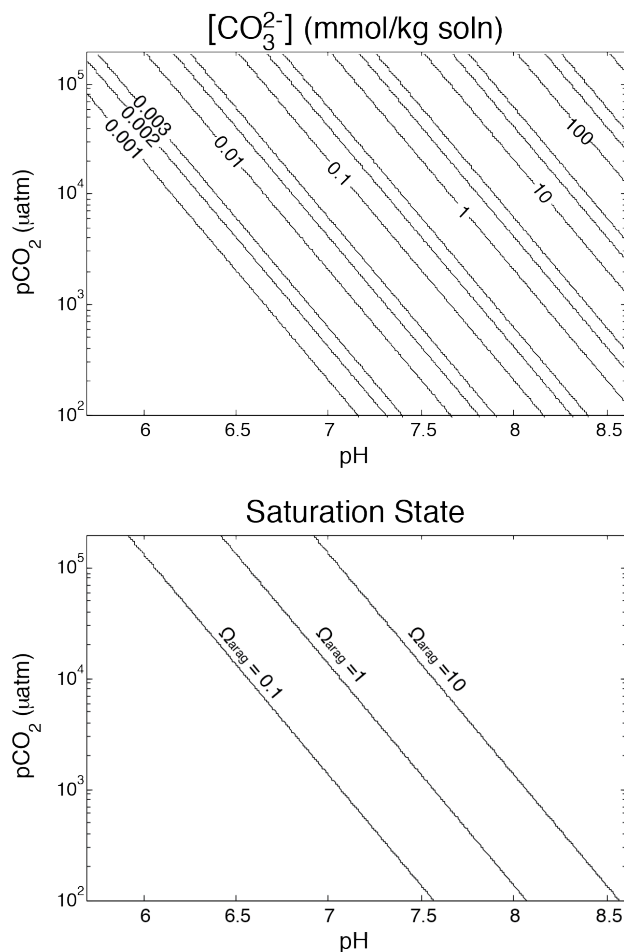


Figure S2.4: Calculations showing constraints on the carbonate chemistry of Tumbiana basin waters over a range of CaCO<sub>3</sub> saturation states. Upper panel: calculation of [CO<sub>3</sub><sup>2-</sup>] in mmol/kg as a function of atmospheric CO<sub>2</sub> and seawater pH. Lower panel: assuming modern [Ca<sup>2+</sup>] (10.28 mmol/kg solution, Zeebe and Wolf-Gladrow (2001)) and standard temperature, pressure, and salinity, saturation state for aragonite precipitation was calculated. Due to the linearity of this calculation, changes in the [Ca<sup>2+</sup>] will scale simply with the saturation state, *i.e.* Ω = 10 at modern [Ca<sup>2+</sup>] is equivalent to Ω = 1 at 10 times modern [Ca<sup>2+</sup>].

## 2.11 References

- Awramik, S. M., and Buchheim, H. P., 2009, A giant, Late Archean lake system: The Meentheena Member (Tumbiana Formation; Fortescue Group), Western Australia: *Precambrian Research*, v. 174, no. 3, p. 215-240.
- Beal, E. J., House, C. H., and Orphan, V. J., 2009, Manganese- and iron-dependent marine methane oxidation: *Science*, v. 325, no. 5937, p. 184-187.
- Beauchamp, B., and Savard, M., 1992, Cretaceous chemosynthetic carbonate mounds in the Canadian Arctic: *Palaios*, p. 434-450.
- Bergmann, K. D., Grotzinger, J. P., and Fischer, W. W., 2013, Biological influences on seafloor carbonate precipitation: *Palaios*, v. 28, no. 2, p. 99-115.
- Birgel, D., Thiel, V., Hinrichs, K.-U., Elvert, M., Campbell, K. A., Reitner, J., Farmer, J. D., and Peckmann, J., 2006, Lipid biomarker patterns of methane-seep microbialites from the Mesozoic convergent margin of California: *Organic Geochemistry*, v. 37, no. 10, p. 1289-1302.
- Blake, T., Buick, R., Brown, S., and Barley, M., 2004, Geochronology of a Late Archaean flood basalt province in the Pilbara Craton, Australia: constraints on basin evolution, volcanic and sedimentary accumulation, and continental drift rates: *Precambrian Research*, v. 133, no. 3, p. 143-173.
- Blaser, M. B., Dreisbach, L. K., and Conrad, R., 2013, Carbon isotope fractionation of 11 acetogenic strains grown on H<sub>2</sub> and CO<sub>2</sub>: *Applied and environmental microbiology*, v. 79, no. 6, p. 1787-1794.
- Boetius, A., Ravensschlag, K., Schubert, C. J., Rickert, D., Widdel, F., Gieseke, A., Amann, R., Jørgensen, B. B., Witte, U., and Pfannkuche, O., 2000, A marine microbial consortium apparently mediating anaerobic oxidation of methane: *Nature*, v. 407, no. 6804, p. 623-626.
- Bristow, T. F., and Grotzinger, J. P., 2013, Sulfate availability and the geological record of cold-seep deposits: *Geology*, v. 41, no. 7, p. 811-814.
- Buick, R., 1992, The antiquity of oxygenic photosynthesis: evidence from stromatolites in sulphate-deficient Archaean lakes: *Science*, v. 255, no. 5040, p. 74-77.
- Buick, R., Dunlop, J., and Groves, D., 1981, Stromatolite recognition in ancient rocks: an appraisal of irregularly laminated structures in an Early Archaean chert-barite unit from North Pole, Western Australia: *Alcheringa*, v. 5, no. 3, p. 161-181.

Campbell, K., Farmer, J., and Des Marais, D., 2002, Ancient hydrocarbon seeps from the Mesozoic convergent margin of California: carbonate geochemistry, fluids and palaeoenvironments: *Geofluids*, v. 2, no. 2, p. 63-94.

Campbell, K. A., 2006, Hydrocarbon seep and hydrothermal vent palaeoenvironments and paleontology: past developments and future research directions: *Palaeogeography, Palaeoclimatology, Palaeoecology*, v. 232, no. 2, p. 362-407.

Cavagna, S., Clari, P., and Martire, L., 1999, The role of bacteria in the formation of cold seep carbonates: geological evidence from Monferrato (Tertiary, NW Italy): *Sedimentary Geology*, v. 126, no. 1, p. 253-270.

Chevalier, N., Bouloubassi, I., Stadnitskaia, A., Taphanel, M.-H., and Damsté, J. S. S., 2014, Lipid biomarkers for anaerobic oxidation of methane and sulphate reduction in cold seep sediments of Nyegga pockmarks (Norwegian margin): discrepancies in contents and carbon isotope signatures: *Geo-Marine Letters*, v. 34, no. 2-3, p. 269-280.

Coffey, J., Flannery, D., Walter, M., and George, S., 2013, Sedimentology, stratigraphy and geochemistry of a stromatolite biofacies in the 2.72 Ga Tumbiana Formation, Fortescue Group, Western Australia: *Precambrian Research*, v. 236, p. 282-296.

Crowe, S. A., Paris, G., Katsev, S., Jones, C., Kim, S.-T., Zerkle, A. L., Nomosatryo, S., Fowle, D. A., Adkins, J. F., and Sessions, A. L., 2014, Sulfate was a trace constituent of Archean seawater: *Science*, v. 346, no. 6210, p. 735-739.

Dennis, K. J., Affek, H. P., Passey, B. H., Schrag, D. P., and Eiler, J. M., 2011, Defining an absolute reference frame for 'clumped isotope' studies of CO<sub>2</sub>: *Geochimica et Cosmochimica Acta*, v. 75, no. 22, p. 7117-7131.

Eigenbrode, J. L., and Freeman, K. H., 2006, Late Archean rise of aerobic microbial ecosystems: *Proceedings of the National Academy of Sciences*, v. 103, no. 43, p. 15759-15764.

Eiler, J. M., Bonifacie, M., and Daëron, M., 2009, 'Clumped isotope' thermometry for high-temperature problems: *Geochimica et Cosmochimica Acta*, v. 73, no. 13, p. A322.

Elvert, M., Greinert, J., Suess, E., and Whiticar, M. J., 2001, Carbon isotopes of biomarkers derived from methane-oxidizing microbes at Hydrate Ridge, Cascadia convergent margin: *Geophysical Monograph-American Geophysical Union*, v. 124, p. 115-130.



Elvert, M., Suess, E., and Whiticar, M. J., 1999, Anaerobic methane oxidation associated with marine gas hydrates: superlight C-isotopes from saturated and unsaturated C<sub>20</sub> and C<sub>25</sub> irregular isoprenoids: *Naturwissenschaften*, v. 86, no. 6, p. 295-300.

Farquhar, J., Bao, H., and Thiemens, M., 2000, Atmospheric influence of Earth's earliest sulfur cycle: *Science*, v. 289, no. 5480, p. 756-758.

Fischer, W., Schroeder, S., Lacassie, J., Beukes, N., Goldberg, T., Strauss, H., Horstmann, U., Schrag, D., and Knoll, A., 2009, Isotopic constraints on the Late Archean carbon cycle from the Transvaal Supergroup along the western margin of the Kaapvaal Craton, South Africa: *Precambrian Research*, v. 169, no. 1, p. 15-27.

Flannery, D., and Walter, M., 2012, Archean tufted microbial mats and the Great Oxidation Event: new insights into an ancient problem: *Australian Journal of Earth Sciences*, v. 59, no. 1, p. 1-11.

Frantz, C., Petryshyn, V., and Corsetti, F., 2015, Grain trapping by filamentous cyanobacterial and algal mats: Implications for stromatolite microfabrics through time: *Geobiology*, v. 13, no. 5, p. 409-423.

Freeman, K. H., Hayes, J., Trendel, J.-M., and Albrecht, P., 1990, Evidence from carbon isotope measurements for diverse origins of sedimentary hydrocarbons: *Nature*, v. 343, no. 6255, p. 254-256.

Fuchs, G., 2011, Alternative pathways of carbon dioxide fixation: insights into the early evolution of life?: *Annual review of microbiology*, v. 65, p. 631-658.

Gelwicks, J. T., Risatti, J. B., and Hayes, J., 1989, Carbon isotope effects associated with autotrophic acetogenesis: *Organic Geochemistry*, v. 14, no. 4, p. 441-446.

Ghosh, P., Adkins, J., Affek, H., Balta, B., Guo, W., Schauble, E. A., Schrag, D., and Eiler, J. M., 2006, <sup>13</sup>C–<sup>18</sup>O bonds in carbonate minerals: A new kind of paleothermometer: *Geochimica et Cosmochimica Acta*, v. 70, no. 6, p. 1439-1456.

Gill, F. L., Harding, I. C., Little, C. T., and Todd, J. A., 2005, Palaeogene and Neogene cold seep communities in Barbados, Trinidad and Venezuela: An overview: *Palaeogeography, Palaeoclimatology, Palaeoecology*, v. 227, no. 1, p. 191-209.

Greinert, J., Bohrmann, G., and Elvert, M., 2002, Stromatolitic fabric of authigenic carbonate crusts: result of anaerobic methane oxidation at cold seeps in 4,850 m water depth: *International Journal of Earth Sciences*, v. 91, no. 4, p. 698-711.

Greinert, J., Bohrmann, G., and Suess, E., 2001, Gas hydrate-associated carbonates and methane-venting at Hydrate Ridge: classification, distribution and origin of authigenic lithologies: *Geophysical Monograph-American Geophysical Union*, v. 124, p. 99-114.

Grotzinger, J. P., and James, N. P., 2000, Carbonate sedimentation and diagenesis in the evolving Precambrian world, Tulsa, Oklahoma, *SEPM Special Publication*, v. 67.

Grotzinger, J. P., and Kasting, J. F., 1993, New constraints on Precambrian ocean composition: *The Journal of Geology*, p. 235-243.

Grotzinger, J. P., and Knoll, A. H., 1999, Stromatolites in Precambrian carbonates: evolutionary mileposts or environmental dipsticks?: *Annual review of earth and planetary sciences*, v. 27, no. 1, p. 313-358.

Guy, R. D., Fogel, M. L., and Berry, J. A., 1993, Photosynthetic fractionation of the stable isotopes of oxygen and carbon: *Plant Physiology*, v. 101, no. 1, p. 37-47.

Halevy, I., Johnston, D. T., and Schrag, D. P., 2010, Explaining the structure of the Archean mass-independent sulfur isotope record: *Science*, v. 329, no. 5988, p. 204-207.

Haroon, M. F., Hu, S., Shi, Y., Imelfort, M., Keller, J., Hugenholtz, P., Yuan, Z., and Tyson, G. W., 2013, Anaerobic oxidation of methane coupled to nitrate reduction in a novel archaeal lineage: *Nature*, v. 500, no. 7464, p. 567-570.

Hayes, J., 1994, Global methanotrophy at the Archean-Proterozoic transition: *Early life on Earth*, v. 84, p. 220-236.

Higgins, J., Fischer, W., and Schrag, D., 2009, Oxygenation of the ocean and sediments: consequences for the seafloor carbonate factory: *Earth and Planetary Science Letters*, v. 284, no. 1, p. 25-33.

Hikida, Y., Suzuki, S., Togo, Y., and IJIRI, A., 2003, An exceptionally well-preserved fossil seep community from the Cretaceous Yezo Group in the Nakagawa area, Hokkaido, northern Japan: *Paleontological Research*, v. 7, no. 4, p. 329-342.

Himmler, T., Freiwald, A., Stollhofen, H., and Peckmann, J., 2008, Late Carboniferous hydrocarbon-seep carbonates from the glaciomarine Dwyka Group, southern Namibia: *Palaeogeography, Palaeoclimatology, Palaeoecology*, v. 257, no. 1, p. 185-197.

Hinrichs, K.-U., Summons, R. E., Orphan, V., Sylva, S. P., and Hayes, J. M., 2000, Molecular and isotopic analysis of anaerobic methane-oxidizing communities in marine sediments: *Organic Geochemistry*, v. 31, no. 12, p. 1685-1701.

Hinrichs, K. U., 2002, Microbial fixation of methane carbon at 2.7 Ga: Was an anaerobic mechanism possible?: *Geochemistry, geophysics, geosystems*, v. 3, no. 7, p. 1-10.

Hotinski, R., Kump, L., and Arthur, M., 2004, The effectiveness of the Paleoproterozoic biological pump: A  $\delta^{13}\text{C}$  gradient from platform carbonates of the Pethei Group (Great Slave Lake Supergroup, NWT): *Geological Society of America Bulletin*, v. 116, no. 5-6, p. 539-554.

Ivanov, M., Mazzini, A., Blinova, V., Kozlova, E., Laberg, J.-S., Matveeva, T., Taviani, M., and Kaskov, N., 2010, Seep mounds on the southern Vøring Plateau (offshore Norway): *Marine and Petroleum Geology*, v. 27, no. 6, p. 1235-1261.

Johnson, C. M., Ludois, J. M., Beard, B. L., Beukes, N. J., and Heimann, A., 2013, Iron formation carbonates: Paleooceanographic proxy or recorder of microbial diagenesis?: *Geology*, v. 41, no. 11, p. 1147-1150.

Kauffman, E. G., Arthur, M. A., Howe, B., and Scholle, P. A., 1996, Widespread venting of methane-rich fluids in Late Cretaceous (Campanian) submarine springs (Tepee Buttes), Western Interior seaway, USA: *Geology*, v. 24, no. 9, p. 799-802.

Kelly, S. R., Ditchfield, P. W., Doubleday, P. A., and Marshall, J. D., 1995, An Upper Jurassic methane-seep limestone from the fossil Bluff Group forearc basin of Alexander Island, Antarctica: *Journal of Sedimentary Research*, v. 65, no. 2.

Kiel, S., Birgel, D., Campbell, K. A., Crampton, J. S., Schiøler, P., and Peckmann, J., 2013, Cretaceous methane-seep deposits from New Zealand and their fauna: *Palaeogeography, Palaeoclimatology, Palaeoecology*, v. 390, p. 17-34.

Kim, S.-T., and O'Neil, J. R., 1997, Equilibrium and nonequilibrium oxygen isotope effects in synthetic carbonates: *Geochimica et Cosmochimica Acta*, v. 61, no. 16, p. 3461-3475.

Lepot, K., Benzerara, K., Brown, G. E., and Philippot, P., 2008, Microbially influenced formation of 2,724-million-year-old stromatolites: *Nature Geoscience*, v. 1, no. 2, p. 118-121.

Liu, J., Fu, G., Song, X., Charles, S. P., Zhang, Y., Han, D., and Wang, S., 2010, Stable isotopic compositions in Australian precipitation: *Journal of Geophysical Research: Atmospheres* (1984–2012), v. 115, no. D23.

- Luff, R., and Wallmann, K., 2003, Fluid flow, methane fluxes, carbonate precipitation and biogeochemical turnover in gas hydrate-bearing sediments at Hydrate Ridge, Cascadia Margin: numerical modeling and mass balances: *Geochimica et Cosmochimica Acta*, v. 67, no. 18, p. 3403-3421.
- Marlow, J. J., Steele, J. A., Ziebis, W., Thurber, A. R., Levin, L. A., and Orphan, V. J., 2014, Carbonate-hosted methanotrophy represents an unrecognized methane sink in the deep sea: *Nature communications*, v. 5.
- Martin, W. F., 2012, Hydrogen, metals, bifurcating electrons, and proton gradients: the early evolution of biological energy conservation: *FEBS letters*, v. 586, no. 5, p. 485-493.
- Mazzini, A., Aloisi, G., Akhmanov, G., Parnell, J., Cronin, B., and Murphy, P., 2005, Integrated petrographic and geochemical record of hydrocarbon seepage on the Vøring Plateau: *Journal of the Geological Society*, v. 162, no. 5, p. 815-827.
- Mazzini, A., Svensen, H., Hovland, M., and Planke, S., 2006, Comparison and implications from strikingly different authigenic carbonates in a Nyegga complex pockmark, G11, Norwegian Sea: *Marine Geology*, v. 231, no. 1, p. 89-102.
- Michaelis, W., Seifert, R., Nauhaus, K., Treude, T., Thiel, V., Blumenberg, M., Knittel, K., Gieseke, A., Peterknecht, K., and Pape, T., 2002, Microbial reefs in the Black Sea fueled by anaerobic oxidation of methane: *Science*, v. 297, no. 5583, p. 1013-1015.
- Nitschke, W., and Russell, M. J., 2012, Redox bifurcations: mechanisms and importance to life now, and at its origin: *Bioessays*, v. 34, no. 2, p. 106-109.
- Ogihara, S., 2008, Acyclic hydrocarbons and ketones in cold-seep carbonates from central Hokkaido, northern Japan: *Geochemical Journal*, v. 42, no. 5, p. 421-427.
- Orphan, V., Ussler, W., Naehr, T., House, C., Hinrichs, K.-U., and Paull, C., 2004, Geological, geochemical, and microbiological heterogeneity of the seafloor around methane vents in the Eel River Basin, offshore California: *Chemical Geology*, v. 205, no. 3, p. 265-289.
- Orphan, V. J., House, C. H., Hinrichs, K.-U., McKeegan, K. D., and DeLong, E. F., 2002, Multiple archaeal groups mediate methane oxidation in anoxic cold seep sediments: *Proceedings of the National Academy of Sciences*, v. 99, no. 11, p. 7663-7668.
- Owen, T., Cess, R., and Ramanathan, V., 1979, Early Earth: an enhanced carbon dioxide greenhouse to compensate for reduced solar luminosity: *Nature*, v. 277, p. 640-642.

Passey, B. H., Levin, N. E., Cerling, T. E., Brown, F. H., and Eiler, J. M., 2010, High-temperature environments of human evolution in East Africa based on bond ordering in paleosol carbonates: *Proceedings of the National Academy of Sciences*, v. 107, no. 25, p. 11245-11249.

Peckmann, D.-G. J., Walliser, O. H., Riegel, W., and Reitner, J., 1999a, Signatures of hydrocarbon venting in a Middle Devonian carbonate mound (Hollard Mound) at the Hamar Laghdad (Antiatlas, Morocco): *Facies*, v. 40, no. 1, p. 281-296.

Peckmann, J., Gischler, E., Oschmann, W., and Reitner, J., 2001a, An Early Carboniferous seep community and hydrocarbon-derived carbonates from the Harz Mountains, Germany: *Geology*, v. 29, no. 3, p. 271-274.

Peckmann, J., Goedert, J., Thiel, V., Michaelis, W., and Reitner, J., 2002, A comprehensive approach to the study of methane - seep deposits from the Lincoln Creek Formation, western Washington State, USA: *Sedimentology*, v. 49, no. 4, p. 855-873.

Peckmann, J., Little, C., Gill, F., and Reitner, J., 2005, Worm tube fossils from the Hollard Mound hydrocarbon-seep deposit, Middle Devonian, Morocco: Palaeozoic seep-related vestimentiferans?: *Palaeogeography, Palaeoclimatology, Palaeoecology*, v. 227, no. 1, p. 242-257.

Peckmann, J., Reimer, A., Luth, U., Luth, C., Hansen, B., Heinicke, C., Hoefs, J., and Reitner, J., 2001b, Methane-derived carbonates and authigenic pyrite from the northwestern Black Sea: *Marine Geology*, v. 177, no. 1, p. 129-150.

Peckmann, J., and Thiel, V., 2004, Carbon cycling at ancient methane-seeps: *Chemical Geology*, v. 205, no. 3, p. 443-467.

Peckmann, J., Thiel, V., Michaelis, W., Clari, P., Gaillard, C., Martire, L., and Reitner, J., 1999b, Cold seep deposits of Beauvoisin (Oxfordian; southeastern France) and Marmorito (Miocene; northern Italy): microbially induced authigenic carbonates: *International Journal of Earth Sciences*, v. 88, no. 1, p. 60-75.

Peckmann, J., Thiel, V., Reitner, J., Taviani, M., Aharon, P., and Michaelis, W., 2004, A microbial mat of a large sulfur bacterium preserved in a Miocene methane-seep limestone: *Geomicrobiology Journal*, v. 21, no. 4, p. 247-255.

Roberts, H. H., and Aharon, P., 1994, Hydrocarbon-derived carbonate buildups of the northern Gulf of Mexico continental slope: a review of submersible investigations: *Geo-Marine Letters*, v. 14, no. 2-3, p. 135-148.

Sagan, C., and Mullen, G., 1972, Earth and Mars: evolution of atmospheres and surface temperatures: *Science*, v. 177, no. 4043, p. 52-56.

Sakai, H., Gamo, T., Ogawa, Y., and Boulegue, J., 1992, Stable isotopic ratios and origins of the carbonates associated with cold seepage at the eastern Nankai Trough: *Earth and Planetary Science Letters*, v. 109, no. 3, p. 391-404.

Sakurai, R., Ito, M., Ueno, Y., Kitajima, K., and Maruyama, S., 2005, Facies architecture and sequence-stratigraphic features of the Tumbiana Formation in the Pilbara Craton, northwestern Australia: Implications for depositional environments of oxygenic stromatolites during the Late Archean: *Precambrian Research*, v. 138, no. 3, p. 255-273.

Schoell, M., and Wellmer, F.-W., 1981, Anomalous  $^{13}\text{C}$  depletion in early Precambrian graphites from Superior Province, Canada.

Shapiro, R., and Fricke, H., 2002, Tepee Buttes: Fossilized methane-seep ecosystems: *Field Guides*, v. 3, p. 94-101.

Shapiro, R. s., 2004, Recognition of fossil prokaryotes in Cretaceous methane seep carbonates: relevance to astrobiology: *Astrobiology*, v. 4, no. 4, p. 438-449.

Stüeken, E., Buick, R., and Schauer, A., 2015, Nitrogen isotope evidence for alkaline lakes on late Archean continents: *Earth and Planetary Science Letters*, v. 411, p. 1-10.

Terzi, C., 1993, The “Calcarei a Lucina”(Lucina Limestones) of the Tuscan–Romagna Apennines as indicators of Miocene cold seep activity (Northern Apennines, Italy): *Giornale di Geologia*, v. 55, no. 2, p. 71-81.

Thauer, R. K., Kaster, A.-K., Seedorf, H., Buckel, W., and Hedderich, R., 2008, Methanogenic archaea: ecologically relevant differences in energy conservation: *Nature Reviews Microbiology*, v. 6, no. 8, p. 579-591.

Thiel, V., Peckmann, J., Richnow, H. H., Luth, U., Reitner, J., and Michaelis, W., 2001, Molecular signals for anaerobic methane oxidation in Black Sea seep carbonates and a microbial mat: *Marine Chemistry*, v. 73, no. 2, p. 97-112.

Thiel, V., Peckmann, J., Seifert, R., Wehrung, P., Reitner, J., and Michaelis, W., 1999, Highly isotopically depleted isoprenoids: molecular markers for ancient methane venting: *Geochimica et Cosmochimica Acta*, v. 63, no. 23, p. 3959-3966.

Thomazo, C., Ader, M., Farquhar, J., and Philippot, P., 2009, Methanotrophs regulated atmospheric sulfur isotope anomalies during the Mesoarchean (Tumbiana Formation, Western Australia): *Earth and Planetary Science Letters*, v. 279, no. 1, p. 65-75.

Thorne, A., and Trendall, A. F., 2001, Geology of the Fortescue Group, Pilbara Craton, Western Australia, Geological Survey of Western Australia, Department of Minerals and Energy.

Torrini, R., Speed, R., and Claypool, G., Origin and geologic implications of diagenetic limestone in fault zones of Barbados, *in* Proceedings Transactions of the 12th Caribbean Geological Conference 1990, p. 366-375.

Williford, K., Ushikubo, T., Lepot, K., Kitajima, K., Hallmann, C., Spicuzza, M., Kozdon, R., Eigenbrode, J., Summons, R., and Valley, J., 2016, Carbon and sulfur isotopic signatures of ancient life and environment at the microbial scale: Neoproterozoic shales and carbonates: *Geobiology*, v. 14, no. 2, p. 105-128.

Yoshiya, K., Nishizawa, M., Sawaki, Y., Ueno, Y., Komiya, T., Yamada, K., Yoshida, N., Hirata, T., Wada, H., and Maruyama, S., 2012, In situ iron isotope analyses of pyrite and organic carbon isotope ratios in the Fortescue Group: Metabolic variations of a Late Archean ecosystem: *Precambrian Research*, v. 212, p. 169-193.

Zeebe, R. E., and Wolf-Gladrow, D. A., 2001, CO<sub>2</sub> in seawater: equilibrium, kinetics, isotopes, Gulf Professional Publishing.

Zhang, C. L., Li, Y., Wall, J. D., Larsen, L., Sassen, R., Huang, Y., Wang, Y., Peacock, A., White, D. C., and Horita, J., 2002, Lipid and carbon isotopic evidence of methane-oxidizing and sulfate-reducing bacteria in association with gas hydrates from the Gulf of Mexico: *Geology*, v. 30, no. 3, p. 239-242.

Zhang, C. L., Pancost, R. D., Sassen, R., Qian, Y., and Macko, S. A., 2003, Archaeal lipid biomarkers and isotopic evidence of anaerobic methane oxidation associated with gas hydrates in the Gulf of Mexico: *Organic Geochemistry*, v. 34, no. 6, p. 827-836.

# Chapter 3

## Iron Mineralogy and Redox Chemistry of the Mesoproterozoic Newland Formation in the Helena Embayment, Belt Supergroup, MT

*Originally published in:*

*Slotznick, S. P., Zieg, J., Webb, S. M., Kirschvink, J. L., and Fischer, W. W., 2015,  
Iron Mineralogy and Redox Chemistry of the Mesoproterozoic Newland  
Formation in the Helena Embayment, Belt Supergroup, Montana: Northwest  
Geology, v. 44, p. 55-72.*



### 3.1 Introduction

The Mesoproterozoic era falls in the period between 1.85 to 0.85 Ga called “the boring billion”, sandwiched between the rise of multi-cellularity and animals in the Neoproterozoic and the Great Oxygenation Event and rise of oxygen in the Paleoproterozoic (Holland, 2006). However, important evolutionary developments occurred over the period with the rise of eukaryotes and macroscopic organisms (Knoll et al., 2006). The Belt Supergroup contains some of the early micro- and macrofossils that have been attributed to eukaryotes (Horodyski et al., 1989). One particularly well-studied example is found in the Greyson Shale of the Helena Embayment region in southwestern Montana (Fig. 3.1A). First identified by Charles Doolittle Walcott (1899) and later renamed (Walter et al., 1976), *Grypania spiralis* is a curved or coiled ribbon, 0.2 to 1.7 mm wide, and 6 to 14 mm in coiled diameter, and has been interpreted as eukaryotic algae as well consortia of several microscopic organisms (Horodyski et al., 1989; Knoll et al., 2006; Walter et al., 1976). Due to our understanding of eukaryotic phylogeny, the fact that most modern eukaryotes are aerobic, and the requirement of oxygen in making certain biological compounds (sterols) contained in eukaryotes, eukaryotes have been tied to oxygenic conditions (e.g. Brocks et al., 2003; Embley and Martin, 2006; Raymond and Blankenship, 2004). Therefore, there is a need to understand more about the environmental conditions in which early macroscopic organisms lived to understand the pacing of eukaryotic evolution and how it might have been aided, frustrated, or unaffected by changing environmental conditions during the Proterozoic.

However, understanding the redox state of ancient oceans has been a longstanding problem since a good oxygen barometer has not yet been developed. In general, geologists and geochemists have looked at iron, sulfur, and other redox sensitive elements as records of oxygen levels, but these approaches often give discordant answers. Some studies have suggested a fully oxygenated mid-Proterozoic ocean (Cloud, 1968; Holland, 1984, 2006), while others have suggested a stratified system with anoxic and/or euxinic deep oceans (Canfield,

1998; Poulton and Canfield, 2011). Aerobic/oxic environments are defined as having  $>80 \mu\text{M O}_2$ , anoxic/ferruginous have  $<5 \mu\text{M O}_2$ , and euxinic environments are anoxic with  $\text{H}_2\text{S}$  also present (Raiswell & Canfield 1998). Even within the subset of studies focused on samples of the Belt Supergroup, there have been conflicting hypotheses about redox conditions. Due to their preservation and low metamorphic grade (Duke and Lewis, 2010), the strata contained in the Helena Embayment, specifically the shale-dominated Newland Formation, have been the main target for understanding the ancient redox character and geochemistry of the Belt Basin. Sulfate concentrations and sulfur isotopes (Gellatly and Lyons, 2005; Luepke and Lyons, 2001; Lyons et al., 2000) as well as presence of basin-wide sedimentary laminations in the shales of the Newland and Prichard Formations similar to those found in the Black Sea (Lyons et al., 2000) were initially argued as evidence of a chemically stratified euxinic basin during deposition of the lower Belt Supergroup. Bottom water suboxic to euxinic conditions were also suggested by the high (several wt.%) organic content observed in shales (Lyons et al., 2000), and the syndepositional to early diagenetic abundant pyrite and sulfide-hosted base metal deposits of Cu, Co, and Ag (Graham et al., 2012; White et al., 2014). Others suggested the euxinic conditions forming early diagenetic pyrite were restricted to pore waters (Schieber, 1989c). In sharp contrast, iron speciation results indicate anoxic and ferruginous conditions for basinal waters of the lower Belt Supergroup (Planavsky et al., 2011). Iron speciation is a recently-developed bulk geochemical technique that uses sequential extraction to estimate proportions of different reactive iron minerals within a given rock sample (Poulton and Canfield, 2005), which are then mapped to redox conditions based on empirical calibrations from modern sediment samples. Additionally, recent nitrogen isotope measurements of samples from the Chamberlain, Greyson, and Newland Formations suggest oxygenated portions of the water column (Stüeken, 2013).

In this study, we focus on samples of the Newland Formation from the Black Butte Deposit in the Helena Embayment since previous workers

investigating mid-Proterozoic redox conditions used drill core specimens from this deposit to avoid complications of recent surface oxidation (Gellatly and Lyons, 2005; Luepke and Lyons, 2001; Lyons et al., 2000; Planavsky et al., 2011). To help reconcile the different redox interpretations and test the iron speciation results, we investigated the iron mineralogy of the Newland Formation using a range of petrographic, spectroscopic, and rock magnetic techniques that help shed light on both the paleoenvironmental processes of iron deposition in the sediments as well as post-depositional modifications to those phases. Bulk rock magnetism experiments provide sensitive techniques to identify ferromagnetic minerals, including magnetic iron sulfide phases. Magnetic iron sulfides such as pyrrhotite have not previously been identified in materials collected from the Newland Formation, but have been widely observed throughout correlative units elsewhere in the lower Belt Supergroup (e.g. Luepke, 1999; Luepke and Lyons, 2001; Slotznick et al., 2016). Much of the pyrrhotite in the rock record is interpreted to be due to the metamorphic alteration of pyrite or precipitation from high temperature fluids (Craig and Vokes, 1993; Hall, 1986); and pyrrhotite observed in Belt strata reflects both of these post-depositional processes (Luepke, 1999). Pyrite can transform to pyrrhotite beginning at 200°C (Hall, 1986) if a suitable reducing environment or organic matter is present, although some experiments suggest even lower temperature transitions are possible (Moreau et al., 2005; Raub et al., 2012). Thus the presence of pyrrhotite can provide a tool for understanding metamorphic temperatures and metasomatic conditions of the Newland Formation at the Black Butte Deposit, aiding us in recognizing if bulk geochemical proxies have been compromised by post-depositional alteration. Additionally, synchrotron-based X-ray spectroscopy provided a complimentary tool to discover and image a wide range of non-magnetic iron minerals such as chalcopyrite and pyrite while confirming the presence or absence of pyrrhotite. By applying these paired magnetic and spectroscopic techniques to the Belt Supergroup, we should be able to improve upon previous bulk geochemical

studies in deducing how iron was being deposited and transformed in the environment to reconstruct ancient redox conditions.

### **3.2 Geologic Setting**

The Helena Embayment is an E-W trending limb of the larger Belt Basin, with strata broadly correlative to three of the four stratigraphic groups recognized elsewhere in the basin: lower Belt Group, Ravalli Group, Middle Belt Carbonate Group (Fig. 3.1A; Graham et al., 2012; Winston and Link, 1993). Fine-grained siliciclastics and carbonates dominate the lower Belt in the northern part of the Helena Embayment near the Black Butte Deposit (Fig. 3.1B). The Neihart Quartzite is a basal quartz arenite sandstone with planar and trough cross-bedding, parallel lamination, and lenses of pebbles lying unconformably on early Proterozoic gneiss basement (Schieber, 1989b; Walcott, 1899). Overlying the Neihart quartzite, the Chamberlain Formation is a wavy laminated to bedded black shale, siltstone and sandstone with lenses of molar tooth hash near the top (Zieg, 1986). The Chamberlain Formation grades into the Newland Formation. The Newland Formation varies considerably in thickness across the Embayment from 610 m to over 3000 m, but is approximately 1,100 m in the region of the Black Butte Cu-Co-Ag deposit near the northern margin of the Helena Embayment (Nelson, 1963; Walcott, 1899; Zieg, 1986). The Newland Formation is subdivided into two informal members: a lower parallel-laminated shale interbedded with debris flows, turbidites, and carbonates and an upper shale with more abundant carbonate beds (Zieg, 1986). Conformably overlying the Newland Formation is the Greyson Formation of wavy laminated siltstone and dark shale, which has been assigned by some to the lower Belt Group (Graham et al., 2012; Ross and Villeneuve, 2003; Winston and Link, 1993) and by others to the Ravalli Group (Harrison, 1972; Mudge et al., 1968). The red siltstone and claystone Spokane Formation overlies the Greyson Formation as part of the Ravalli Group. The Empire Formation (Ravalli Group) and the Helena Formation (Middle Belt Carbonate) also outcrop in the Helena Embayment, but these two units are not

exposed in the Black Butte region. Instead, the Spokane is uncomfortably overlain by the Cambrian Flathead Sandstone (Fig. 3.1B; Deiss, 1935).

### ***3.2.1 Black Butte Deposit***

The strata-bound Black Butte Cu-Co-Ag Deposit occurs in the Newland Formation associated with spectacular synsedimentary pyrite-rich horizons that extend over a 25 km by 8 km area, although the main ore mineralization is localized to a fault-bounded block 8 km by 4 km (Fig. 3.1C). Three mineralized zones occur in the lower member, which are separated stratigraphically by approximately 600 m and divided by the Volcano Valley Fault (VVF). They have been named the Johnny Lee Upper Sulfide Zone (USZ), the Lowry Middle Sulfide Zone (MSZ) and the Johnny Lee Lower Sulfide Zone (LSZ) (Figs. 3.1B, 2; Zieg et al., 2013). The MSZ is still being studied and explored, and no samples were collected from it: this study focuses on the relatively well-characterized Johnny Lee deposits. Petrographic analyses have shown that the mineralization within the USZ and LSZ zones is distinct texturally and mineralogically although both contain abundant early and late diagenetic pyrite and early diagenetic barite (Graham et al., 2012). Much of the early diagenetic pyrite is framboidal or occurs in small fine-grained aggregates including small circular tubes proposed to reflect pyritized microbial filaments (McGoldrick and Zieg, 2004) and chimneys (Present et al., in review). The early diagenetic pyrite is interpreted to form from fault controlled iron-rich fluids moving through the sedimentary pile and venting at or just below the sediment surface at low temperatures (Graham et al., 2012; White et al., 2014), or from diagenetic transformations of detrital iron oxides under conditions of microbial sulfate reduction in shallow pore fluids (Schieber, 1989c). Based on framboidal textures, a general lack of base metal enrichments, and S isotopes, several authors have extended these arguments to suggest water-column precipitation of pyrite from euxinic bottom waters (Lyons et al., 2000; White et al., 2014). A secondary diagenetic phase, especially prevalent in the USZ, formed overgrowth rims and coarse cements of pyrite. Sulfur isotope data implies the

sulfur for these secondary pyrites was sourced from seawater (Zieg and Leitch, 1999). Some galena and sphalerite phases occurring in the USZ are tied to diagenetic fluids, but these minerals are not prevalent especially when compared to surrounding non-mineralized strata; Pb and Zn are not yet recognized in economic concentrations (Graham et al., 2012; White et al., 2014).

Although many Co-Ni-As-Cu rich sulfides formed relatively early during diagenesis in the USZ, a third mineralization event prior to lithification in both zones created most of the chalcopyrite as well as some chalcocite, bornite, tennentite, cobaltite, and chlorite (LSZ only) while remobilized base metals in the USZ formed siegenite (White et al., 2014). The LSZ contains a higher percentage of chalcopyrite than the USZ, although more mineralization results in a higher tonnage for the USZ. Thermodynamic calculations suggest these hydrothermal fluids were between 125°C and 225°C (White et al., 2014). In late post-lithification events, dolomite and ankerite (USZ only) precipitated within the mineralized zones (Graham et al., 2012).

### 3.3 Methods

In this study, samples from near both the USZ and LSZ were collected and analyzed to understand the richness in iron mineralization processes in the Newland Formation in this part of the Belt basin (Fig. 3.2.) Twenty-five quarter-core block samples were collected in July 2013 from 4 different cores housed in the Tintina Resources, Inc. core shed, White Sulphur Springs, MT. Samples were cut using a non-magnetic brass blade into 3 cm by 2 cm billets, and made into polished thin or thick sections for further analyses. Table 3.1 summarizes the sample data for the 11 samples from 10 quarter-cores that were analyzed in detail.

Non-destructive rock magnetic experiments were performed on thick sections or billets returned from thin sections for all 11 samples using a 2G Enterprises SQUID magnetometer following the RAPID protocols, and analyzed using the RAPID Matlab (The Mathworks, Inc.) scripts (Kirschvink et al., 2008). The RAPID protocol used here includes measurements of alternating field (AF)

demagnetization of the natural remanent magnetization (NRM), anhysteretic remanent magnetization (ARM) acquisition and demagnetization, isothermal remanent magnetization (IRM) acquisition and demagnetization, backfield IRM acquisition, and rotational remanent magnetization (RRM) acquisition and demagnetization. Combined, these measurements quantify fundamental properties that can be used to distinguish different ferromagnetic minerals present in the samples (e.g. Peters and Dekkers, 2003). The destructive rock magnetic technique of KappaBridge thermal susceptibility was measured on neighboring specimens for one sample using an AGICO MFK1-FA KappaBridge and resulting data were analyzed in Matlab. Ultra-high resolution scanning SQUID Microscopy (UHRSSM) was performed on 5 of the sections with 100  $\mu\text{m}$  pixels after giving them an IRM to locate and image ferromagnetic grains at the microscale.

Additional chemical imaging techniques were employed to study the non-magnetic iron- and sulfur-bearing mineral phases. Transmitted and reflected light microscopy was used to observe petrographic textures and preliminarily identify mineralogy. High-energy synchrotron-based microprobe X-ray fluorescence (XRF) at 13500 or 20200 eV was used to map elemental abundances with 35  $\mu\text{m}$  pixels across regions in 10 representative sections at beamline 10-2 at the Stanford Synchrotron Radiation Lightsource. Additionally, synchrotron-based X-ray near-edge absorption spectroscopy (XANES/XAS) at sulfur energies (2400-2500 eV) was paired with redox imaging at the S K-edge using a new lower energy X-ray microprobe (beamline 14-3) to collect both full spectra and multiple energy maps with 4  $\mu\text{m}$  resolution and determine the mineral chemistry (oxidation state, orbital electronics, type and number of neighbors) while retaining textural information. Differences in the shape of these K-edge absorption spectra allow us to easily distinguish between a wide range of materials (Fleet, 2005; Mosselmans et al., 1995). Paired with end-member XANES spectra, the absorptions at multiple excitation energies in diagnostic regions of the XANES spectrum were collected and fit to create large maps of the mineralogy in samples. Principle component analysis of this multiple energy data was used to target and check for

additional minerals. Chalcopyrite and pyrrhotite have similarities in their S K-edge spectra and thus the elemental maps made by high-energy XRF at 10-2 were used to evaluate the abundance of Cu. Synchrotron XANES and XRF analyses were performed at the Stanford Synchrotron Radiation Lightsource. Additional petrographic observations and mineral identifications were made using a ZEISS 1550VP FESEM, scanning electron microscope in the Caltech GPS Division Analytical Facility. This instrument is paired with an Oxford X-Max SDD X-ray Energy Dispersive Spectrometer (EDS) system and was used to determine X-ray spectra of elemental abundance at sub-micron sized spots on 3 thin sections to confirm the presence of chalcopyrite and galena implied from synchrotron data.

### 3.4 Results

Rock magnetic techniques both confirmed previous observations (Graham et al., 2012; White et al., 2014) and highlighted the presence of iron mineralization not previously described in the Newland Formation shales at the Black Butte Deposit.

#### 3.4.1 Rotational Remanent Magnetization (RRM)

The presence of RRM can be used to identify magnetic iron-sulfide phases like pyrrhotite, although the sensitivity limits are not well understood (Snowball, 1997; Thomson, 1990). RRM is acquired during the application of an alternating field of 90 mT (950 Hz) perpendicular to the spin axis of a sample while it is rotating at a given speed. Studies have shown that  $B_{RRM}$  (normalized field strength of acquired RRM) varies with speed and direction of rotation so the sample is rotated clockwise and counterclockwise from 0 to 20 revolutions per second, rps (e.g. Suzuki et al., 2006). Two samples, T029-56 and T095-140.36, indicated strong evidence for magnetic iron sulfides,  $B_{RRM} > \pm 20 \mu\text{T}$  at 5 rps (Potter and Stephenson, 1986; Suzuki et al., 2006), while the rest of the samples showed no signs of RRM with  $B_{RRM} \approx 0$  (Fig. 3.3A). Importantly, UHRSSM imaging revealed the ferromagnetic grains in these two samples to be located in



epoxy-filled holes (Figs. 3.4CD) created either for standard emplacement of a pyrite grain for textural S isotope analyses (Present et al., in review) or to fill porous textures when making thin sections, demonstrating that these grains are contaminants (metal alloys can produce strong RRM, Snowball, 1997). Thus, there is no evidence of magnetic iron sulfides in the Newland Formation, including the mineralized zones associated with the Black Butte Deposit.

### ***3.4.2 Coercivity of Remanence Acquisition***

The coercivity of remanence acquisition ( $H_{cr'}$ ), defined as the magnetic field required to permanently flip half of the magnetic moments in a mineral, is a useful property to differentiate ferromagnetic minerals (Peters and Dekkers, 2003). Overall a measurement of how easily a mineral becomes magnetized, it is determined by taking the derivative of the acquisition of IRM curve and deconvolving the spectra into distinct peaks of different field strengths, which are the different coercivities of the mineral assemblage (Heslop et al., 2002; Robertson and France, 1994). Goethite is easily identified with coercivities over 1000 mT, and the range of 140-800 mT is unique for hematite. However, extensive data collection has shown that the coercivity ranges for hematite, magnetite, titanomagnetite, greigite, and pyrrhotite overlap between 16-140 mT—though the averages of hematite (270 mT), pyrrhotite (53 mT), greigite (75 mT) are higher than those for magnetite and titanomagnetite (30 mT). Thus mineral identifications solely using  $H_{cr'}$  for identification have some margin of error and benefit from additional analyses (Table 3.2).

Notably, three groups of ferromagnetic mineralogy can be separated based on  $H_{cr'}$  and stratigraphic/lithologic information (Fig. 3.3B). All of the samples collected far outside the strongly mineralized sulfide zones (T095-38, T095-53, T112-334, T112-384) primarily contain finely disseminated pyrite and show very similar mid-coercivity peaks interpreted to be magnetite. Sample T095-38 also shows a striking high-coercivity goethite peak; this sample contains fractures mineralized with oxides seen in hand sample and described in the core log for this

stratigraphic height. Sample T029-61.21 has early diagenetic pyrite textures with minimal secondary recrystallization and contains the same magnetite mid-coercivity peak as the four samples described above. The other three samples exhibiting early diagenetic textures (T029-56, T029-140.36, T095-389), including the two samples with known ferromagnetic contamination, have slightly higher coercivity spectra. While T095-389 did not show RRM, it does have an epoxied hole with a standard, which could be contaminated by a ferromagnetic mineral/alloy similar to samples T029-140.36 and T095-389. Therefore we interpret the characteristic slightly higher  $H_{cr}$  peak of these three samples to be due to contamination and not representative of early textures. Lastly, three samples display multiple generations of sulfide-bearing minerals including late displacive and replacive textures (T095-156, T101-389, T101-390). These samples show a range of mid- to low-coercivity spectra suggesting larger grain size and/or multi-domain magnetite (Peters and Dekkers, 2003).

### ***3.4.3 Lowrie-Fuller Test***

To further examine the grain size and magnetic domain state, we employed a rock magnetic technique called the Lowrie-Fuller test—a measure of ferromagnetic grain size based on the relative stability of IRM versus ARM to applied demagnetizing AF (Lowrie and Fuller, 1971; Xu and Dunlop, 1995). In single domain grains, ARM is more stable and less easily demagnetized than IRM, while in larger multidomain grains, IRM is more stable and less easily demagnetized using AF than ARM. Although the exact physics are poorly understood, if the ARM is consistently stronger than the IRM then single domain or pseudo single domain ( $<10\ \mu\text{m}$ ) particles probably represent the majority of the magnetized minerals in a sample. While most of the samples appear to contain single-domain or pseudo-single domain particles, T095-156 (which had low coercivity spectra) does contain multi-domain grains (Fig. 3.3C). T095-38 also is shown to contain multi-domain grains, but this sample contains goethite, which would bias the Lowrie-Fuller test toward multi-domain results. From this data,

multi-domain magnetite is more common in samples with replacive textures suggesting it could have formed from recrystallization or authigenic precipitation—this can be tested if it shows a chemical remanent magnetization.

#### ***3.4.4 Fuller Test of NRM***

Magnetite appears to be the primary ferromagnetic component in the majority of the Newland Formation shale samples. As a result, we can apply a useful rock magnetic experiment called the Fuller Test of NRM to determine if the magnetization carried by the magnetite is detrital or chemical in origin. This test uses the ratio of the NRM:IRM compared to empirical calibrations and synthetic ARM:IRM relationships of a given sample (Fuller et al., 1988; Fuller et al., 2002). Empirical calibrations on rocks with magnetite as the primary ferromagnetic mineral suggest that the weak NRM:IRM ratios of 1:1000 occur in sedimentary rocks with detrital remanent magnetization formed during primary deposition and ratios of 1:10 represents chemical remanent magnetization when magnetite has grown *in situ* or authigenically in a sample (Fuller et al., 2002). The ARM:IRM curve is used for comparison to demonstrate which changes in the shape of the curve are characteristic of the sample. Most samples of the Newland Formation show an NRM:IRM ratio of 1:1000, which is consistent with weak detrital remanent magnetization (Fig. 3.3D). T112-334 shows indication of chemical remanent magnetization, in which magnetite is an authigenic phase that either grew during early diagenesis or during a later diagenetic mineralization. UHRSSM maps showed the locations of disperse dipoles of ferromagnetic grains throughout samples in fine-grained material, located close to and far from secondary cross-cutting textures, consistent with a detrital origin (Figs. 3.4AB). However, due to the sub-micron size of these grains, the ferromagnetic minerals in the regions with dipoles could not be visualized via petrography.

#### ***3.4.5 KappaBridge Thermal Susceptibility***

To further study the magnetite, a neighboring sample from T101-389 was used for destructive thermal susceptibility experiments using a KappaBridge. Powdered rock was slowly heated from -190°C to 700°C and then cooled to 40°C while the susceptibility from a weak induced field was measured at 20 second intervals. Susceptibility measures the ability of a sample to be magnetized in the presence of an applied field. Thus it is a magnetic measurement that integrates the entire assemblage of minerals in a sample, although ferromagnetic minerals usually dominate the signal. Changes in susceptibility during heating and cooling are produced by mineralogical transformations within the sample. A drop in susceptibility at 580°C indicates the presence of magnetite as it becomes paramagnetic at its Curie temperature (Fig. 3.5A). The low-temperature Verwey transition typical for magnetite at -150°C as it transforms from weakly magnetic monoclinic magnetic structure and to ferromagnetic cubic structure was not observed in this sample; either it was suppressed due to low abundance with other phases dominating the signal, or the magnetite contains a small weight percent titanium (Kozłowski et al., 1996; Moskowitz et al., 1998). A slight drop in susceptibility at 80°C is suggestive of goethite decomposing and reacting with sulfur to form pyrite or decomposition of titanomagnetite (Charilaou et al., 2011; Minyuk et al., 2013). Although the typical pyrite/chalcopyrite decomposition peak to magnetite is not seen (Li and Zhang, 2005; Minyuk et al., 2013), some new magnetite and a substantial amount of pyrrhotite were formed after heating to 700°C in an argon atmosphere based on the fact that the cooling curves increase in susceptibility during cooling with distinct peaks at 580°C and at 320°C the respective Curie temperatures for those minerals (Fig. 3.5B). The creation of these minerals suggests there were non-magnetic iron sulfides in these samples that transformed into magnetic minerals during the heating process.

#### ***3.4.6 X-ray Spectroscopy***

Iron sulfide phases were visually identified in all of the samples using light microscopy. We used X-ray spectroscopy, specifically XANES and XRF, to

evaluate the exact chemical composition and crystal structure of these phases (Table 3.2). Ferrous disulfide was identified as the major sulfide-bearing phase in all the samples (Fig. 3.6). The ferrous disulfide minerals marcasite and pyrite have similar S K-edge spectra using XANES and can only be readily distinguished by the Fe L-edge (Mosselmans et al., 1995) or X-ray diffraction, which were not measured here. However, petrography shows that the disulfides phases present in these samples are pyrite. Chalcopyrite was observed as a major component of T101-389 (Figs. 3.4E, 3.6). Sulfate salts were also identified in many of the samples including laths of barite that show differential compaction of sedimentary laminae (Figs. 3.4F, 3.6). However, in the samples with disseminated pyrite, small domains of sulfate (10-20  $\mu\text{m}$  in size) were found both alone and associated with pyrite, suggesting some of the sulfate minerals could be iron sulfates instead of barite (Figs. 3.4GH, 3.6). EDS and high-energy XRF maps were used to confirm the presence of chalcopyrite (as opposed to pyrrhotite); however, the XRF maps also highlight interesting patterns in base metal mineralization. Some replacive pyrite grains contain greater amounts of As, Pb, Zn, or Cu (Figs. 3.7DEG), while other regions hosted chalcophile metals as dominant cations in sulfide phases like Cu in chalcopyrite (Figs. 3.7A-F,H). Microprobe X-ray spectroscopy paired mapping capabilities, coupled with traditional petrographic and bulk chemical techniques, provide an exciting new tool for mineral analysis opening new avenues for inquiry into trace metal abundances, redox states and gradients, and mineral phase identification.

### 3.5 Discussion and Conclusions

Bulk rock magnetic techniques employed in this study confirm the absence of pyrrhotite in shales of the Newland Formation near the Black Butte Deposit, in contrast to its ubiquitous presence in correlative units at higher metamorphic grades to the northwest (Slotznick et al., 2016). This result confirms that these rocks have not been heated to very high temperatures, and while hydrothermal fluids did cause overprinting and recrystallization of sulfide

phases, no pyrrhotite was formed with this mineralization. This is important for bulk geochemical studies such as iron speciation (Planavsky et al., 2011) because pyrrhotite may be misplaced in sequential chemical extraction with the magnetite fraction and/or result in incorrect iron calculations due to its unique chemistry during the pyrite extraction—both could make a basin appear more ferruginous than it was by incorrectly identifying the iron mineralogy (Asael et al., 2013; Schumann et al., 2012)). Samples collected far outside the massive sulfide mineralization zones contain early diagenetic disseminated pyrite grains (Schieber, 1989a); copper, zinc, and lead sulfides are rare in these areas but their presence still signals some mineralization extends beyond the regions of economic interest. Sulfide phases tied to these hydrothermal fluids should be taken into account when using Belt strata to interpret the ancient redox conditions and processes operating in the Belt Basin, because these phases show iron was mobile and likely advected from elsewhere in the sediment pile. The hydrothermal fluids could have also sourced iron for some of the magnetite present in the samples and/or been responsible for recrystallization processes.

The identification of magnetite in Newland Formation shales provides important insights into the redox character and mode of iron delivery in this part of the Belt Basin. Rock magnetic experiments indicate that magnetite is primarily detrital in origin, with limited evidence for authigenic magnetite in some samples. Though pyrite is commonly the most abundant iron-bearing mineral present in these diagenetically stabilized lithologies, detrital magnetite represents an important sedimentary vector for iron delivery to this basin that is not a direct measure of redox conditions in seawater. Furthermore, detrital iron oxides might bias iron speciation data toward compositions that appear more anoxic and ferruginous (Planavsky et al., 2011); during deposition Belt Basin waters could have either been more oxic or more euxinic depending on the relative abundances of these oxides and other iron-bearing minerals. Petrography and X-ray imaging reveal that pyrite is ever-present as small framboids and disseminated grains exhibiting textures that are consistent with the formation of much of this pyrite in

the water column or in sediments during early diagenesis (Graham et al., 2012; Schieber, 1989a; Wilkin et al., 1996). We speculate that detrital iron oxides were an important source of reactive iron for early pyrite formation (e.g. Canfield and Berner, 1987; Reynolds et al., 2000; Schieber, 1989c). Many samples (not just limited to economically meaningful sulfide mineralization zones) show additional sulfide phases in late diagenetic textures that mark iron sourced by hydrothermal fluids. If iron sources did not limit early pyrite formation more broadly, perhaps this was limited by the abundance of  $H_2S$  in the bottom water, bacterial sulfate reduction/sulfur oxidation rates, and/or sedimentation rates. More work is needed to better understand the interplay between these factors (Present et al., in review), but what is clear at present is that we do not see clear evidence for the ferruginous water column conditions during the depositional of Newland Formation shales put forward on the basis of iron speciation data (Planavsky et al., 2011).

Based on our observations, we hypothesize that bottom waters in Helena Embayment during the deposition of the Newland Formation were suboxic or possibly euxinic (Gellatly and Lyons, 2005; Lyons et al., 2000), and that detrital fluxes played an important role in delivery of iron into the Helena Embayment, much of which was transformed into pyrite during sulfate reduction associated with early diagenesis of these organic-rich sediments (Lyons et al., 2000; Strauss and Schieber, 1990). This is a similar mode of iron deposition and pyrite production today in modern euxinic basins and anoxic pore waters in marine sediments (e.g. Berner, 1984), and implies a degree of continuity of redox conditions and processes operating in large sedimentary basins over the past one and a half billion years.

### **3.6 Acknowledgements**

We thank John Grotzinger, Ted Present, Andy Knoll, Ken Williford, and the members of the 2013 Agouron Field Course for assistance with sample collection. Support for this work was provided by the Agouron Institute, Tobacco

Root Geological Society Scholarship, Belt Association Student Research Grant, the David and Lucile Packard Foundation (W.W.F.), NSF Graduate Research Fellowship program (S.P.S.), and NASA Earth and Space Fellowship (S.P.S.). Portions of this research were carried out at the Stanford Synchrotron Radiation Lightsource, a Directorate of SLAC National Accelerator Laboratory and an Office of Science User Facility operated for the U.S. Department of Energy Office of Science by Stanford University.



### 3.7 Tables

**Table 3.1: Detailed Sample Data**

Sample Name	Drill Core	GPS of Drill Core Collar	Sulfide Zones	Depth of Billet (m)	Stratigraphy	Description
T029-56	SC11-029	N 46° 46' 54.8" W 110° 54' 46.33"	USZ, LSZ	56.475- 56.50	Upper Newland right above USZ	Early unfilled circular tube network of iron sulfides 1-4mm in diameter with .5mm thick walls in larger massive sulfide zone
T029-61.21	SC11-029	N 46° 46' 54.8" W 110° 54' 46.33"	USZ, LSZ	61.205- 61.235	Upper Newland right above USZ	Early diagenetic barite laths with differential compaction of laminated dolomitic shale with intergrown sub-parallel iron sulfide blebs rimmed with altered barite
T095-38	SC11-095	N 46° 46' 44.76" W 110° 55' 32.7"	USZ	38.70- 38.76	Upper Newland far above USZ	Grey laminated silty dolomitic shale with abundant dolomite veins and iron oxide along fracture surfaces
T095-53	SC11-095	N 46° 46' 44.76" W 110° 55' 32.7"	USZ	53.50- 53.56	Upper Newland far above USZ	Black laminated dolomitic shale with disseminated iron sulfides
T095-140.36	SC11-095	N 46° 46' 44.76" W 110° 55' 32.7"	USZ	140.375- 140.405	Upper Newland	Early diagenetic iron sulfide nodules with differential compaction, laminae, and wavy laminae in larger massive sulfide zone, minor altered barite
T095-156	SC11-095	N 46° 46' 44.76" W 110° 55' 32.7"	USZ	156.815- 156.845	Upper Newland	Large iron sulfide bleb within cross-cutting late iron sulfide band in micro-faulted grey laminated dolomitic shale
T095-389	SC11-095	N 46° 46' 44.76" W 110° 55' 32.7"	USZ	389.22- 389.255	Upper Newland right above USZ	Grey laminated dolomitic shale with small debris flows and early iron sulfide broken tubes, complete to disaggregated framboids, and fine-grained laminations
T101-389	SC12-101	N 46° 46' 53.15" W 110° 54' 21.17"	LSZ	389.935- 389.96	Lower Newland in LSZ	Multiple generations of cross-cutting sulfides (up to 3mm blebs) in heavily recrystallized dolomite and shale within larger massive sulfide zone
T101-390	SC12-101	N 46° 46' 53.15" W 110° 54' 21.17"	LSZ	390.085- 390.11	Lower Newland in LSZ	Multiple generations of cross-cutting sulfides in heavily recrystallized dolomite and shale within larger massive sulfide zone
T112-334	SC12-112	N 46° 46' 51.53" W 110° 53' 58.67"	LSZ	334.62- 334.64	Lower Newland in Volcano Valley Fault Shear Zone	Black laminated shale with disseminated iron sulfides
T112-384	SC12-112	N 46° 46' 51.53" W 110° 53' 58.67"	LSZ	384.43- 334.49	Lower Newland right below LSZ	Sheared black and grey silty shale with intergrown iron sulfide blebs (<1mm) and disseminated iron sulfides

Table 3.2: Mineralogical Identifications from Samples of Newland Formation from Black Butte Deposit

Sample name	Bulk Techniques				S XANES and EDS							High-Energy XRF*			
	Mag	Goe	Pyr	Cont	Py	Pyr	FerS	CuPy	Cov	Gal	SO4	AsPb	Cu	Zn	Ni
T029-56				X	X†			X†	X†	X†		X	X	t	
T029-61.21	X				X						X	t	X	X	
T095-38	X	X										X	X	X	t
T095-53	X				X						X	X	X	X	t
T095-140.36				X								X			
T095-156	X				X							t			
T095-389				X	X†			X†	X†	X	X	X			
T101-389	X				X		X	X				X	X	X	
T101-390	X											X	X	t	
T112-334	X				X						X	X	X	X	t
T112-384	X											t	t		t

Abbreviations: XANES = X-ray Absorption Near Edge Spectroscopy, EDS = X-ray Energy Dispersive Spectroscopy, XRF = X-ray Fluorescence, Mag = Magnetite, Goe = Goethite, Pyr = Pyrrhotite, Cont = Contamination, Py = Pyrite, FerS = Ferric Disulfide, CuPy = Chalcopyrite, Cov = Covellite, Gal = Galena, SO4 = Sulfate often Barite, AsPb = Arsenic and/or Lead

\*For XRF, t=trace, X = important mineral constituent

† Data from Present et al., in review based on reflected light petrography

### 3.8 Figures

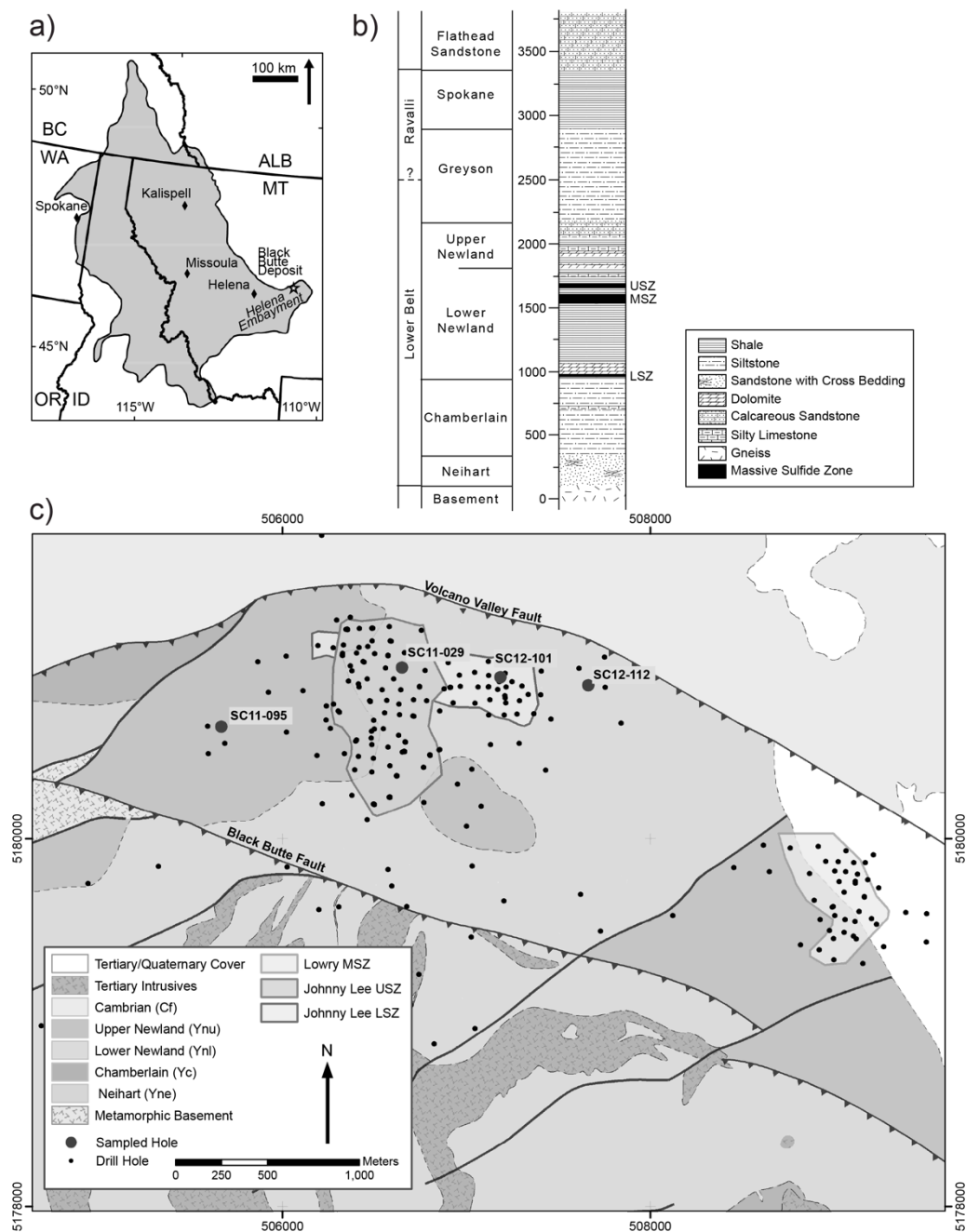


Figure 3.1: a) Map showing the extent of Belt Supergroup outcrops and the location of the Black Butte Deposit within the Helena Embayment. b) General stratigraphic column of Belt Supergroup strata in the Black Butte Deposit region of the Helena Embayment with height in meters. Note: USZ = Upper Sulfide Zone, MSZ = Middle Sulfide Zone, LSZ = Lower Sulfide Zone. c) Geologic Map of the Black Butte Deposit region with locations of all drill cores drilled by Tintina Resources Inc. and Cominco American Inc. and labels for the drill cores that were sampled in this study.

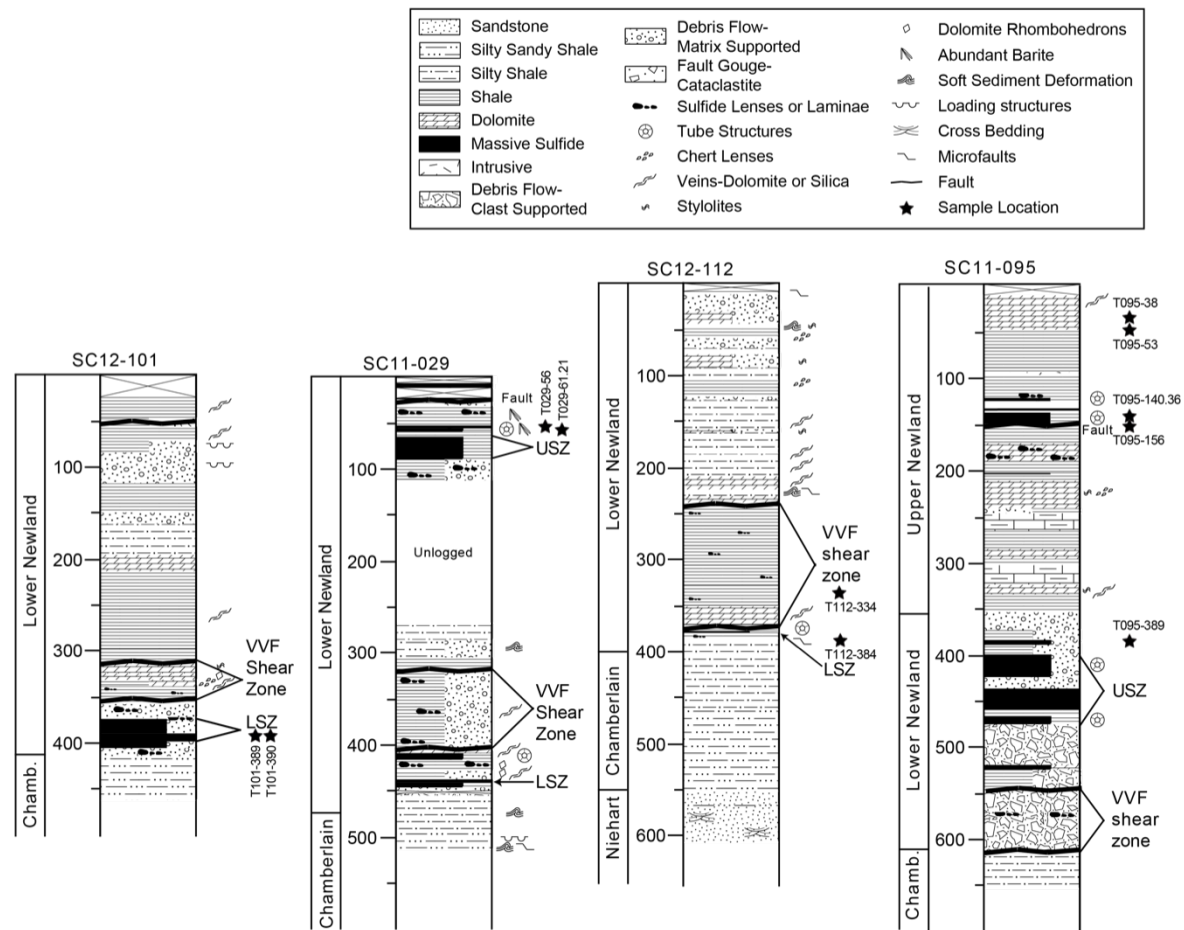


Figure 3.2: Lithostratigraphic columns of the drill cores from the Black Butte Deposit area examined in this study. Labeled black stars mark the stratigraphic positions of samples analyzed. Cores are not aligned by stratigraphic datum, and core depth is in meters.

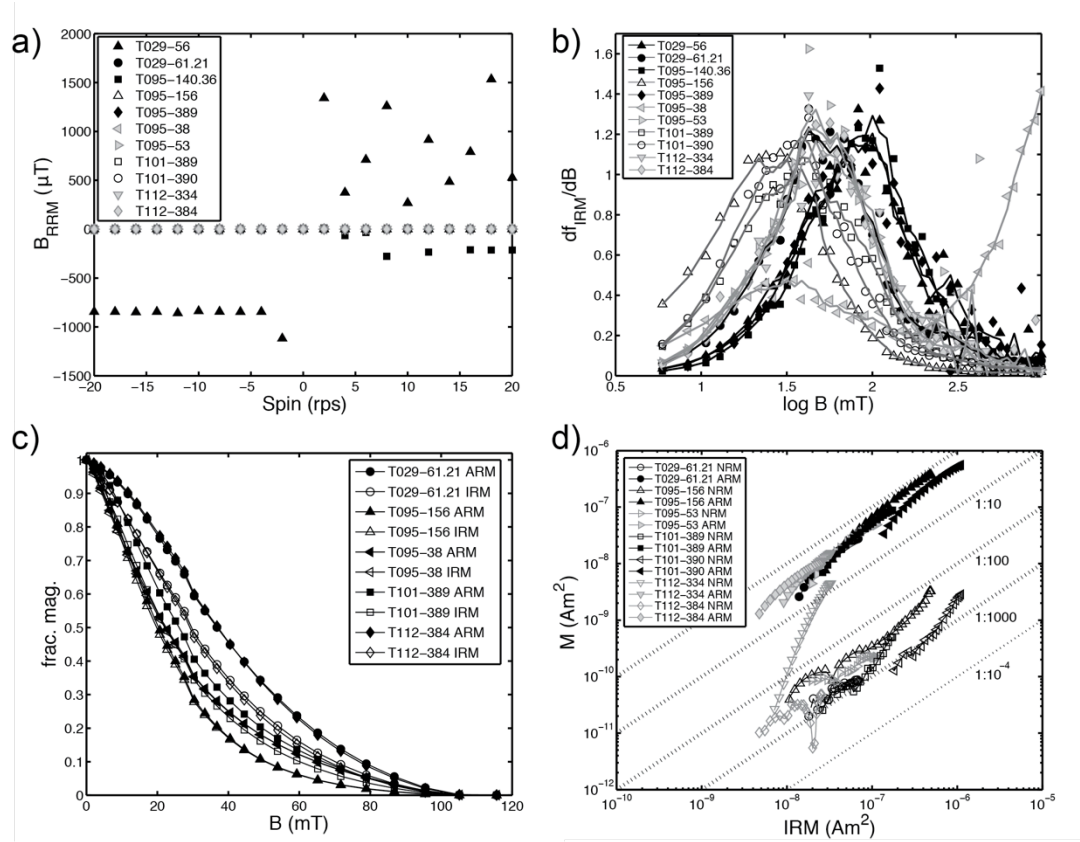


Figure 3.3: Rock magnetic data from shale samples of the Newland Formation. a) Rotational remanent magnetization (RRM) data to assess the presence or absence of magnetic iron sulfide phases. Negative spin speed indicated counter-clockwise rotation around the spin axis when the perpendicular alternating field is applied. All 11 samples are plotted, but only 2 of the samples are clearly visible since most of the samples have  $B_{RRM} \approx 0$  at all spin speeds. b) Data showing the derivative of the isothermal remanent magnetization (IRM) of all samples to determine the coercivity of remanence ( $H_{cr}'$ ) and from this information the ferromagnetic mineralogy. The applied field (B, x-axis) at the peaks of the spectra is the  $H_{cr}'$ . c) Results of representative samples from the Lowrie-Fuller test to inform domain state and grain size based on the relative strength of the IRM vs. the ARM curves as measured by the fraction of total magnetization (frac. mag., Y-axis) when a specific demagnetizing field is applied (B, x-axis). d) Results from the Fuller test to provide insight into the origins (detrital, chemical, thermal) of magnetization based on the ratio of the NRM (y-axis) to IRM (x-axis). The ratio of ARM:IRM is also plotted using the same axes.

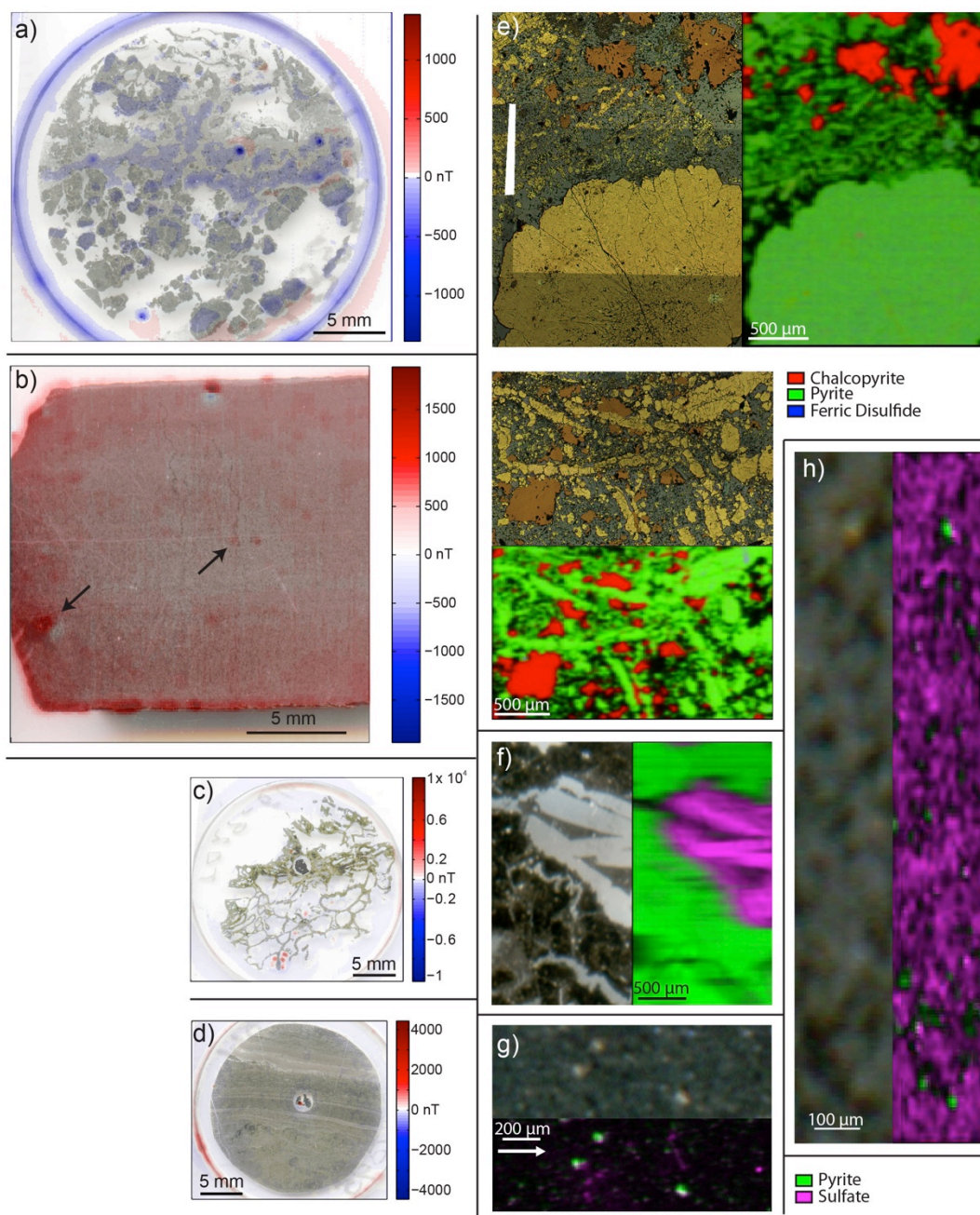


Figure 3.4: Parts a-d show UHRSSM magnetic microscopy images of ferromagnetic minerals. Hot and cool colors reflect magnetic vectors out of and into the page, respectively. a) Map of T101-389 showing scattered dipoles focused in fine-grained regions. b) Scattered dipoles including some that trend with post-depositional crosscutting features, such as pointed out by arrows, in T112-334. c) Image of T029-56 showing dipoles in epoxied holes around iron sulfide tube network that reflect contaminant phases introduced via standard preparation. d) Map of T095-140.36 showing single strong dipole in epoxied drill

hole with pyrite standard that reflect contaminant phases introduced during preparation. Parts e-h show paired reflected light microscopy or photograph on the left-top and multiple-energy maps fit to minerals using end-member S XANES spectra on the right-bottom. Samples are oriented with correct up direction; an arrow marks the up direction for part c e) Two mapped regions of T101-389 contain multiple generations of sulfide phases including chalcopyrite, pyrite, and a unique ferric disulfide. f) Map of T026-61.21 with barite laths surrounded by early diagenetic pyrite in layers. g) Disseminated pyrite grains with associated sulfate and distinct sulfate domains in T095-53. h) Disseminated pyrite with low abundance sulfur in matrix in T112-334. Scale bar provided for each image or image pair.



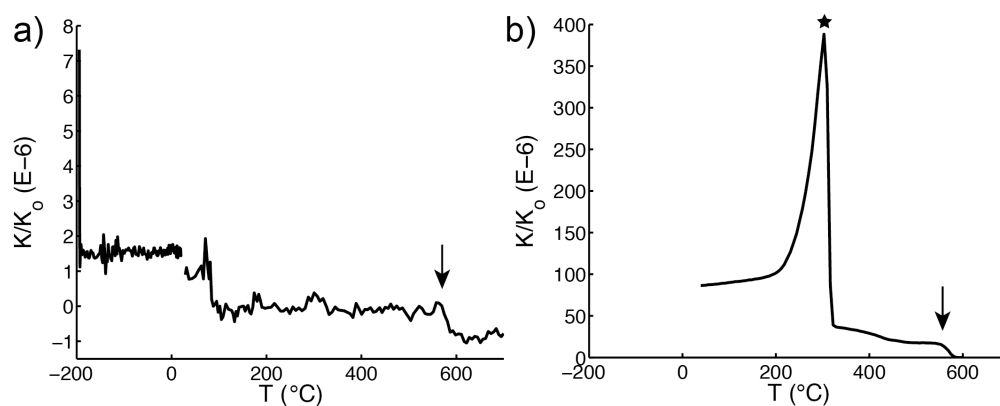


Figure 3.5: KappaBridge results for a representative shale sample, T101-389. a) Magnetic susceptibility during heating from  $-190^{\circ}\text{C}$  to  $700^{\circ}\text{C}$ . b) Magnetic susceptibility during cooling from  $700^{\circ}\text{C}$  to  $23^{\circ}\text{C}$ . Note the different y-axis scale as there is increased susceptibility during this cooling phase. Data are normalized to the blank, an empty specimen holder measurement. Arrows mark the Curie temperature of magnetite ( $580^{\circ}\text{C}$ ) while the star marks the Curie temperature of pyrrhotite ( $320^{\circ}\text{C}$ )



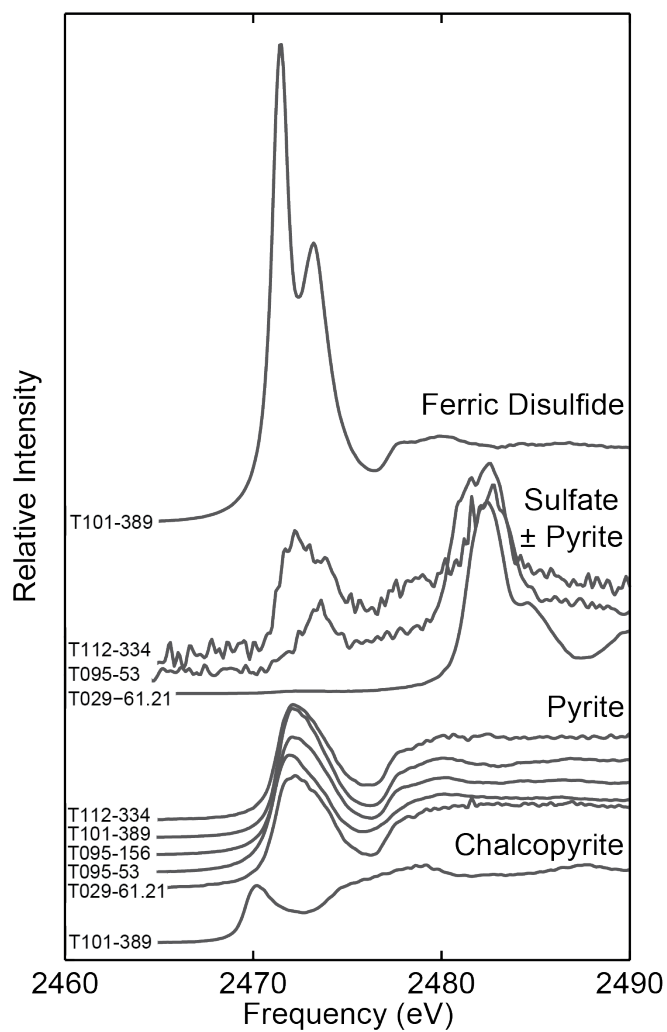


Figure 3.6: Synchrotron S K-edge XANES spectra for phases identified in all samples. An unnamed unique mineral, a ferric disulfide not previously found in natural samples, is identified based off its K-edge spectra, which shows  $\text{Fe}^{+3}$  bonding with di-sulfide valence sulfur.

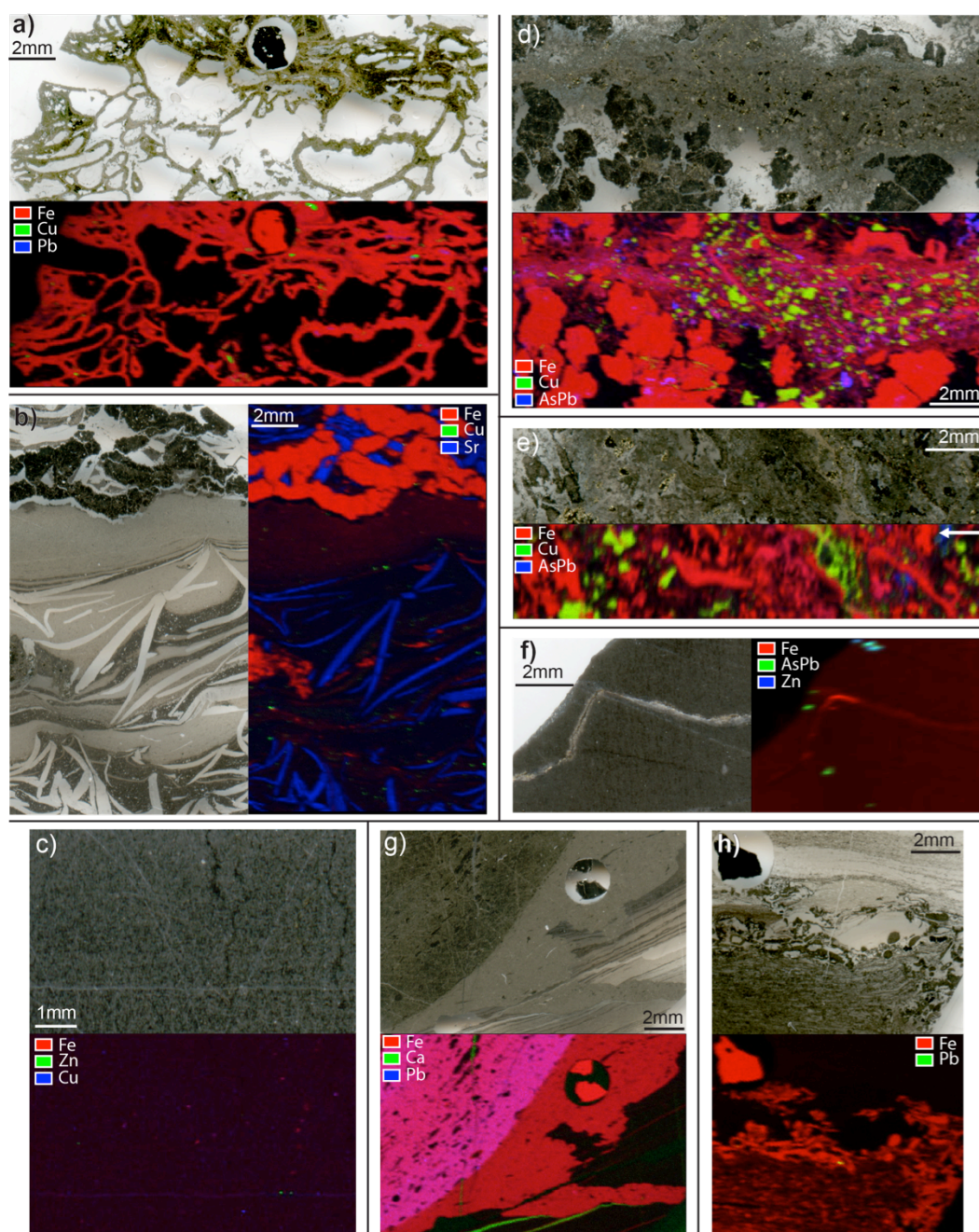


Figure 3.7: High-Energy XRF maps of metal abundances (right-bottom) shown alongside a light scan of a given sample in thick or thin section (left-top). Samples are oriented with correct up direction; an arrow marks the up direction for part e. a) Unfilled tubular network of iron sulfide cements with small inclusions of Pb- and Cu-bearing minerals in T029-56. b) Early diagenetic and recrystallized barite containing trace Sr with sub-parallel pyrite blebs and small Cu-bearing minerals in T029-61.21. c) Disseminated pyrite with distinct Zn and Cu minerals that show mineralization associated both along lamination and crosscutting features in T112-334. d) Multiple generations of sulfides including

pyrite and chalcopyrite with As- and Pb-rich grains, zones of finely disseminated grains, and zones within euhedral grains in T101-389 e) Closer look at multiple generations of iron sulfides and chalcopyrite with As- and Pb-rich grains and zones in larger grains in T101-390. f) Dolomite vein containing iron oxide with As-, Pb-, and Zn-rich minerals associated with smaller non-dolomitized fractures and/or laminations in T095-38. g) Vertical dolomitic veins cut Pb-rich pyrite bleb within a crosscutting pyrite aggregate in a laminated dolomitic shale in T095-156. h) Intraformational detrital iron sulfides parallel to, and deforming shale laminates with small amounts of galena in T095-389.

### 3.9 References

- Asael, D., Tissot, F. L., Reinhard, C. T., Rouxel, O., Dauphas, N., Lyons, T. W., Ponzevera, E., Liorzou, C., and Chéron, S., 2013, Coupled molybdenum, iron and uranium stable isotopes as oceanic paleoredox proxies during the Paleoproterozoic Shunga Event: *Chemical Geology*, v. 362, p. 193-210.
- Berner, R. A., 1984, Sedimentary pyrite formation: an update: *Geochimica et Cosmochimica Acta*, v. 48, no. 4, p. 605-615.
- Brocks, J. J., Buick, R., Summons, R. E., and Logan, G. A., 2003, A reconstruction of Archean biological diversity based on molecular fossils from the 2.78 to 2.45 billion-year-old Mount Bruce Supergroup, Hamersley Basin, Western Australia: *Geochimica et Cosmochimica Acta*, v. 67, no. 22, p. 4321-4335.
- Canfield, D., 1998, A new model for Proterozoic ocean chemistry: *Nature*, v. 396, no. 6710, p. 450-453.
- Canfield, D. E., and Berner, R. A., 1987, Dissolution and pyritization of magnetite in anoxic marine sediments: *Geochimica et Cosmochimica Acta*, v. 51, no. 3, p. 645-659.
- Charilaou, M., Löffler, J., and Gehring, A., 2011, Fe–Ti–O exchange at high temperature and thermal hysteresis: *Geophysical Journal International*, v. 185, no. 2, p. 647-652.
- Cloud, P. E., 1968, Atmospheric and Hydrospheric Evolution on the Primitive Earth: *Science*, v. 160, no. 3829, p. 729-736.
- Craig, J. R., and Vokes, F. M., 1993, The metamorphism of pyrite and pyritic ores: an overview: *Mineralogical Magazine*, v. 57, no. 1, p. 3-18.
- Deiss, C., 1935, Cambrian-Algonkian unconformity in western Montana: *Geological Society of America Bulletin*, v. 46, no. 1, p. 95-124.
- Duke, E. F., and Lewis, R. S., 2010, Near infrared spectra of white mica in the Belt Supergroup and implications for metamorphism: *American Mineralogist*, v. 95, no. 7, p. 908-920.
- Embley, T. M., and Martin, W., 2006, Eukaryotic evolution, changes and challenges: *Nature*, v. 440, no. 7084, p. 623-630.
- Fleet, M. E., 2005, XANES spectroscopy of sulfur in earth materials: *The Canadian Mineralogist*, v. 43, no. 6, p. 1811-1838.

Fuller, M., Kidane, T., and Ali, J., 2002, AF demagnetization characteristics of NRM, compared with anhysteretic and saturation isothermal remanence: an aid in the interpretation of NRM: *Physics and Chemistry of the Earth*, v. 27, no. 25-31, p. 1169-1177.

Gellatly, A. M., and Lyons, T. W., 2005, Trace sulfate in mid-Proterozoic carbonates and the sulfur isotope record of biospheric evolution: *Geochimica et Cosmochimica Acta*, v. 69, no. 15, p. 3813-3829.

Graham, G., Hitzman, M. W., and Zieg, J., 2012, Geologic Setting, Sedimentary Architecture, and Paragenesis of the Mesoproterozoic Sediment-Hosted Sheep Creek Cu-Co-Ag Deposit, Helena Embayment, Montana: *Economic Geology*, v. 107, no. 6, p. 1115-1141.

Hall, A. J., 1986, Pyrite-pyrrhotine redox reactions in nature: *Mineralogical Magazine*, v. 50, p. 223-229.

Harrison, J. E., 1972, Precambrian Belt basin of northwestern United States: Its geometry, sedimentation, and copper occurrences: *Geological Society of America Bulletin*, v. 83, no. 5, p. 1215-1240.

Heslop, D., Dekkers, M., Kruiver, P., and Van Oorschot, I., 2002, Analysis of isothermal remanent magnetization acquisition curves using the expectation-maximization algorithm: *Geophysical Journal International*, v. 148, no. 1, p. 58-64.

Holland, H. D., 1984, *The chemical evolution of the atmosphere and oceans*, Princeton University Press.

-, 2006, The oxygenation of the atmosphere and oceans: *Philosophical Transactions of the Royal Society B: Biological Sciences*, v. 361, no. 1470, p. 903-915.

Horodyski, R. J., Winston, D., and Whipple, J. W., 1989, Paleontology of the middle Proterozoic belt supergroup, *in* Winston, D., Horodyski, R. J., and Whipple, J. W., eds., *Middle Proterozoic Belt Supergroup, Western Montana: Great Falls, Montana to Spokane*, Washington: 28th International Geological Congress, Field Trip Guidebook T334, p. 7-26.

Kirschvink, J. L., Kopp, R. E., Raub, T. D., Baumgartner, C. T., and Holt, J. W., 2008, Rapid, precise, and high-sensitivity acquisition of paleomagnetic and rock-magnetic data: Development of a low-noise automatic sample changing system for superconducting rock magnetometers: *Geochemistry Geophysics Geosystems*, v. 9, no. 5.

Knoll, A. H., Javaux, E. J., Hewitt, D., and Cohen, P., 2006, Eukaryotic organisms in Proterozoic oceans: *Philosophical Transactions of the Royal Society B: Biological Sciences*, v. 361, no. 1470, p. 1023-1038.

Kozłowski, A., Kakol, Z., Kim, D., Zalecki, R., and Honig, J., 1996, Heat capacity of  $\text{Fe}_{3-\alpha}\text{M}_{\alpha}\text{O}_4$  ( $\text{M} = \text{Zn, Ti}$ ,  $0 \leq \alpha \leq 0.04$ ): *Physical Review B*, v. 54, no. 17, p. 12093.

Li, H. Y., and Zhang, S. H., 2005, Detection of Mineralogical Changes in Pyrite Using Measurements of Temperature-Dependence Susceptibilities: *Chinese Journal of Geophysics*, v. 48, no. 6, p. 1454-1461.

Lowrie, W., and Fuller, M., 1971, Alternating field demagnetization characteristics of multidomain thermoremanent magnetization in magnetite: *Journal of Geophysical Research*, v. 76, no. 26, p. 6339-&.

Luepke, J. J., 1999, Geochemical trends in shales of the Belt Supergroup, Northwestern US: a marine model for the evolution of the Mesoproterozoic western Laurentian Margin [M.S. thesis: University Missouri-Columbia, 133 p.

Luepke, J. J., and Lyons, T. W., 2001, Pre-Rodinian (Mesoproterozoic) supercontinental rifting along the western margin of Laurentia: geochemical evidence from the Belt-Purcell Supergroup: *Precambrian Research*, v. 111, no. 1, p. 79-90.

Lyons, T. W., Luepke, J. J., Schreiber, M. E., and Zieg, G. A., 2000, Sulfur geochemical constraints on Mesoproterozoic restricted marine deposition: lower Belt Supergroup, northwestern United States: *Geochimica et Cosmochimica Acta*, v. 64, no. 3, p. 427-437.

McGoldrick, P., and Zieg, J., Massive microbes from the Mesoproterozoic of Montana, *in* Proceedings 17th Australia Geological Geological Convention Hobart, Australia, 2004, Volume 73, p. 100.

Minyuk, P., Tyukova, E., Subbotnikova, T., Kazansky, A. Y., and Fedotov, A., 2013, Thermal magnetic susceptibility data on natural iron sulfides of northeastern Russia: *Russian Geology and Geophysics*, v. 54, no. 4, p. 464-474.

Moreau, M., Ader, M., and Enkin, R., 2005, The magnetization of clay-rich rocks in sedimentary basins: low-temperature experimental formation of magnetic carriers in natural samples: *Earth and Planetary Science Letters*, v. 230, no. 1, p. 193-210.

Moskowitz, B. M., Jackson, M., and Kissel, C., 1998, Low-temperature magnetic behavior of titanomagnetites: *Earth and Planetary Science Letters*, v. 157, no. 3, p. 141-149.

Mosselmans, J., Patrick, R., Van der Laan, G., Charnock, J., Vaughan, D., Henderson, C., and Garner, C., 1995, X-ray absorption near-edge spectra of transition metal disulfides FeS<sub>2</sub> (pyrite and marcasite), CoS<sub>2</sub>, NiS<sub>2</sub> and CuS<sub>2</sub>, and their isomorphs FeAsS and CoAsS: *Physics and Chemistry of Minerals*, v. 22, no. 5, p. 311-317.

Mudge, M. R., Erickson, R. L., Kleinkopf, M. D., and Zartman, R. E., 1968, Reconnaissance geology, geophysics, and geochemistry of the southeastern part of the Lewis and Clark Range, Montana.

Nelson, W. H., 1963, Geology of the Duck Creek Pass quadrangle, Montana, U.S. Geological Survey Bulletin, Volume 1121-J, p. 56.

Peters, C., and Dekkers, M., 2003, Selected room temperature magnetic parameters as a function of mineralogy, concentration and grain size: *Physics and Chemistry of the Earth, Parts A/B/C*, v. 28, no. 16, p. 659-667.

Planavsky, N. J., McGoldrick, P., Scott, C. T., Li, C., Reinhard, C. T., Kelly, A. E., Chu, X., Bekker, A., Love, G. D., and Lyons, T. W., 2011, Widespread iron-rich conditions in the mid-Proterozoic ocean: *Nature*, v. 477, no. 7365, p. 448-451.

Potter, D., and Stephenson, A., 1986, The detection of fine particles of magnetite using anhysteretic and rotational remanent magnetizations: *Geophysical Journal International*, v. 87, no. 2, p. 569-582.

Poulton, S. W., and Canfield, D. E., 2005, Development of a sequential extraction procedure for iron: implications for iron partitioning in continentally derived particulates: *Chemical Geology*, v. 214, no. 3, p. 209-221.

-, 2011, Ferruginous conditions: a dominant feature of the ocean through Earth's history: *Elements*, v. 7, no. 2, p. 107-112.

Present, T. M., Bergmann, K. D., Meyers, C. E., Slotznick, S. P., Creveling, J. R., Zieg, G. A., Fischer, W. W., Knoll, A. H., and Grotzinger, J. P., in review, Pyrite-walled tube structures in a Mesoproterozoic SEDEX massive sulfide deposit: *Geological Society of America Bulletin*.

Raub, T., Johnson, S. C., and Raub, T. D., 2012, Rock magnetic detection of the pyrite-to-pyrrhotite reduction: applications to

hydrocarbon maturity, mineral resources, and biogeochemistry, American Geophysical Union, Fall Meeting: San Francisco, CA, p. GP34A-08.

Raymond, J., and Blankenship, R. E., 2004, Biosynthetic pathways, gene replacement and the antiquity of life: *Geobiology*, v. 2, no. 4, p. 199-203.

Reynolds, R. L., Rosenbaum, J. G., Sweetkind, D. S., Lanphere, M. A., Roberts, A. P., and Verosub, K. L., 2000, Recognition of primary and diagenetic magnetizations to determine the magnetic polarity record and timing of deposition of the moat-fill rocks of the Oligocene Creede Caldera, Colorado: *Geological Society of America Special Papers*, v. 346, p. 77-93.

Robertson, D., and France, D., 1994, Discrimination of remanence-carrying minerals in mixtures, using isothermal remanent magnetisation acquisition curves: *Physics of the Earth and Planetary Interiors*, v. 82, no. 3, p. 223-234.

Ross, G. M., and Villeneuve, M., 2003, Provenance of the Mesoproterozoic (1.45 Ga) Belt basin (western North America): Another piece in the pre-Rodinia paleogeographic puzzle: *Geological Society of America Bulletin*, v. 115, no. 10, p. 1191-1217.

Schieber, J., 1989a, Facies and origin of shales from the mid-Proterozoic Newland Formation, Belt Basin, Montana, USA: *Sedimentology*, v. 36, no. 2, p. 203-219.

Schieber, J., 1989b, The origin of the Neihart Quartzite, a basal deposit of the Mid-Proterozoic Belt Supergroup, Montana, USA: *Geological Magazine*, v. 126, no. 03, p. 271-281.

Schieber, J., 1989c, Pyrite mineralization in microbial mats from the mid-Proterozoic Newland Formation, Belt Supergroup, Montana, USA: *Sedimentary geology*, v. 64, no. 1, p. 79-90.

Schumann, R., Stewart, W., Miller, S., Kawashima, N., Li, J., and Smart, R., 2012, Acid-base accounting assessment of mine wastes using the chromium reducible sulfur method: *Science of the Total Environment*, v. 424, p. 289-296.

Slotznick, S. P., Winston, D., Webb, S. M., Kirschvink, J. L., and Fischer, W. W., 2016, Iron mineralogy and redox conditions during deposition of the Mid-Proterozoic Appikunni Formation, Belt Supergroup, Glacier National Park: *Geological Society of America Special Papers*, v. 522.

Snowball, I. F., 1997, The detection of single-domain greigite (Fe<sub>3</sub>S<sub>4</sub>) using rotational remanent magnetization (RRM) and the effective gyro field (Bg):



mineral magnetic and palaeomagnetic applications: *Geophysical Journal International*, v. 130, no. 3, p. 704-716.

Strauss, H., and Schieber, J., 1990, A sulfur isotope study of pyrite genesis: the Mid-Proterozoic Newland Formation, Belt Supergroup, Montana: *Geochimica et Cosmochimica Acta*, v. 54, no. 1, p. 197-204.

Stüeken, E. E., 2013, A test of the nitrogen-limitation hypothesis for retarded eukaryote radiation: nitrogen isotopes across a Mesoproterozoic basinal profile: *Geochimica et Cosmochimica Acta*, v. 120, p. 121-139.

Suzuki, Y., Kopp, R. E., Kogure, T., Suga, A., Takai, K., Tsuchida, S., Ozaki, N., Endo, K., Hashimoto, J., and Kato, Y., 2006, Sclerite formation in the hydrothermal-vent “scaly-foot” gastropod—possible control of iron sulfide biomineralization by the animal: *Earth and Planetary Science Letters*, v. 242, no. 1, p. 39-50.

Thomson, G. F., 1990, The anomalous demagnetization of pyrrhotite: *Geophysical Journal International*, v. 103, no. 2, p. 425-430.

Walcott, C. D., 1899, Pre-Cambrian fossiliferous formations: *Geological Society of America Bulletin*, v. 10, no. 1, p. 199-244.

Walter, M., Oehler, J. H., and Oehler, D. Z., 1976, Megascopic algae 1300 million years old from the Belt Supergroup, Montana: a reinterpretation of Walcott's *Helminthoidichnites*: *Journal of Paleontology*, p. 872-881.

White, J., Gammons, C. H., and Zieg, G., 2014, Paragenesis of cobalt and nickel in the Black Butte shale-hosted copper deposit, Belt Basin, Montana, USA: *Mineralium Deposita*, v. 49, no. 3, p. 335-351.

Wilkin, R., Barnes, H., and Brantley, S., 1996, The size distribution of framboidal pyrite in modern sediments: an indicator of redox conditions: *Geochimica et Cosmochimica Acta*, v. 60, no. 20, p. 3897-3912.

Winston, D., and Link, P., 1993, Middle Proterozoic rocks of Montana, Idaho and eastern Washington: the Belt Supergroup: *Precambrian: Conterminous US: The Geology of North America*, v. 2, p. 487-517.

Xu, S., and Dunlop, D. J., 1995, Toward a better understanding of the Lowrie-Fuller test: *Journal of Geophysical Research: Solid Earth* (1978–2012), v. 100, no. B11, p. 22533-22542.

Zieg, G., and Leitch, C., The geology of the Sheep Creek copper deposit, Meagher County, Montana, *in* Proceedings Belt Symposium III Abstracts, 1993: Montana Bureau of Mines and Geology 1999, Volume 381.

Zieg, G., Scartozzi, V., Chutas, N., Albers, D., Gostomski, K., and Jones, J., 2013, Black Butte copper deposits, lower Belt Supergroup, Montana: Northwest Geology, v. 42, p. 131-147.

Zieg, G. A., 1986, Stratigraphy and sedimentology of the Middle Proterozoic Newland Limestone: Montana Bureau of Mines and Geology Special Publication, v. 94, p. 125-141.

## Chapter 4

# Iron Mineralogy and Redox Conditions During Deposition of the Mid-Proterozoic Appekunny Formation, Belt Supergroup, Glacier National Park

*Originally published in:*

*Slotznick, S. P., Winston, D., Webb, S. M., Kirschvink, J. L., and Fischer, W. W., 2016, Iron mineralogy and redox conditions during deposition of the Mid-Proterozoic Appekunny Formation, Belt Supergroup, Glacier National Park: Geological Society of America Special Papers, v. 522, doi: 10.1130/2016.2522(09).*

## 4.1 Abstract

The redox state of the mid-Proterozoic oceans, lakes, and atmospheres is still debated, but it is vital for understanding the emergence and rise of macroscopic organisms and eukaryotes. The Appekunny Formation, Belt Supergroup, Montana contains some of these early macrofossils dated between 1.47 Ga and 1.40 Ga and provides a well-preserved record of paleoenvironmental conditions. We analyzed the iron chemistry and mineralogy in samples from Glacier National Park, Montana by pairing the bulk rock magnetic techniques with textural techniques including light microscopy, scanning electron microscopy, and synchrotron-based X-ray absorption spectroscopy. Field observations of the Appekunny Formation combined with mineralogical information allowed revised correlations of stratigraphic members across the park. However, late diagenetic and/or metasomatic fluids affected primary iron phases as evidenced by prevalent postdepositional phases including base-metal sulfides. On the west side of the park, pyrrhotite and chlorite rims formed during burial metamorphism in at least two recrystallization events. These complex postdepositional transformations could affect bulk proxies for paleoredox. By pairing bulk and textural techniques, we show primary records of redox chemistry were preserved in early diagenetic and often recrystallized framboidal pyrite, submicron magnetite grains interpreted to be detrital in origin, and red-bed laminae interpreted to record primary detrital oxides. Based on these observations, we hypothesize that the shallow waters of the mid-Proterozoic Belt Basin were similar to those in modern marine and lacustrine waters: fully oxygenated, with detrital reactive iron fluxes that mineralized pyrite during organic diagenesis in suboxic, anoxic, and sulfidic conditions in sedimentary pore waters.

## 4.2 Introduction

Currently exposed across parts of Montana, Idaho, Washington, Alberta, and British Columbia, the Belt Supergroup is one of the best-preserved and

extensive mid-Proterozoic sedimentary terranes (Fig. 4.1A). This thick sedimentary succession was deposited between 1470 Ma and 1401 Ma (Anderson and Davis, 1995; Evans et al., 2000; Sears et al., 1998), and provides an important paleontological perspective on the evolution of eukaryotes and multicellularity (Knoll et al., 2006). The Belt Supergroup is well-known for its stromatolites, but it also contains a diversity of other micro- and macrofossils (Horodyski et al., 1989). In the mudstones of its lower portion, two macrofossils have been studied in great detail. First identified by Charles Doolittle Walcott (1899) in the Greyson Shale and later renamed (Walter et al., 1976), *Grypania spiralis* is a curved or coiled ribbon, 0.2 to 1.7 mm wide, and 6 to 14mm in coiled diameter, and has been nonuniquely interpreted as eukaryotic algae as well as a consortia of several microscopic organisms (Horodyski et al., 1989; Knoll et al., 2006; Walter et al., 1976). Within the stratigraphically correlated Appekunny Formation, *Horodyskia moniliformis* has the general appearance of a string of beads with diameters of 2.1-9.2 mm and lengths up to 15 cm, and has been interpreted to represent a wide range of different organisms including algae (Grey and Williams, 1990; Horodyski, 1993), prokaryotic colony (Knoll et al., 2006), tissue-grade colonial eukaryote (Fedonkin and Yochelson, 2002), sponge (Hofmann, 2001), foraminifer (Dong et al., 2008), and lichen (Retallack et al., 2013). No matter their affinity, understanding more about the environmental conditions where these early macroscopic organisms lived will tell us more about the pacing of evolution and how it might have been aided, frustrated, or unaffected by changing environmental conditions.

Major first order questions exist concerning the redox status of the oceans, lakes, and atmosphere during mid-Proterozoic time. Based broadly on a gap in the preserved record of banded iron formation, red beds, marine manganese deposits, and the conspicuous presence of carbonate platforms, it has been suggested that the mid-Proterozoic subaqueous basins were oxygenated at (nearly) all depths (Cloud, 1968; Holland, 1984, 2006; Slack et al., 2007). Based on theory and sulfur isotope records, others have suggested that if atmospheric

oxygen values were lower than today with similar levels of marine primary production, then the deep oceans would have been anoxic and sulfidic (i.e. euxinic), with the consequence that the lack of banded iron formations was due to an increase in water column sulfide leading to iron sulfide precipitation (Canfield, 1998). Recently, bulk geochemical techniques have queried the composition and redox state of mid-Proterozoic basins using the sequential extraction technique known as iron speciation as well as trace metal work (e.g. Gilleaudeau and Kah, 2015; Kendall et al., 2009; Planavsky et al., 2011; Shen et al., 2003; Sperling et al., 2014). Iron speciation data suggest anoxic, euxinic, and oxic waters varying between different basins, different water depths, and temporally with dominant anoxic and sulfur poor (i.e. ferruginous) conditions despite the lack of iron formation deposition (Poulton and Canfield, 2011; Sperling et al., 2015). This new notion of a ferruginous Proterozoic world based on iron speciation is distinctly different from the aforementioned canonical views of mid-Proterozoic paleoenvironments.

Several geochemical studies have focused specifically on the paleoredox state and geochemistry of the Belt Basin during deposition of the Belt Supergroup. Arguments for a stratified euxinic basin during deposition of the lower Belt Supergroup were made on the basis of sulfate levels and sulfur isotopes (Gellatly and Lyons, 2005; Luepke and Lyons, 2001; Lyons et al., 2000) as well as presence of basinwide sedimentary laminations similar to those found in the Black Sea (Huebschman, 1973; Lyons et al., 2000). Bottom water suboxic to euxinic conditions were also inferred from the high (several weight percent) organic content observed in shales regionally (Lyons et al., 2000) and the conspicuous syndepositional to early diagenetic sulfide and base metal deposits of Pb, Cu and Zn (Graham et al., 2012; Hamilton et al., 1982; Huebschman, 1973; Slotznick et al., 2015). However, iron speciation results on the same samples suggested instead anoxic and ferruginous conditions for the water column during deposition of the lower Belt Supergroup (Planavsky et al., 2011). Additionally, recent nitrogen isotope studies suggested oxygenated surface waters (Stüeken,

2013). Importantly, most of these studies focused on samples from the Helena Embayment, which is distinct from, but stratigraphically correlated to, the units in Glacier National Park and the rest of the Belt Basin.

The Belt Supergroup exposures in Glacier National Park provide a well-studied region of low metamorphic grade in which to investigate iron mineralogy, and provide a different window into the redox status of the larger Belt Basin than previously-studied samples from the Helena Embayment (Lyons et al., 2000; Planavsky et al., 2011; Stüeken, 2013). Based on sedimentological indicators, the strata in the park were predominantly deposited within storm wave base, even including intervals of subaerial exposure, from a much more proximal part of the basin (Winston and Link, 1993). For many of these shallower environments, the local water column should reflect a higher degree of influence by oxygen in the atmosphere, with the null expectation that local anoxic and/or H<sub>2</sub>S-rich conditions would be tied to sedimentary pore fluids. However, the sedimentary units at Glacier National Park are well-known for their brilliant green and red coloration, due to the variable and differential presence of reduced and oxidized iron-bearing minerals (Winston, 1986c). These differences have been hypothesized to reflect changing redox conditions even in these shallow waters (Stanley and Davies-Vollum, 2000) while others suggest they are diagenetic but broadly reflect syndepositional environments (Winston, 1986b; Winston, 2016). We focused our study of iron mineralogy, deposition, and preservation on the primarily green and gray-colored Appekunny Formation as well as the stratigraphic units above and below it using a unique and powerful combination of techniques to assess iron mineralization including rock magnetics, light and electron microscopy, and synchrotron X-ray spectroscopy. Characterization of the iron mineralization of the Appekunny, Prichard, and Grinnell Formations provides support for new stratigraphic correlations of the Appekunny Formation across Glacier National Park and suggests that the shallow waters of the Belt Basin were similar to today with an oxic water column overlying suboxic to anoxic to H<sub>2</sub>S-rich pore waters.

### 4.3 Geologic Setting

The Belt Supergroup is composed of mixed siliciclastic and carbonate rocks in units that thicken from Glacier National Park to the west, reaching a maximum of 15-20 km (Winston and Link, 1993). Several tectonostratigraphic models for the origin and development of the Belt Basin have been proposed including a large lake in an intercontinental rift (Winston, 1986b), a marine setting along the rifted margin of North America (Price, 1964), a lake or restricted marine setting from a remnant ocean basin (Hoffman, 1988), or a restricted marine/isolated lake setting due to supercontinental rifting (Luepke and Lyons, 2001; Lyons et al., 2000). Part of this debate is due to the preservation of shallow water and potentially fluvial sediments on the eastern edge of the basin, whereas a western margin was rifted away during the breakup of Rodinia (Stewart, 1972). Sediment provenance studies suggest a predominantly western source for the lower two-thirds of the Belt, with a predominately Laurentian source observed in Glacier National Park and the Helena Embayment (González-Álvarez et al., 2006; Ross and Villeneuve, 2003).

The Belt Supergroup has been divided into 4 main stratigraphic groups: the lower Belt, the Ravalli Group, the Piegan Group, and the Missoula Group (Whipple et al., 1984; Winston, 1986a; Winston, 2007) (Fig. 4.1B). The lower Belt is primarily dark colored mudstones and siltstones with iron sulfides, interpreted as deep basinal turbidites (Cressman, 1989). The Ravalli Group contains red and green mudstones and siltstones and light-colored sandstones deposited in shallower environments; some units and members display evidence of episodic subaerial exposure/playa environments (Winston, 2016; Winston and Link, 1993). The Piegan Group is composed of cyclic and/or graded dolomite, mudstone, and sandstone beds with common stromatolites, ooids, and molar tooth structures; it is interpreted to preserve the subtidal midshelf (Pratt, 2001) or underfilled lake deposits with less detrital input (Winston, 2007). The Missoula Group contains red to green mudstones, and pink quartz sandstones with thin intervals of carbonate and dark gray mudstones interpreted to be alluvial, playa,



and shallow subaqueous sequences (Winston and Link, 1993). Despite this well-recognized coarse stratigraphic architecture, more detailed stratigraphic correlations between different parts of the Belt Basin have been challenging in part due to facies changes and local stratigraphic nomenclature. Notably, some have grouped the Appekunny Formation, composed of green and gray mudstones and siltstones, in the Ravalli Group with the overlying Grinnell Formation, composed of red and green mudstones and sandstones (e.g. Whipple et al., 1997; Whipple et al., 1984; Fig. 4.1B). Others, due to its dramatic thinning and absence toward the west, have considered this unit to pass westward into the Prichard Formation making it part of the lower Belt (Winston and Link, 1993) and/or it has been correlated with the Greyson Formation of the Helena Embayment (Harrison, 1972; Winston, 1986a) which is similarly nebulously assigned, sometimes with the lower Belt (Graham et al., 2012; Ross and Villeneuve, 2003; Winston and Link, 1993) and other times with the Ravalli Group (Harrison, 1972; Mudge et al., 1968). Observations of the stratigraphy and iron-mineralogy and geochemistry may help shed light onto these possible correlation schemes by providing additional data on the key transition from the east side of Glacier National Park to its western side.

The Belt Supergroup is variably well-preserved across its present extent with known metamorphic gradients. In general, the degree of metamorphism increases to the west, with the best-preserved, lowest temperature exposures in Glacier National Park and the Helena Embayment (Duke and Lewis, 2010). Within Glacier National Park, several studies have quantified the amount of metamorphism and postdepositional alteration of these rocks. Maxwell and Hower (1967) examined the structural changes of white mica (illite) from 1M<sub>d</sub> or 1M polymorphs in low-grade samples to 2M polymorphs in more deeply buried samples with the transition complete by the biotite isograd (Frey, 1987). Samples from the Appekunny Formation, Grinnell Formation, and Missoula Group in Glacier National Park were between 41% and 62% 2M polytype, suggesting sub-biotite zone metamorphism. Eslinger and Savin (1973) found a similar range

from 21 to 61% 2M polytype in samples from the Appekunny Formation, Grinnell Formation, and Helena Formation primarily from the east side of the park, which also increased with burial depth as interpreted from stratigraphic level. Oxygen isotope geothermometry of quartz and white micas indicated metamorphic temperatures between 225°C and 310°C, suggesting sub-biotite zone to near-biotite zone (Eslinger and Savin, 1973). A new high throughput technique using near-infrared spectroscopy to observe shifts in the Al-OH absorption band in white micas, which were correlated basinwide using other metamorphic studies (including those cited already), observed the Belt rocks of Glacier National Park to be some of the best preserved in the sub-biotite zone (Duke and Lewis, 2010).

Although the strata in Glacier National Park have not been as strongly heated and metamorphosed as those to the west in the Belt Basin, several observations of the mineralogy and petrography of the rocks within Glacier National Park have documented the effects of mineralization due to later diagenetic and/or metasomatic fluids. These observations include euhedral authigenic monazites in the Appekunny Formation and Grinnell Formation with dates ranging from 300 Ma to 1400 Ma, interpreted to reflect the protracted flow of basinal brines through these units (González-Álvarez et al., 2006). Peaks in age spectra at 1400 Ma, 1000-900 Ma, 600 Ma, and 300 Ma suggest an episodic nature to the metasomatism, which could be linked to continental-scale tectonic processes (González-Álvarez and Kerrich, 2010). Rare-earth element abundances throughout the stratigraphic units in Glacier National Park highlight a mixture of near-primary compositions with two distinct alteration patterns that are more pronounced in sandstones, perhaps due to their greater permeability; the enrichment and depletion patterns suggest at least some of the alteration fluids were oxidizing and alkaline (González-Álvarez and Kerrich, 2010).

Previous studies have not directly examined the impact of these metasomatic fluids on the iron mineralogy in samples from Glacier National Park. However, some paleomagnetic measurements of the Grinnell Formation in

Glacier National Park were noted to have overprints from phases of intermediate coercivity between 50 and 100 mT or Curie temperature between 210°C and 610°C, which were distinct from a component that demagnetized at over 665°C (Vitorello and Van der Voo, 1977). The wide coercivity and temperature range given for the overprint component could be indicative of secondary hematite, maghemite, titanomagnetite, magnetite, pyrrhotite, or greigite, whereas the high temperature component is uniquely hematite (Dunlop and Özdemir, 1997; Peters and Dekkers, 2003). The high temperature component weakly passed a fold test, has a vector direction similar to other localities from the same time period, and thus was interpreted as primary (Vitorello and Van der Voo, 1977). Other samples of the Grinnell Formation in the northwestern portion of the park were not affected by these overprints and matched other samples across the Belt Basin, which also pass the field test for antiparallel reversals (Elston et al., 2002).

#### **4.4 Sample Descriptions and Field Relationships**

Samples were collected in Glacier National Park focusing on stratigraphic sections of the Appekunny Formation and extending into the overlying Grinnell Formation and the underlying Prichard Formation. To minimize effects on iron mineralogy possibly due to temporal and paleoenvironmental variation and/or heterogeneous distribution of altering fluid flow, samples were collected carefully from locations covering the entire Appekunny Formation on outcrops occurring on both the west and east limbs of the Akamina syncline, a broad SE-NW trending structure running through Glacier National Park (Fig. 4.1A; Dahlstrom, 1970; Whipple et al., 1992).

The Appekunny Formation (Ross, 1959; Willis, 1902) has been divided into five informal members (Whipple et al., 1984) based on stratigraphic measurements on Apekuni Mountain in the Many Glacier region (Fig. 4.2B; Whipple et al., 1997). We revisited this type locality and one of us (Slotznick) remeasured the stratigraphic section to describe these members in greater detail (Fig. 4.2A). Based on the Apekuni Mountain section, the descriptions of these

members by J.W. Whipple, and previous field excursions by one of us (Winston) with J.W. Whipple, we identified and sampled outcrops of all five members on the east side of the park exposed along the Going-to-the-Sun Road. These sampled outcrops show very similar lithofacies and stratigraphy to the Many Glacier section, although we did not measure a detailed stratigraphic section along the Going-to-the-Sun Road. Observations and interpretations of sedimentary structures in these members vary slightly from previous authors and are described next for completeness.

Member 1 of the Appekunny Formation and the underlying Altyn Formation show a conformable gradational interbedded contact (over 10 m) of siltstone and argillite beds with carbonate layers. Based on Whipple et al. (1997), the base of member 1 was defined as a 1-m-thick greenish white quartz sandstone bed, above which sandstone continued to be interbedded with green siltstone and argillite for several meters. Member 1 consists of mostly planar, sometimes gently undulating laminated maroon siltstone with millimeter-thick laminae interstratified with equally thick layers of red claystone. Ripple cross-stratification is present at the millimeter to decimeter wavelength scale (Fig. 4.3A) with uncommon broad centimeter-tall hummocky cross-stratification. A thick quartz arenite sandstone bed in the middle of member 1 has been used as a key marker bed across the park (Whipple et al., 1984), and it is 24 m thick in the Apekuni Mountain section. Rare rip-up mud chips are found; overall, the member is interpreted as reflecting subaqueous sediment transport and deposition. Although mainly maroon to red in color, some grayish green intervals are observed; while sometimes discontinuous pinching out as lenses, others are distinct stratigraphic units that span large distances along strike. Samples of each colored lithotype were sampled and analyzed with the maroon sample taken from lower in the succession than the green sample. Member 1 is 173 m thick at Apekuni Mountain. *Horodyskia moniliformis* was first found in the Appekunny Formation at Apekuni Mountain (Horodyski, 1982), and most fossils occur below the thick quartz sandstone marker bed in the middle of member 1 (Fedonkin and

Yochelson, 2002; Retallack et al., 2013). Additional fossil examples have been collected in member 1 along the Going-to-the-Sun Road and at Rising Wolf Mountain in the Two Medicine region (Fedonkin and Yochelson, 2002; Retallack et al., 2013). One *Horodyskia* specimen was collected at Otokomi Mountain north of the Going-to-the-Sun Road, but no stratigraphic information is available for it (Horodyski, 1982).

Member 2 and member 1 have a gradational interbedded contact with the top of member 1 set at the uppermost maroon beds (Whipple et al., 1992). Although very similar to member 1 in lithology, member 2 notably has an increased proportion of green siltstone to mudstone creating thicker beds up to a meter thick; these beds of well-sorted silt laminae often exhibit plumose fracturing. Planar to gently undulating to wavy lamination was observed on the centimeter to meter-scale with ripple cross stratification and broad decimeter-scale hummock cross-stratification. Along the Going-to-the-Sun Road, multiple meter-thick beds display soft-sediment deformation structures including loading and the ball-and-pillow structures noted in the middle of member 2 (Fig. 4.3B). A few quartz sandstone beds are observed throughout the section, but they are thinner than those in member 1. Overall, member 2 is 145 m thick at Apekuni Mountain.

Member 3 contains several 2-5-m-thick pinkish brown quartz arenite sandstone beds and lenses/load structures; the lowest of these beds marks its base (Whipple et al., 1992). These arenite intervals contain common large millimeter-sized pyrite grains and goethite pseudomorphs after pyrite. Interbedded within the arenite sandstone and between these sandstone beds, there is grayish green siltstone with small amounts of claystone in thinly planar to wavy laminae. Most strikingly, this member contains common large hummocky cross stratification up to a decimeter in height and up to meter-scale in wavelength, and in some locations, steep walled decimeter-scale gutters cut into the underlying beds (Figs. 4.3CD). Additionally, member 3 differs from member 2 with increased claystone, the presence of common fining upward cycles, and an orange-red weathering

appearance of some intervals. Ripples and mud cracks are found throughout the member, the latter especially common near quartz arenite sandstone layers. No implied mechanism of formation is interpreted for the mud cracks; they could be either subaqueous or subaerial. Scattered rusty weathering iron oxide phases were observed in road-cut outcrop exposures, whereas fresh-cut samples revealed iron sulfides suggesting the oxides are dominantly a recent near-surface weathering product. At Apekuni Mountain, member 3 is 72 m thick.

Member 4 is composed of green to dark greenish gray to dark to medium gray interbedded siltstone and claystone in millimeter to centimeter-thick lenticular and pinch and swell layers. These are more silty than the microcouplets noted throughout the Prichard Formation (Winston and Link, 1993). Finely laminated, member 4 is fissile, weathering in thin plates, and it is poorly exposed. The base of the member is defined by the first occurrence of this thinly laminated siltstone (Whipple et al., 1992). Notable characteristics include the abundance of red iron oxides on parting surfaces, presumably from the exposure and surface weathering of iron sulfides. Scour pits and convolute bedding from soft sediment deformation are also common and a defining characteristic (Fig. 4.3E). Hummocky-cross stratification is still present in this member, but it is less common and smaller in scale than member 3. Similarly, pinkish-brown quartz arenite sandstone beds are still found in this unit. Mudcracks and mudchip breccias are also found throughout this member, often associated with quartz sandstone but occasionally in green siltstone and claystone instead.

Member 5 is composed of fining-upward couplets (3 mm to 10 cm) and microlaminae (<3 mm) of planar laminated green siltstone and claystone. Abundant mud cracks and mud chip breccias (much more common than in member 4) highlight alternating subaerial desiccation and flooding of a shoreline muddy flat (Fig. 4.3F). The fine lamination of this unit results in weathering of the unit in thin plates, especially on Apekuni Mountain where recent freeze-thaw cycles have made this unit be poorly exposed. Member 5 and member 4 have a complex gradational contact with a few intervals of member 5-type beds found

over a 75 m interval. The base of the contact is unclear from previous work, so it is defined here as transition from a majority of member 4-type intervals of pinch-and-swell centimeter to millimeter thick laminations with scour pits, convolute bedding, and hummocky cross-stratification to even thinner beds with a predominance of microlaminae with mud cracks and mud chips characterizing member 5. This makes member 4 185 m thick at Apekuni Mountain with a thin member 5 measuring 48 m in thickness.

Appekunny member 5 grades conformably up into the overlying Grinnell Formation. The base of the Grinnell Formation is defined by the lowest occurrence of red to purplish red mud-cracked claystone and siltstone beds (Whipple et al., 1984), although interbedded green and red beds continue for several tens of meters above this contact. Although the proportion varies, the Grinnell Formation contains more white quartz arenite sandstone lenticular beds throughout than the Appekunny Formation, and it preserves a wide range of shallow-water sedimentary structures from ripple marks and cross stratification to mud cracks and mud chip/mud ball breccias.

Exposures of Appekunny member 5 continue on the west side of Glacier National Park (e.g. Fig. 4.2D). Here, it was interpreted to overlie the Prichard Formation with a thick transition zone containing wavy laminated and lenticular layers of calcareous claystone and siltstone as well as beds and lenses of quartz arenite, stromatolitic limestone (Whipple et al., 1997). Rare mud cracks are noted in a few intervals. The precise contact between the Appekunny Formation and Prichard Formation was not exposed within the park from previous stratigraphic descriptions, and it was postulated Appekunny member 3 and 4 could even have extended to the west side of the park (Whipple et al., 1997; Whipple et al., 1992). However, in the neighboring Whitefish and Flathead Range, the contact was suggested to be gradational, although there were questions about the identification of the Appekunny Formation in this locality (Harrison et al., 1998; Whipple et al., 1984).

A previously unpublished stratigraphic section was measured by coauthor Winston on the east side of Mount Brown and it is shown here in Figure 4.2C. This locality is 3 km from a published section measured by J.W. Whipple at Beaver Medicine Falls, Edwards Mountain (Fig. 4.2D; Whipple et al., 1997), and it was measured in an effort to improve stratigraphic correlations within the park. Based on the new descriptions and definitions of the members of the Appekunny Formation from the type-section and revisiting the east side of Mount Brown, we present here new stratigraphic interpretations for these units.

At the base of the section, there is an 89 m thick package of medium gray siltstone to dark gray claystone microlaminae, subcentimeter-scale pinch-and-swell couplets, and even couplets (Fig. 4.3G). Soft sediment deformation including convolute bedding is found throughout, sometimes producing clasts of the laminated mudstone. Mud cracks were observed near the top of this unit at 52 m and 76 m. Although entire laminae filled with abundant iron sulfides were not observed in the field, collected hand samples include very large (5 mm) iron sulfide phases in various states of *in situ* oxidative weathering. We interpret this unit as member 4 due to its pinch-and-swell couplets, convolute bedding, and abundant iron oxides.

The transition to the next unit is gradational. The first 188 m of the unit are mainly composed of green, even microlaminae and microcouplets of siltstone to claystone, with common mud cracks and mud chip breccias. This unit's massive weathering is a striking feature, and it additionally contains several 10-60 cm thick tabular siltstone beds. Several additional unique beds stand out from the siltstones and claystones in this unit. One calcareous bed weathers recessively and contains mud chips, mud cracks, and soft sediment deformation features. In the upper portions, two 3 cm thick medium-grained, well-rounded quartz sand beds with high-angle cross bedding were observed.

A change in facies up section occurs with 58 m of dark gray interbedded siltstone and claystone and even to pinch and swell couplets and microlaminae layers as well as some hummocky cross stratification in siltstones. Several 60 cm



thick medium-grained sandstone beds with cross stratification occur throughout the unit. This interval contains an increasing amount of carbonate with several lenses of carbonate-rich mud chips and molar tooth hash. A 10 cm thick stromatolitic limestone bed occurs at 295 m. Mud cracks with associated mud chips are rare except in intervals near the sandstone beds. After the 58 m of wavy and pinch-and-swell layers, there is a return to green tabular siltstone beds, microlaminae, and lenticular to even siltstone to claystone couplets for another 75 m. Some intervals contain mud cracks and mud chips—textures that become more abundant near the top of the unit.

Here we interpret the entire 321 m as Appekunny member 5 with a small interval similar to Appekunny member 4 in this long complex transition. The upper portion of this has previously been identified as member 5 (Whipple et al., 1997), but due to the characteristics of the lower portion with even couplets and microlaminae and abundant mud chip breccias, we think the lower portion should be grouped with member 5 even though it is below a small interbedded interval of pinch-and-swell beds. The new description of the type-section at Apekuni Mountain highlights the complex long-gradational transition between these two members, so interbedded intervals of member 4-type facies within member 5 are not unexpected.

The top of this unit is marked by the first appearance of purple coloration in the even couplets of siltstone and claystone, with mud cracks and chips. This purple coloration appears interbedded with green-colored beds and lenses as well as frequent thin quartz sand beds for at least 148 m. This is the contact of Appekunny Formation member 5 with the overlying Grinnell Formation.

The new Mount Brown stratigraphic column and facies detailed earlier highlight the abundance of mud cracks and mud chip breccias in the lower portion of the stratigraphy previously called the Prichard transition zone, as well as a lack of stratigraphically continuous laminae of abundant iron sulfides like those common in the Prichard Formation. Therefore, we argue that these strata do not represent classic Prichard Formation or Prichard transition zone, and we instead

assign them to Appekunny members 4 and 5. While still in line with the interpretations by previous authors (Whipple et al., 1997) as a transitional facies, this interpretation extends Appekunny member 4 to the west side of the park and highlights a thickening of facies to the west consistent with the larger architecture of the Belt Basin. Although facies typical of the Prichard Formation—even couplets of gray siltstone and claystone with continuous layers of iron sulfides—were observed in outcrops on the west side of Mount Brown and along McDonald Creek, we found no clear evidence that these units are preserved on the east side of Mount Brown (Fig. 4.3H). Due to through-going structures and limited continuous exposure, it is difficult to determine the relative position of these samples within the stratigraphic columns to the east. The iron mineralogy and geochemistry of these units, however, may help to evaluate these possible correlations.

#### **4.5 Sampling and Analytical Methods**

Oriented block samples were collected by hiking off-trail from the Going-to-the-Sun Road, Glacier National Park in October 2012 and August 2014 (Fig. 4.1A). Metadata including lithology, sedimentology, photographs, and global-positioning system (GPS) locations were also recorded for all samples. Samples covered all five members of the Appekunny Formation, the Grinnell Formation, and potentially the Prichard Formation (Table S4.1). Samples were cored using a nonmagnetic 25.4 mm diamond-edged drill bit, and sliced into 2-5-mm-thick specimen rounds using a saw with a nonmagnetic brass blade. Nondestructive rock magnetic experiments were performed on specimens using a 2G Enterprises SQUID magnetometer following the RAPID protocols, and the data were analyzed using the RAPID Matlab (The Mathworks, Inc.) scripts (Kirschvink et al., 2008). Our protocol included measurements of alternating field (AF) demagnetization of the natural remanent magnetization (NRM), rotational remanent magnetization (RRM) acquisition and demagnetization, anhysteretic remanent magnetization (ARM) acquisition and demagnetization, isothermal remanent magnetization

(IRM) acquisition and demagnetization, and backfield IRM acquisition. These analyses can be used to observe fundamental physical properties that can be used to distinguish different ferromagnetic minerals (e.g. Peters and Dekkers, 2003). The destructive rock magnetic technique of KappaBridge thermal susceptibility was measured on neighboring specimens for a subset of the samples using an AGICO MFK1-FA KappaBridge, with the resulting data reduced using Cureval and Matlab scripts.

The same specimens that were run through nondestructive rock magnetic experiments were then made into polished thick or thin sections to provide a flat surface for optical, magnetic, and chemical imaging. Ultrahigh-resolution scanning SQUID Microscopy (UHRSSM) was then performed on 11 of the sections with 100  $\mu\text{m}$  pixels to locate ferromagnetic grains as regions for further analysis. Transmitted and reflected light microscopy was used to observe petrographic textures in all samples as well as identify additional target regions. Further petrographic observations were made using the Zeiss 1550VP field emission scanning electron microscope in the Caltech GPS Division Analytical Facility; this has a Robinson-type backscatter electron detector for imaging and a working distance of 8-9 mm. This instrument contains a paired Oxford X-Max SDD X-ray energy dispersive spectrometer (EDS) system used to determine X-ray spectra of elemental abundance at submicron sized spots on 12 thin or thick specimens. This chemical information was important for confirming detections of chalcopyrite, galena, and sphalerite in addition to iron sulfides in present in many samples.

Synchrotron-based high-energy X-ray fluorescence (XRF) imaging was performed using beam line 10-2 at the Stanford Synchrotron Radiation Lightsource to characterize elemental abundances including trace metals in 21 thick or thin sections. Applied incident X-ray energies ranged from 20,200 eV to 10,000 eV, and standards for elements of interest were run at each beam time session with the same collection parameters. Synchrotron-based X-ray absorption near-edge spectroscopy (XANES/XAS) was paired with elemental imaging using

beam line 14-3 and 2-3 at the Stanford Synchrotron Radiation Lightsource. X-ray absorbance spectroscopy (XAS) was performed in fluorescence mode at specific 2-4- $\mu\text{m}$ -sized spots on 13 thin or thick sections to determine the chemical form of elements (oxidation state, orbital electronics, type and number of neighbors) while preserving textural information. Differences in the shape and K-edge of these absorption spectra allow us to easily distinguish between a wide range of Fe- and S- bearing minerals (Fleet, 2005; O'Day et al., 2004). Chalcopyrite and pyrrhotite have sufficiently similar S K-edge spectra that high-energy XRF, electron microscopy, and EDS were applied to confirm the presence of these minerals. The incident X-ray energy was set to energies around the sulfur absorption edge (2472 eV) and the iron absorption edge (7112 eV) using a Si (111) double crystal monochromator. At beam line 14-3, the monochromator energy was calibrated by setting the first thiol peak of a sodium thiosulfate powder to 2472.02 eV. At beam line 2-3, the monochromator energy was calibrated by setting the inflection point of a metallic Fe foil to 7112 eV. XRF elemental maps were processed using the MicroAnalysis Toolkit (Webb, 2011) and XAS data were processed using SIXPACK (Webb, 2005).

#### **4.6 Results**

A wide array of iron-bearing minerals was observed in the samples collected from Glacier National Park, as summarized in Table 4.1. Importantly, bulk rock magnetic techniques provide a sensitive approach for finding and describing ferromagnetic minerals, but some of these techniques may not be diagnostic for a given phase. However, when coupled to petrography, phases can be confirmed and in certain cases, the mineralization sequence can be ordinated by crosscutting relationships or informed by grain shape. We discuss the results of these analyses first from the perspective of bulk techniques identifying iron minerals and then using petrographic (including chemical imaging) techniques.

The coercivity of remanence acquisition, determined using the derivative of the IRM, can be used to make ferromagnetic mineralogical determinations

(Figs. 4.4AB; Heslop et al., 2002; Peters and Dekkers, 2003; Robertson and France, 1994). Notably, most of the samples share a similar mid-coercivity peak with a few additional different high-coercivity peaks present in some of the samples. Goethite is easily identified with coercivities over 1000 mT, and the range of 140-800 mT is generally indicative of hematite. However, the coercivity ranges for hematite, magnetite, titanomagnetite, greigite, and pyrrhotite overlap between 16-140 mT, though pyrrhotite, greigite, and hematite tend to have higher coercivities. Additionally, interpretations of coercivity data can be more difficult in natural samples where more than one ferromagnetic mineral is present. Thus other techniques are valuable to provide confirmation and/or to separately identify these minerals.

The presence of RRM can be used to identify magnetic iron-sulfide phases like pyrrhotite, although the sensitivity limits are not well understood (Snowball, 1997; Thomson, 1990). Compared using  $B_{\text{eff}}$  (applied field times ratio of RRM to ARM), several samples in the west outcrops of member 4 indicated strong evidence for magnetic iron sulfides,  $B_{\text{eff}} > \pm 20 \mu\text{T}$  at 5 rps (revolutions per second) (Potter and Stephenson, 1986; Suzuki et al., 2006), while two samples of west side member 5 displayed weaker RRM signals,  $B_{\text{eff}} > \pm 5 \mu\text{T}$  at 5 rps (Fig. 4.4C). Notably, no samples on the east side showed any RRM, and thus do not contain pyrrhotite. Additionally, all of the samples that had RRM displayed coercivity peaks greater than 100 mT, above the main mid-coercivity peak, suggesting that the lower common mid-coercivity mineral observed widely in Glacier National Park samples is magnetite.

In order to confirm the presence of magnetite and other iron-bearing minerals, Kappabridge thermosusceptibility experiments were used (Figs. 4.4E-G). Magnetite was indicated by a drop in coercivity at 580°C in all of the samples measured except one from west side outcrops of member 4. However, the Verwey transition at about -150°C was not observed, suggesting either it was suppressed due to low abundance with other phases dominating the signal, or that the magnetite contains a small weight percent titanium and could include

titanomagnetite (Kozłowski et al., 1996; Moskowitz et al., 1998). Many of the samples showed the transformation of a nonmagnetic iron-bearing mineral into magnetite through a peak of increased susceptibility starting between 400°C and 500°C that dropped at 580°C. This is interpreted as the decomposition of pyrite (Li and Zhang, 2005). Only one sample from the west side outcrop of member 4 displayed any sign of pyrrhotite's ferromagnetic to paramagnetic shift at its Curie temperature of 325°C (Horng and Roberts, 2006; Minyuk et al., 2013). No low-temperature peaks hinted at the presence of goethite. Hematite is difficult to identify using Kappabridge thermal susceptibility due to its low susceptibility. The pure hematite Curie temperature transition is rarely seen in samples with other minerals like chlorite or elements like S or C and the low-temperature Morin transition can be easily suppressed in submicron-size grains or with cation substitution (Bowles et al., 2010; Minyuk et al., 2011; Zhang et al., 2012). Indeed, Kappabridge experiments on samples containing hematite and carbon-, nitrogen- or sulfur-bearing phases are hard to distinguish from those of pyrite decomposition except that pyrrhotite sometimes forms during the cooling of pyrite, although cation substitutions can affect this process (Li and Zhang, 2005; Minyuk et al., 2011; Minyuk et al., 2013). Since no pyrrhotite was formed in our experiments, identification of pyrite using Kappabridge is only weak evidence for this mineral. The cooling curves are all much higher susceptibility than the initial heating curves in these thermosusceptibility experiments, often with a shifted peak toward lower temperatures of 200°C to 550°C. This suggests the decomposition of nonmagnetic minerals combining with other minerals to form titanomagnetite. This could be due to the reduction of paramagnetic hematite, the decomposition of ilmenite or other titanium bearing minerals, and/or another less well understood process (Hrouda, 2003; Zhang et al., 2012).

Using an empirical rock magnetic procedure called the Fuller test, one can use the ratio of the NRM:IRM to infer if the magnetization is detrital, chemical, or thermal in origin, especially when compared to the synthetic ARM:IRM relationships (Fuller et al., 1988; Fuller et al., 2002). In sedimentary rocks

deposited in approximately Earth-strength magnetic fields, NRM:IRM ratios of 1:1000 correspond to weak detrital magnetization whereas ratios of 1:10 are typical of chemical remagnetization. This test was calibrated for magnetite, and thus can only be applied to samples where the primary ferromagnetic mineral is magnetite. When applied to the samples from the Appekunny Formation that do not show RRM (no pyrrhotite) or large amounts of hematite, most of the samples show a NRM:IRM ratio of 1:1000 with a few slightly higher, but not near 1:10. These results suggest that the magnetite in these samples is detrital in origin. Results from the ARM modification of the Lowrie-Fuller test imply that this magnetite is single domain or pseudo single domain, and is probably submicron (maximum less than 10  $\mu\text{m}$ ) in size (Johnson et al., 1975; Lowrie and Fuller, 1971; Xu and Dunlop, 1995).

To quantify the amount of magnetite in the samples, we used the saturation remanent magnetization measured using IRM acquisition. Magnetite has a saturation magnetization of 92  $\text{Am}^2/\text{kg}$  (O'Reilly, 1984), and for magnetite the ratio of the saturation remanence to the saturation magnetization has been calculated for a range of grain sizes in the famous Day plot (e.g. Day et al., 1977; Dunlop, 2002). Our samples are single-domain or pseudo-single domain in size so this ratio should be between 0.5 and 0.02. By mass-normalizing a measured saturation remanence, we can divide by the saturation magnetization of magnetite times a correction factor of the ratio of saturation remanence to saturation magnetization to get approximate percentages of magnetite in our samples (e.g. Klein et al., 2014). This calculation can only be done for samples where magnetite is the only or primary ferromagnetic mineral, and due to underlying assumptions it is probably only accurate to an order of magnitude. Estimates range from tenths of a part per million (ppm) to tens of ppm of magnetite (depending on the ratio used), primarily for samples on the east side of the Glacier National Park with one from the west side.

All mineralogical identifications using light and electron microscopy were confirmed chemically/structurally using synchrotron XAS and/or EDS spectra.

All green or gray Appekunny Formation samples contained pyrite, but pyrrhotite was only observed in samples of member 4 (or Prichard Formation) on the west side of Glacier National Park (Fig. 4.5A). The presence of different sulfide phases with exotic trace metal cations such as chalcopyrite, sphalerite, galena, nickel iron monosulfide, copper sulfide, and cobalt arsenic sulfide were also observed in many samples (Fig. 4.5C). Chalcopyrite and sphalerite occurred throughout the Appekunny Formation and on both sides of the park, while galena, nickel sulfides, and cobalt sulfides were only found in member 5 (east side) and member 4 (west side). Iron oxides were also identified in many of the samples throughout the Appekunny Formation and on both sides of the park, and they were primarily confirmed chemically using EDS. XAS at the Fe K-edge was used to identify the iron oxide as goethite in one sample from member 2 (Fig. 4.5B). Iron-bearing chlorite was also ubiquitous throughout the samples, identified by electron microscopy and EDS as well as synchrotron XAS at the Fe K-edge (Fig. 4.5B). Sulfate phases were identified in many samples using S XAS (Fig. 4.5A), often with more than one sulfate salt present in a given sample. Electron microscopy and EDS characterized many of these sulfates as barite, but iron sulfates were also observed—these probably reflect the recent oxidative weathering of pyrite.

Using high-energy XRF maps, we were able to quantize the abundance of iron and trace metals for two of our samples (Table 4.2). XRF counts were correlated to mass based on standards measured during the same beam time session, then corrected for X-ray attenuation for each element and the rock matrix (assuming a homogeneous quartz lithology), then summed over a measured volume, and then divided by the sample density to find weight percent. This also implicitly assumes that a representative area was chosen for chemical imaging (Fig. 4.6). For all quantized elements, the values were remarkably similar across the park, often the same order of magnitude and similar to the second significant digit. However, comparison with previously measured bulk XRF and inductively coupled plasma-mass spectrometry (ICP-MS) elemental abundances of the



Appেকunny Formation (Table 4.2, González-Álvarez and Kerrich, 2010; González-Álvarez et al., 2006) suggests that while the textural XRF estimates for major elements (such as Fe) are within the expected range, the trace element estimates are often 2 to 16 times more abundant than observed in bulk. This could be due to differential sample analysis because given chemical imaging efforts were focused to a degree on reactive iron phases and thus the abundance of trace metals contained within these texturally late iron sulfide phases was overrepresented compared to background matrix.

Using these same XRF maps (Fig. 4.6), we estimated the volume percent of Fe-rich minerals such as iron sulfides and oxides. In this approach, the numbers of matrix pixels above a certain cutoff level of intensity of Fe signal were counted and divided by the total number of pixels in the XRF microprobe map to get a volume percent estimate (Table 4.2). This level was determined by cross-correlating the chemical maps with microscopy, XANES, and EDS to include all iron sulfides and oxides as identified in those regions but to exclude other minerals containing Fe such as chlorite. These calculations bear typical uncertainties associated with point count estimates, but avoid a certain degree of human error in phase identification (e.g. Johnson et al., 2014). Each pixel of the XRF maps represents the abundance over a volume of 10  $\mu\text{m}$  by 10  $\mu\text{m}$  by the thickness of samples, but are actually 20 x 20  $\mu\text{m}$  pixels based on the chosen measurement step-size. In exporting these images from the MicroAnalysis Toolkit for point-counting processing, the pixels are redistributed at a finer scale across the map, which leads to some averaging between pixels. Therefore to be counted in the volume estimation, the Fe-rich grains or aggregates must be sufficiently large in size, consisting of the majority of a 10 x 10  $\mu\text{m}$  area (which has been further averaged in processing), and thus disseminate grains are not included in this estimate. In this manner, the presence of large aggregates of sulfide phases versus disseminated grains in the XRF mapped region will influence the volume percent estimation. Even with these caveats, similar volume percentages of Fe-rich minerals were attained for samples from both sides of the

park and these modal abundances were the same order of magnitude as modal abundances from point-counting of other sub-biotite grade, organic-lean shales (e.g. Ferry, 1984, 2007).

From light and electron microscopy, many of the iron-bearing minerals show shapes or crosscutting textures that indicate their recrystallized and secondary nature. Much of the observed pyrite is euhedral, and often is found in large nodular aggregations from samples throughout the park (e.g. Figs. 4.7BCD). These nodules do not display evidence of differential compaction unlike early nodules in the lower Belt's Newland Formation in the Helena Embayment (Schieber, 1989; Slotznick et al., 2015) and preserved macroscale soft sediment deformation in the Appekunny Formation, implying a later diagenetic or metasomatic origin. Small aggregates of euhedral pyrite grains similar to pyrite framboids observed in modern anoxic and sulfidic sediments (Wilkin et al., 1996) were found in a few members on the east side of Glacier National Park (Fig. 4.7A), suggesting the much of the coarse euhedral pyrite could be simply recrystallized from an early diagenetic framboidal phase in these samples. These pyrite grains range in size from 1.5 to 10  $\mu\text{m}$  average width/diameter with a mean size of 4.3  $\mu\text{m}$  (standard deviation = 1.7,  $n = 168$ ), which is similar to other measured framboids and infilled framboids in the modern sediments and in sediments throughout Earth history (Wilkin et al., 1996). In samples that contain multiple sulfide phases, various textural relationships were observed. In three samples, pyrite and pyrrhotite nodules contain small inclusions of chalcopyrite and sphalerite, often near veins or fractures within the crystal (Figs. 4.7BCF); however, in other samples, sphalerite and chalcopyrite phases coexisted with pyrite as separate crystals. While pyrrhotite and pyrite were often found in the same samples, we did not observe clear crosscutting relationships between these phases. Sometimes, the pyrrhotite occurred in large aggregates with small grains of pyrite nearby, and sometimes pyrite was larger in grain size than the pyrrhotite (Fig. 4.7C). Surface weathering of iron oxides is present in many of the samples surrounding pyrite grains, and XAS showed at least one of these surrounding rims

to be goethite (Fig. 4.7D). However, rims of chlorite and/or carbonate were also observed around iron sulfides on the west side of the park (Figs. 4.7EF). On the east side of the park, chlorite was present in the background fabric of the sample instead. Barite occurred in small isolated grains sometimes with lath shapes, sometimes rounded (Fig. 4.7G), and sometimes as replacement/embayed domains with unclear origins (Figs. 4.7DG). However, one sample contained barite intimately associated with the pyrite in space-filling patterns as well as small grains and rims (Fig. 4.7H).

#### **4.7 Discussion**

Despite the well-preserved nature of the fine-grained siliciclastic Belt strata in Glacier National Park, secondary overprinting of the iron-bearing minerals in the Appekunny Formation was observed in all samples from a range of bulk and texture-specific techniques. Some of these alteration processes included recent (near) surface weathering, but many point to late diagenetic and/or metasomatic events. Nearly all pyrite has defined margins that crosscut fine-grained phases and reflect either recrystallization and coarsening of prior phases or mineralization from later fluids, although pyrite in exposures on the east side of the park appears generally better preserved with several examples consistent with early diagenetic emplacement (Fig. 4.6A). Many samples contained sulfide phases enriched in As, Zn, Cu, Pb, Ni, and Co, which indicate the mobility of these metals as well as sulfur in postdepositional recrystallization events possibly involving metasomatic fluids. Sulfide phases rich in these trace metals were observed throughout the Appekunny Formation on both sides of the park, suggesting any flow of altering fluids was not restricted to a particular stratigraphic member due to differential permeability, depth within the stratigraphy, and/or proximity to local structures. Samples with multiple sulfide phases in one nodule (found both in samples with and without pyrrhotite) emphasize the recrystallization of original iron minerals to incorporate trace-metals. The impact of metasomatic fluids on the Appekunny Formation has been

well noted by previous studies (González-Álvarez and Kerrich, 2010; González-Álvarez et al., 2006); however, less consideration has been given to how these processes have impacted the iron mineralogy, and the quality of interpretations of paleoenvironmental processes and chemistry of Belt Basin waters made from redox proxy data.

Pyrrhotite was found in several samples from the west side of Glacier National Park. Overall, the bulk magnetic technique of RRM appears to be a valuable indicator of the presence of magnetic iron sulfides even in samples with multiple ferromagnetic components. Pyrrhotite was confirmed using XANES and EDS in all three samples that showed a strong RRM signal. Similarly, no pyrrhotite was found in samples that showed no RRM signal. Pyrrhotite was not found texturally in the two samples with moderate RRM signal ( $\pm 20 > B_{\text{eff}} > \pm 5$   $\mu\text{T}$  at 5 rps), but these grains could be very small with a weaker signal due to the overwhelming presence of other ferromagnetic minerals or another magnetic mineral could be capable of producing moderate RRM. The fact that pyrrhotite was only observed in samples from the west side of Glacier National Park, both in bulk and textural measurements, highlights local variations in metamorphic conditions in samples separated by only 26 km (though palinspastic reconstruction might restore a larger distance). Although modern examples of detrital pyrrhotite and early diagenetic pyrrhotite have been found in unique environments (Hornig and Roberts, 2006; Larrasoana et al., 2007), much of the pyrrhotite in the rock record is interpreted to be due to the transformation of pyrite into pyrrhotite during metamorphism or precipitation from high temperature fluids (e.g. Craig and Vokes, 1993; Hall, 1986; Weaver et al., 2002). In the presence of organic matter or a reducing environment, pyrite may transform to pyrrhotite beginning at 200°C (Hall, 1986), with some experiments indicating that pyrrhotite can form at even lower temperatures depending on lithological constraints (Moreau et al., 2005; Raub et al., 2012). Although pyrrhotite formation is variable based on lithological constraints like organic matter (e.g. Carpenter, 1974), our new stratigraphic correlations suggest that the appearance

of pyrrhotite is linked to different metamorphic conditions on the west side of the park and is not simply due to lithological differences between stratigraphic members. Although recent studies often screen for pyrrhotite (e.g. Asael et al., 2013; Planavsky et al., 2011), the presence of pyrrhotite makes interpreting iron speciation analyses tricky because it apportions iron to a highly reactive pool usually composed of oxides and carbonates; furthermore it can be difficult to mass balance iron and sulfur even when accounting for the iron in pyrrhotite as the iron and sulfur budgets associated with pyrrhotization of pyrite in open systems remain unknown (Asael et al., 2013; Craig and Vokes, 1993; Piatak et al., 2007; Shannon and White, 1991; Zhou et al., 1995). Due to the lack of quantification for pyrrhotite, it is unclear the extent to which the pyrrhotite noted in these samples has impacted the bulk iron speciation data; however, the widespread observation of pyrrhotite on the west side of Glacier National Park shows that secondary processes have played a role in changing the iron geochemistry of these strata.

The presence of pyrrhotite only on the west side of the park is consistent with increasing burial metamorphism to the west, similar to the overall trend seen across the Belt Supergroup due to thickening of the section (Duke and Lewis, 2010; Winston and Link, 1993). Indeed, pyrrhotite has been widely observed in the Prichard Formation to the west of Glacier National Park, and linked via geochemistry to the metamorphic transformation of pyrite (Luepke, 1999; Luepke and Lyons, 2001). Within Glacier National Park, the appearance of pyrrhotite could be linked to transformations at deeper burial depths in a reducing environment probably an open system, but distinct fluids could also have delivered and/or removed dissolved iron and sulfide to precipitate pyrrhotite (e.g. Hall, 1986). Supporting this suggestion is the observation that cobalt arsenic base metal sulfides from the west side of the park are closely texturally associated with the pyrrhotite. Notably the chlorite rims surrounding the pyrrhotite and pyrite aggregates on the west side of the park suggest an even later transformation (and redox change) of iron from sulfides into a mixed valence silicate phase. This

highlights the increased mobility of iron between different minerals on the west side of the park explainable by either of the mechanisms detailed above, but in a second alteration event after pyrrhotite had already formed.

One of the most interesting iron mineralogical findings in this study was the discovery of nearly ubiquitous submicron-size magnetite across all of the Appekunny Formation in all members. Results from the rock magnetic Fuller test suggest that this magnetite is detrital due to its low ratio of NRM:IRM, whereas chemical precipitation would be expected to have a much stronger magnetization than was observed. The evidence for detrital magnetite is important because it represents a significant delivery process of iron into the system that is not directly linked to the redox chemistry of the depositional waters. In bulk geochemical iron speciation measurements, abundant preserved detrital magnetite would skew results toward an interpretation of ferruginous waters; however, the amounts of magnetite present in our samples are too low to dramatically impact the results of bulk geochemical extraction techniques. The observations of detrital iron fluxes provide an important view of the iron systematics in the basin, by documenting an important supply of highly reactive iron to the basin (e.g. Canfield and Berner, 1987). Furthermore, the preservation of at least some of this magnetite suggests that a large anoxic H<sub>2</sub>S-rich zone (either in the water column or as sedimentary pore fluids), if present during deposition of the strata in Glacier National Park, was not sufficient to scavenge all this highly reactive iron to form pyrite (Canfield and Berner, 1987; Lyons and Severmann, 2006). Additionally neither the water column nor pore fluids were sufficiently rich in ferrous iron to recrystallize detrital magnetite and generate a chemical remanent magnetization (e.g. Skomurski et al., 2010).

The presence of shallow-water hematite-bearing red units in member 1 of the Appekunny Formation as well as in the overlying Grinnell Formation highlights the presence of oxygen in the atmosphere and shallow waters. All of the units in the Appekunny Formation of Glacier National Park represent relatively shallow water environments of the Belt Basin, and based on

sedimentary structures from orbital water motion, long-lived stratification of the water column seems unlikely. However, the framboidal pyrite in samples from the east side of Glacier National Park (and perhaps even much of the recrystallized pyrite seen elsewhere), suggests the precipitation of early diagenetic pyrite during organic diagenesis. Thus pyrite is reasonably interpreted as an indicator of primary anoxic and sulfidic sedimentary environments in the Belt Basin, but based on the constraints noted earlier herein suggesting oxic, nonstratified conditions in shallow waters, it seems likely that these conditions were effectively limited to sediment pore waters. Detrital iron oxides likely provided an important source of highly reactive iron for pyrite formation during organic diagenesis (Canfield and Berner, 1987; Raiswell and Canfield, 1998). Based on our observations, the shallow waters and sediments of the Belt Basin preserved in Glacier National Park do not show any signs of being anoxic and sulfur-poor (i.e. ferruginous conditions) as was hypothesized for older, more distal sediments further south in the basin (Planavsky et al., 2011). The barite closely associated with pyrite in space-filling patterns (Fig. 4.7H) suggests at least some of the barite precipitated from diagenetic and/or metasomatic reactions with deep fluids and may not be representative of sulfate in the depositional waters (Griffith and Paytan, 2012; Hanor, 2000). The presence of authigenic replacement barite not associated with iron sulfides found in many of the samples (Figs. 4.7DG) could in principle record postdepositional oxidizing fluids, although these micron-scale grains may instead reflect precipitation during early organic diagenesis, associated with vacillating redox fronts of sulfate reduction with pore fluid sulfate sourced from bottom waters (Griffith and Paytan, 2012; Koski and Hein, 2004). Water column or detrital barite could be a component of our samples, but no lath-shaped euhedral barite was identified and while rounded grains were observed (Fig. 4.7G), they often occurred near barite displaying replacement or embayed textures. This suggests much of the either water column or detrital barite was recrystallized after deposition.

Ultimately, the iron mineralogy and geochemistry of the Appekunny Formation and surrounding formations suggest a redox structure of (relatively) shallow mid-Proterozoic sedimentary basins that was similar to today with detrital iron fluxes carried through oxygenated waters, wherein sedimentary environments with sufficient organic carbon loads exhausted their supply of O<sub>2</sub> and underwent anaerobic respiratory metabolisms that promoted sulfidic pore fluids and the production of diagenetic pyrite. Additionally, from the data generated in this study, we can link evidence for oxygenated waters directly to outcrops known to contain the early macroscale fossil *Horodyskia moniliformis*, a putative (aerobic) eukaryote. Understanding the depths in the Belt Basin to which water was oxygenated and whether anoxic and sulfidic conditions emerged from the sediments into the water column in more distal sedimentary settings (Gellatly and Lyons, 2005; Luepke and Lyons, 2001; Slotznick et al., 2015), or whether the water column instead became anoxic and ferruginous (Planavsky et al., 2011) remains a priority for future work.

Although our iron mineralogy analyses shed light onto questions about redox and geochemistry of the Belt Basin, they are not as straightforward in aiding in stratigraphic correlations across Glacier National Park. Sulfides rich in Zn, Cu, and Pb were found on both sides of the park, and they do not appear to be restricted to any single stratigraphic member. Similarly, pyrrhotite appears to be a characteristic of the west side of Glacier National Park and is not restricted to a single member. It is noteworthy that the abundance of pyrrhotite (as well as pyrite) in samples on the west side of Glacier National Park was distinct between different units. Appekunny member 4/Prichard-like lithologies from the west face of Mount Brown and McDonald Creek contained abundant pyrrhotite, as did samples in proposed member 4 on the east face of Mount Brown. Samples from member 5 in McDonald Creek and from proposed member 5 on the east face of Mount Brown contained smaller proportions or no pyrrhotite. This suggests a stratigraphic link between samples on the west side of Mount Brown and the better-studied McDonald Creek region and supports the hypothesis that the strata



on the east face of Mount Brown are metamorphosed equivalents of member 4, maybe even the same member as the more Prichard-like samples on the west face and in McDonald Creek. Additionally, member 4 siltstones and claystones on the east side of the park contained abundant pyrite, which could reflect the mineralogical progenitor of the abundant pyrrhotite seen on the west side of the park in these ambiguously correlated units.

#### 4.8 Conclusion

The Appekunny Formation of Glacier National Park is an excellently preserved shallow-water unit that, while complicated by postdepositional processes, still contains records of primary redox chemistry of the Belt Basin during mid-Proterozoic time when macroscopic life was emerging. From our iron mineralogy and chemical observations, we propose that the shallow waters in the Belt Basin were oxygenated, but with underlying suboxic  $\text{H}_2\text{S}$ -rich pore waters that promoted precipitation of pyrite. This water chemistry and these redox processes are similar to those of shallow sedimentary basins today, and they may help to explain why these rocks are notably fossiliferous (e.g. Horodyski et al., 1989), as many of the preserved biota are interpreted as (different) aerobic organisms. In the sedimentary rocks of Glacier National Park, most of the strata capture paleoenvironments that would have been habitable to diverse sets of aerobic organisms. Our interpretations of the paleoenvironment in Glacier National Park provide a geochemical constraint on paleoredox conditions that helps to support the hypotheses from many paleontologists that some of the macroscale and microscale fossils found in Glacier National Park and in the rest of the Belt Basin were early eukaryotes (e.g. Adam et al., 2014; Fedonkin and Yochelson, 2002; Horodyski, 1993; Retallack et al., 2013; Walter et al., 1976; Walter et al., 1990). It is possible that portions of the Belt Basin could have been anoxic or euxinic (e.g. Slotznick et al., 2015) in either a stratified or locally heterogeneous manner, but these paleoredox constraints are distinct in time and record deeper water environmental settings than the fossiliferous units focused on

in this work. Iron mineralogy preserved in Precambrian rocks is rich and complex with the possibility of many different redox and phase transformations. By combining textural and bulk techniques, it is possible to untangle the iron phases to get a picture of key redox processes operating in the environment and the postdepositional processes that have served to complicate our interpretation of that history.

#### **4.9 Acknowledgements**

We thank Rob Thomas, Tim Lyons, Austin Chadwick, and Steven Skinner for assistance with stratigraphic measurements and sample collections under National Park Service collection permits # GLAC-2012-SCI-0195 and GLAC-2014-SCI-0008. Thanks also go to Jim Sears, Johnny MacLean, Erik Sperling, and an anonymous reviewer for helpful comments that greatly improved the manuscript. Support for this work was provided by the Agouron Institute, a Tobacco Root Geological Society scholarship, a Belt Association student research grant, a Geological Society of America student research grant, National Aeronautics and Space Administration (NASA) Exobiology program (Fischer), the David and Lucile Packard Foundation (Fischer), National Science Foundation Graduate Research Fellowship program (Slotznick), a NASA Earth and Space fellowship (S.P.S.), and a Philanthropic Educational Organization Scholar Award (Slotznick). Portions of this research were carried out at the Stanford Synchrotron Radiation Lightsource, a Directorate of SLAC National Accelerator Laboratory, and an Office of Science User Facility operated for the U.S. Department of Energy Office of Science by Stanford University.

## 4.10 Tables

**Table 4.1: Mineral identifications from samples of the Appekunny, Grinnell, and Prichard Formations**

	East side of Glacier National Park							West side of Glacier National Park		
	Mbr. 1 (red)	Mbr. 1 (green)	Mbr. 2	Mbr. 3	Mbr. 4	Mbr. 5	Grinnell	Prichard/ Mbr. 4*	Mbr. 4†	Mbr. 5
<u>Bulk Techniques</u>										
Magnetite		X	X	X	X	X		X	X	X
Hematite	X				X	X	X		X	X
Goethite	X	X	X	X			X		X	X
Pyrite			X		X			X		
Pyrrhotite								X	X	X
<u>Textural Techniques</u>										
Goethite			X							
Iron Oxide (generic)	X	X	X		X		X	X	X	X
Pyrite		X	X	X	X	X		X	X	X
Pyrrhotite								X	X	
Chalcopyrite		X				X		X	X	X
Galena						X			X	
Sphalerite		X			X	X		X	X	X
Nickel Iron Monosulfide								X		
Cobalt Arsenic Sulfide									X	
Copper Sulfide									X	
Ferric Disulfide						X				
Chlorite	X	X	X	X	X	X		X	X	X
Barite	X	X	X	X	X				X	
Sulfate (generic)		X		X	X			X	X	
*Samples from the east face of Mt. Brown and McDonald Creek										
†Samples from the west face of Mt. Brown										

<b>Sample*</b>	<b>Member</b>	<b>Location*</b>	<b>Fe (wt%)</b>	<b>Ti (wt%)</b>	<b>Mn (wt%)</b>	<b>Cu (ppm)</b>	<b>As (ppm)</b>	<b>Zn (ppm)</b>	<b>Ni (ppm)</b>	<b>Fe-rich mineral (vol%)†</b>
GP12-8, Reg1	Member 4	West, McD	2.01	0.232	0.042	21.3	42.7	106	131	0.2
GP12-1, Reg4	Member 2	East	3.54	0.213	0.000056	21.7	40.1	143	237	0.3
Average Published Appekunny Formation Data§			2.59± 0.55	0.294± 0.045	0.037± 0.024	12.4± 11.0	2.57± 1.41	58.3± 18.3	22.6± 8.33	

\* Reg stands for Region, East stands for east side of Glacier National Park, West stands for west side of Glacier National Park, McD stands for McDonald Creek

† Based on point counting XRF map, this includes iron sulfides and oxides that represent most of a 6 or 13 µm square pixel

§ Data from silt and claystones of González-Álvarez et al. (2006) and González-Álvarez & Kerrich (2010), Averaged with 1 population standard deviation, n= 16 for Fe, Ti, Mn, As, and Ni, n = 12 for Cu and Zn

4.11 Figures

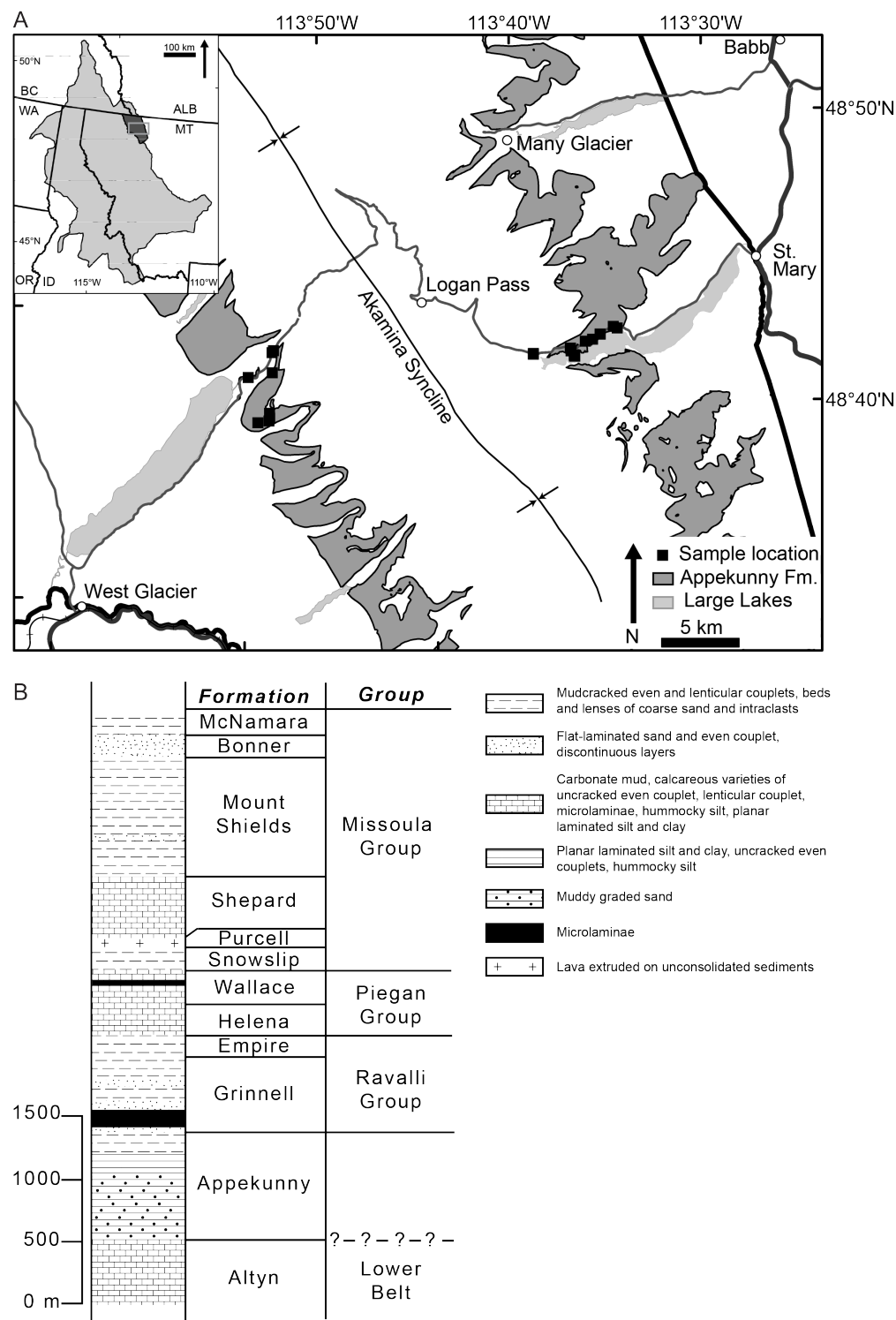


Figure 4.1: (A) Map of sample localities in Glacier National Park, as well as exposures of Appekunny Formation. Inset map shows location of these samples

within the larger Belt Supergroup outcrops. State/province abbreviations: OR—Oregon, ID—Idaho, MT—Montana, WA—Washington, BC—British Columbia, ALB—Alberta. (B) Generalized stratigraphy and stratigraphic nomenclature of the units exposed on the east side of Glacier National Park. See text for details.

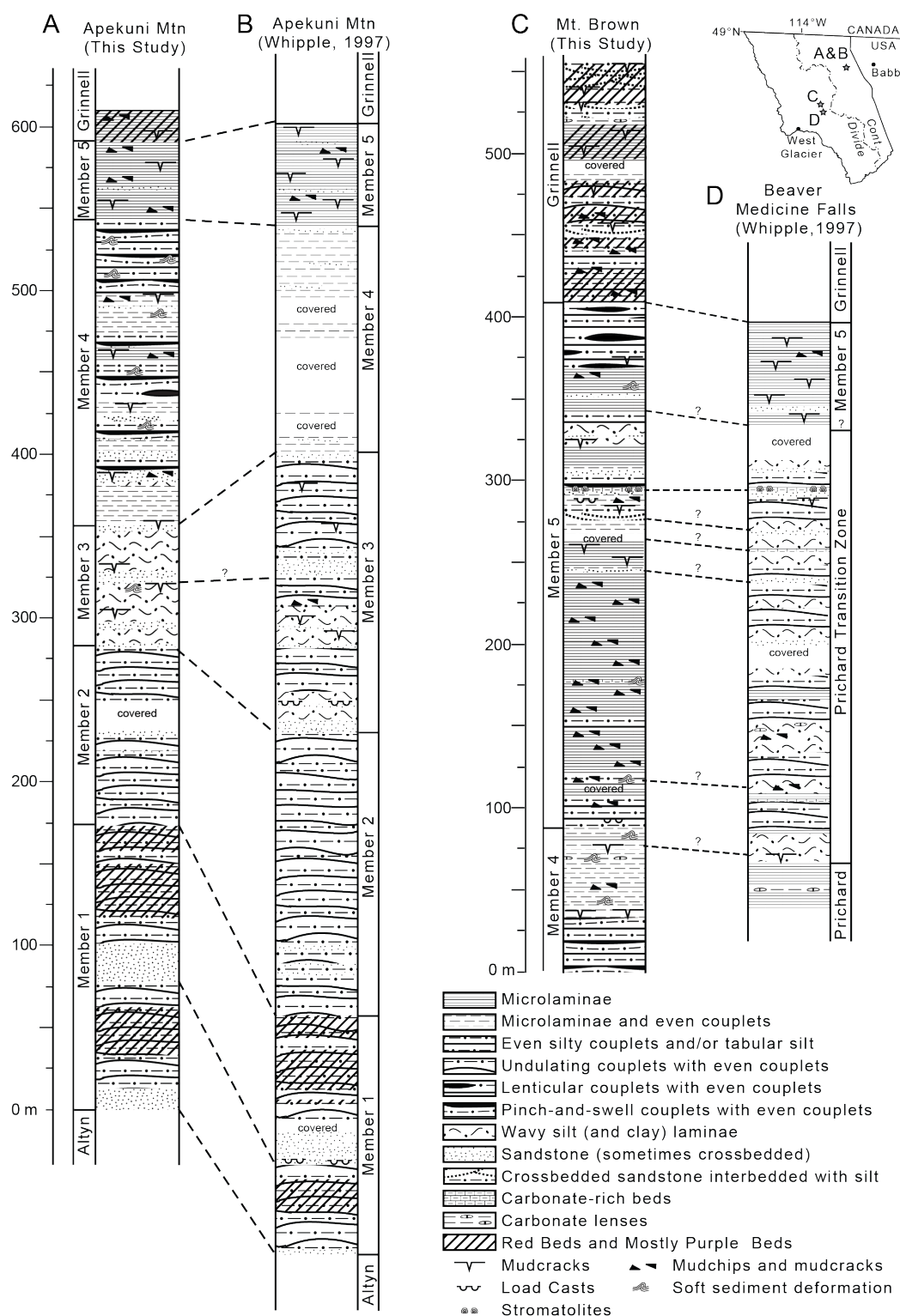


Figure 4.2: Stratigraphic columns of the Apekunny Formation. Scale is in meters and applies to all stratigraphic columns shown. Top right inset: Map showing approximate locations of the stratigraphic columns in Glacier National Park.

Note: Cont. Divide—Continental Divide. (A) New stratigraphic section of the Appekunny Formation at the type section at Apekuni Mountain, Many Glacier. (B) Original stratigraphic section detailing the Appekunny Formation's 5 informal members at the type section of Apekuni Mountain, Many Glacier from Whipple et al. (1997). (C) New stratigraphic section from the east face of Mount Brown as well as new interpretation of the units present. Sedimentology is summarized in the text. (D) Stratigraphic section from Beaver Medicine Falls, Edwards Mountain showing Prichard Formation and Prichard transition zone interpretations from Whipple et al. (1997).



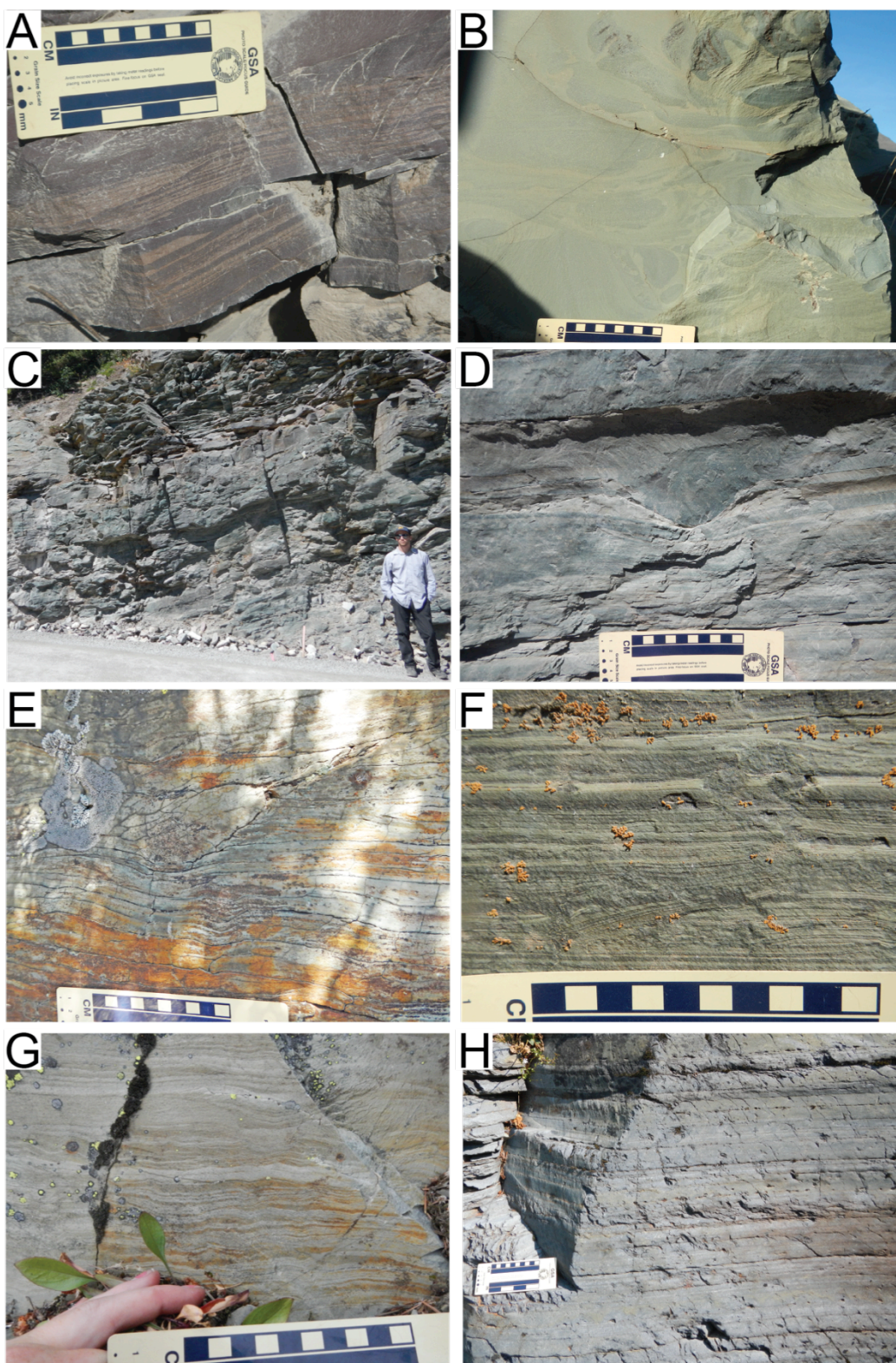


Figure 4.3: Photographs of Appekunny Formation member lithotypes and sedimentary structures along the Going-to-the-Sun Road. (A) Ripple cross-

stratification in member 1. (B) Soft-sediment deformation load structures and plumose fracturing in member 2. Person is 1.8 m for scale. (C) Large-scale hummocky cross stratification in member 3 (D) Centimeter-scale gutters in member 3. (E) Soft sediment deformation and scour in lenticular beds of interbedded siltstone and claystone in member 4 on the east side. Note red iron oxides from weathering of iron sulfides. (F) Mud cracks and mud chips in flat even laminations of alternating siltstone and claystone in member 5 on the east side. (G) Lenticular siltstone and claystone couplets as well as soft-sediment deformation on east face of Mount Brown. (H) Gray siltstone and claystone even couplets with continuous beds rich in iron sulfides on the west side of Mount Brown.

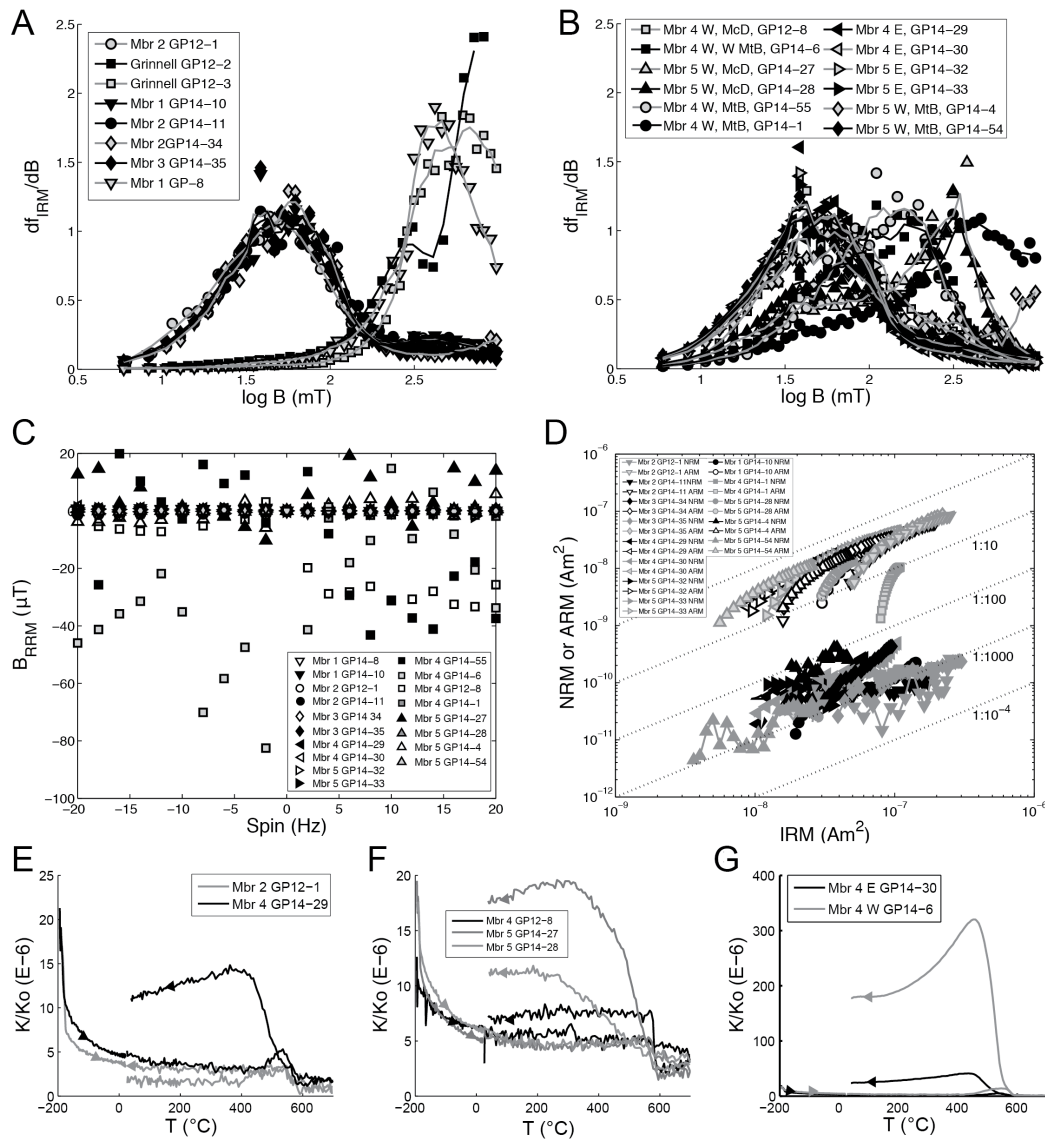


Figure 4.4: Bulk rock magnetic techniques. (A) Derivative of isothermal remanent magnetization (IRM) acquisition with respect to the applied field to determine coercivity of remanence acquisition for Grinnell Formation and Appekunny members 1-3. Abbreviations:  $f_{IRM}$ —normalized IRM,  $B$ —applied field. (B) Derivative of the IRM acquisition for members 4-5 separated by location in the park. Abbreviations: E—east side, W—west side, MtB—east face of Mount Brown, W MtB—west side of Mount Brown, McD—McDonald Creek. (C) Rotational remanent magnetization (RRM) of the Appekunny Formation samples to assess the presence or absence of magnetic iron sulfide phases. (D) Fuller test to determine origin of magnetization in samples not showing RRM or dominant hematite. (E-G) KappaBridge thermal susceptibility (abbreviated as K) to determine mineralogy, with arrows showing direction of heating, including samples from the east side of the park (E), samples from the west side of the park

(F), and some samples with strong signals (G). Sample stratigraphic member assignment is noted by number and by side of the park in part G. Data are normalized to an empty holder measurement (abbreviated as Ko).



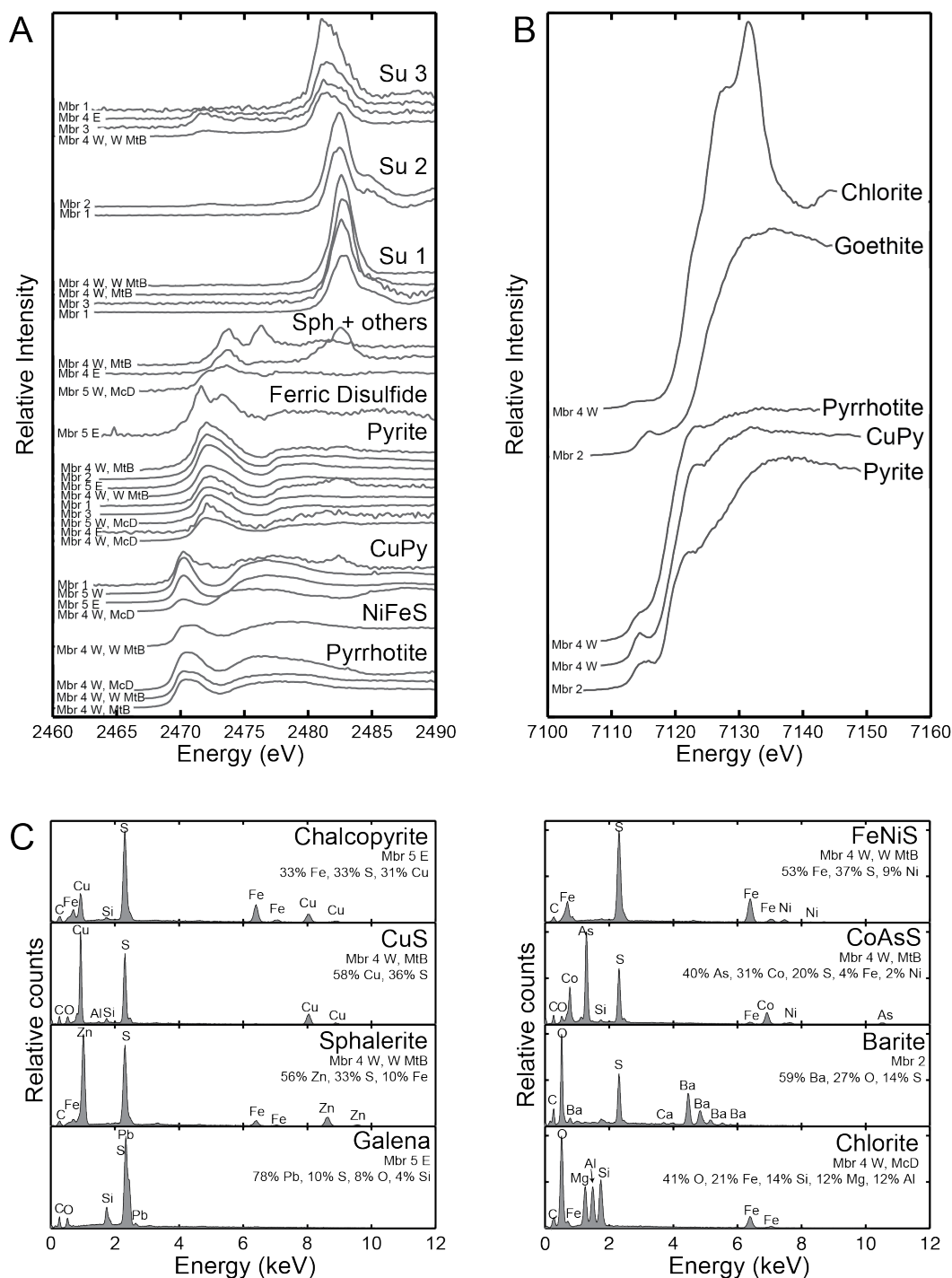


Figure 4.5: (A) End-member S X-ray absorption near-edge spectroscopy (XANES) spectra shown to exhibit mineralogical diversity found in each Appekunny member across different locations. Abbreviations for minerals: NiFeS—nickel iron monosulfide, CuPy—chalcopyrite, Sph—sphalerite, Su—sulfate. Abbreviations for location: E—east side, W—west side, MtB—east face

of Mount Brown, W MtB—west side of Mount Brown, McD—McDonald Creek. Note that three different sulfate phases are indicated by small shifts in the K-edge position. (B) End-member Fe XANES spectra for two samples, one from the member 2 and one from member 4 in McDonald Creek on the west side of Glacier National Park; abbreviation of CuPy—Chalcopyrite. (C) X-ray energy dispersive spectrometer (EDS) spectra for examples of chalcopyrite, copper sulfide, sphalerite, galena, iron nickel, sulfide, cobalt arsenic sulfide, barite and chlorite. Same abbreviations as part A; chemical composition is included in wt% of chemical species. Samples were carbon coated for analysis and carbon peaks result from this process.

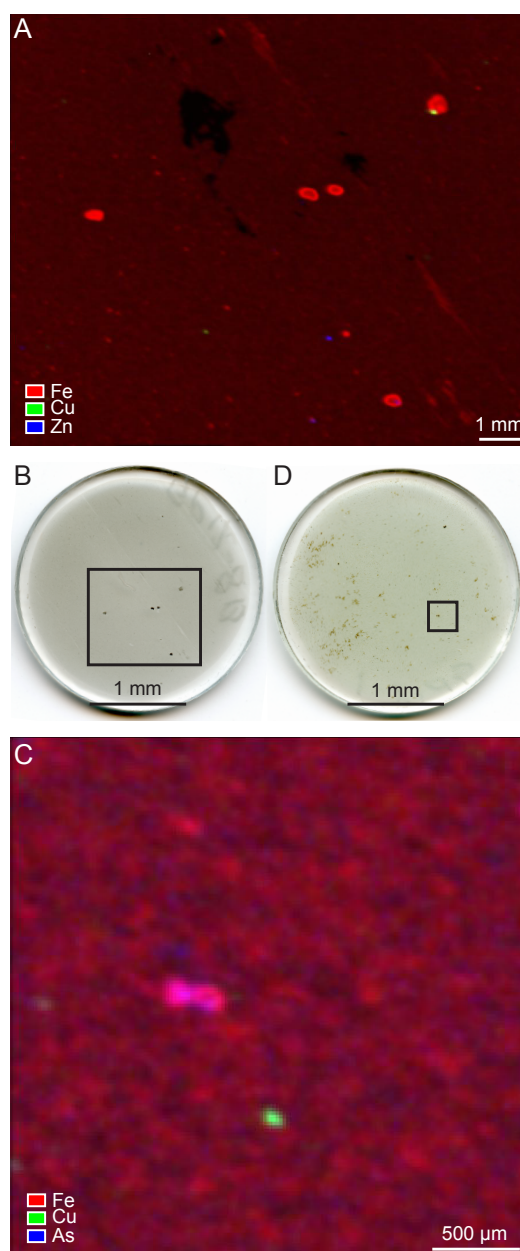


Figure 4.6: X-ray fluorescence (XRF) microprobe maps of elemental abundance used in quantification calculations as well as corresponding thin section scans. Each image has its own scale bar. (A) XRF for region 1 in GP12-8, member 4 west side on McDonald Creek. Color scales go from black at 0 to being brightly colored at maximum. Scale ranges are Fe = 0 to  $4.69\text{E-}4$   $\mu\text{g}$ , Cu = 0 to  $2.52\text{E-}5$   $\mu\text{g}$ , Zn = 0 to  $9.20\text{E-}5$   $\mu\text{g}$ . (B) Scan of GP12-8 thin section showing region chosen for XRF map. (C) XRF for region 4 in GP12-1, member 2 east side. Color scales range from black at 0 to being brightly colored at maximum. Scale ranges are Fe = 0 to  $4.38\text{E-}4$   $\mu\text{g}$ , Cu = 0 to  $3.49\text{E-}6$   $\mu\text{g}$ , and As = 0 to  $1.85\text{E-}6$   $\mu\text{g}$ . (D) Scan of GP12-1 thin section showing region chosen for XRF imaging.

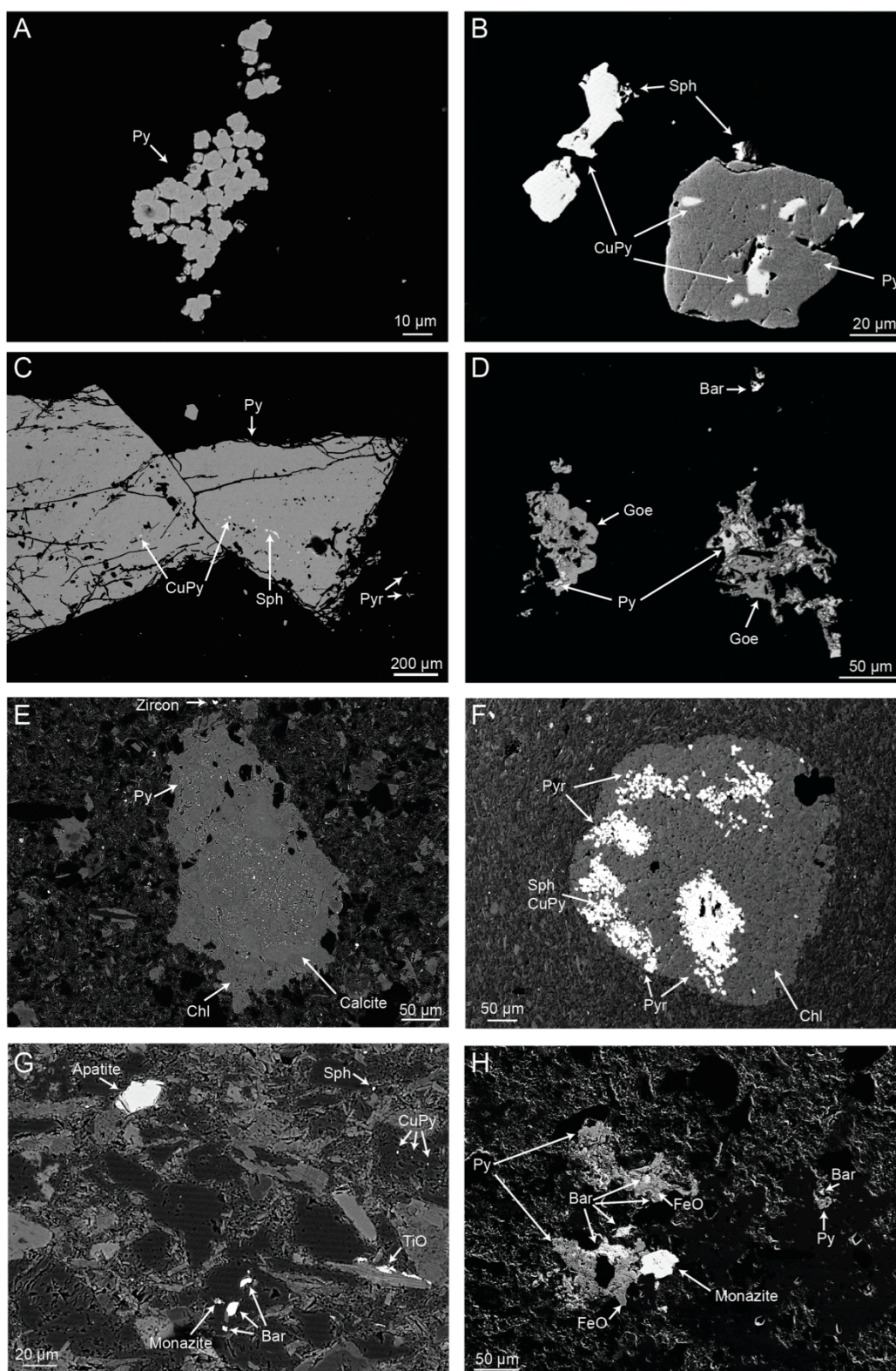


Figure 4.7: Backscatter Electron and Scanning Electron images each with own scale bar. Abbreviations for labeled minerals: Py—pyrite, CuPy—chalcopyrite,



Sph—sphalerite, Pyr—pyrrhotite, Goe—goethite, Bar—barite, Chl—chlorite, TiO—titanium oxide, FeO—iron oxide (generic). (A) Small framboidal pyrite grains in Appekunny member 3 (GP14-35). (B) Pyrite grain with inclusions of chalcopyrite and sphalerite as well as neighboring chalcopyrite grain in Appekunny member 5, east side outcropping (GP14-32). (C) Large nodular pyrite grain with small neighboring pyrrhotite grains in member 4/Prichard west side of park (GP14-6). (D) Goethite surrounding pyrite grains interpreted as replacement of euhedral recrystallized nodules in member 2 (GP12-1). (E) Small pyrite grains within carbonate nodule, rimmed by chlorite in member 5 west side of park (GP14-27). (F) Chlorite rim replacing pyrrhotite nodule in member 4/Prichard west side of park (GP12-8). (G) Individual barite grains far from sulfides or other sulfates in member 1 (GP14-10). (H) Barite rimming pyrite and iron oxides filling spaces as well as replacing grains in member 2 (GP14-11).

## 4.12 Supplemental Tables

Table S4.1: Detailed Sample Data For Glacier National Park Samples

Sample	GPS Location		Formation	Side of Park	Descriptive Location	Lithology
	Lat (°N)	Long (°W)				
GP14-8	48.69420	113.54347	Appelukunny Member 1	East	Going-to-the-Sun Road, St. Mary Lake	Red claystone and siltstone in even microlaminae
GP14-10	48.69485	113.54699	Appelukunny Member 1	East	Going-to-the-Sun Road, St. Mary Lake	Green siltstone from tabular weathering siltstone with even couplets, near ripple cross stratification
GP12-1	48.68959	113.55764	Appelukunny Member 2	East	Going-to-the-Sun Road, St. Mary Lake	Massive-weathering green siltstone with concoidal fractures, near wavy laminations and soft sediment deformation
GP14-11	48.68952	113.55772	Appelukunny Member 2	East	Going-to-the-Sun Road, St. Mary Lake	Massive-weathering green siltstone near faint wavy laminations and soft sediment deformation
GP14-34	48.68609	113.56375	Appelukunny Member 3	East	Going-to-the-Sun Road, St. Mary Lake	Green siltstone with wavy laminations and silt-clay couplets, large m-scale hummocks
GP14-35	48.68449	113.56968	Appelukunny Member 3	East	Going-to-the-Sun Road, St. Mary Lake	Green siltstone in large m-scale hummock, wavy laminations and silt-clay couplets
GP14-29	48.67574	113.57782	Appelukunny Member 4	East	Sun Point, St. Mary Lake	Grayish green interbedded siltstone and claystone with shaly parting and microlaminae, oxidized bedding planes and fractures
GP14-30	48.67524	113.57734	Appelukunny Member 4	East	Sun Point, St. Mary Lake	Gray siltstone and claystone in microlaminae, even couplets, and lenticular couplets with soft sediment deformation and oxidized bedding planes
GP14-32	48.67810	113.58099	Appelukunny Member 5	East	Sun Point, St. Mary Lake	Green claystone and siltstone in even and wavy microlaminae with mudcracks and mudchips with a few orangish laminations, near lenses of quartz sandstone
GP14-33	48.67961	113.58194	Appelukunny Member 5	East	Sun Point, St. Mary Lake	Green claystone and siltstone in even microlaminae with mudcracks, mudchips, and other soft sediment deformation features, oxidized fractures
GP12-2	48.67411	113.61337	Grinnell	East	Going-to-the-Sun Road, St. Mary Lake	Red clay-rich siltstone with euhedral rhombohedral and cubic mm-sized pseudomorphs in siltstone-claystone even couplets with mudcracks and mudchips
GP12-3	48.67374	113.61325	Grinnell	East	Going-to-the-Sun Road, St. Mary Lake	Red interbedded claystone and siltstone microlaminae with mudcracks, mudchips, and other soft sediment deformation, euhedral rhombohedral and cubic mm-sized pseudomorphs
GP12-8	48.64159	113.85725	Prichard or Appelukunny Member 4	West	McDonald Creek	Dark gray siltstone and claystone in even couplets and microlaminae with continuous laminae of mm-scale oxidizing iron sulfides
GP14-6	48.64593	113.83690	Prichard or Appelukunny Member 4	West	West Mt. Brown	Dark gray siltstone and claystone in even couplets and microlaminae with continuous laminae of mm-scale oxidizing iron sulfides
GP14-1	48.61807	113.83498	Appelukunny Member 4	West	East Mt. Brown	Green siltstone and gray claystone in even and pinch-and-swell couplets, oxidized iron sulfides
GP14-55	48.61634	113.84432	Appelukunny Member 4	West	East Mt. Brown	Greenish grey siltstone and claystone wavy laminations with mudcracks and soft sediment deformation and oxidized bedding planes and mm-sized grains, vertical mm-wide quartz veins
GP14-27	48.65734	113.83917	Appelukunny Member 5	West	McDonald Creek	Green mudchip breccia in orangish green siltstone, near even and wavy microlaminae of claystone and siltstone with mudcracks and mudchips
GP14-28	48.65857	113.83808	Appelukunny Member 5	West	McDonald Creek	Green claystone and siltstone in even microlaminae with mudcracks, mudchips and other soft sediment deformation, oxidization along fractures
GP14-4	48.61971	113.83451	Appelukunny Member 5	West	East Mt. Brown	Massive-weathering green siltstone with microlaminae, mudcracks, mudchips, and soft sediment deformation
GP14-54	48.62255	113.83518	Appelukunny Member 5	West	East Mt. Brown	Green siltstone and claystone microlaminae with mudchips, mudcracks, and other soft sediment deformation, vertical cm-wide quartz veins

#### 4.13 References

- Adam, Z., Mogk, D., Skidmore, M., and Butterfield, N., Microfossils from the Greyson Formation, Lower Belt Supergroup: Support for early Mesoproterozoic biozonation, *in* Proceedings Geological Society of America Abstracts with Programs 2014, Volume 46, p. 71.
- Anderson, H. E., and Davis, D. W., 1995, U-Pb geochronology of the Moyie sills, Purcell Supergroup, southeastern British Columbia: implications for the Mesoproterozoic geological history of the Purcell (Belt) basin: *Canadian Journal of Earth Sciences*, v. 32, no. 8, p. 1180-1193.
- Asael, D., Tissot, F. L., Reinhard, C. T., Rouxel, O., Dauphas, N., Lyons, T. W., Ponzevera, E., Liorzou, C., and Chéron, S., 2013, Coupled molybdenum, iron and uranium stable isotopes as oceanic paleoredox proxies during the Paleoproterozoic Shunga Event: *Chemical Geology*, v. 362, p. 193-210.
- Bowles, J., Jackson, M., and Banerjee, S., 2010, Interpretation of low-temperature data Part II: the Hematite Morin transition: *IRM Quarterly*, v. 20, p. 1-10.
- Canfield, D., 1998, A new model for Proterozoic ocean chemistry: *Nature*, v. 396, no. 6710, p. 450-453.
- Canfield, D. E., and Berner, R. A., 1987, Dissolution and pyritization of magnetite in anoxic marine sediments: *Geochimica et Cosmochimica Acta*, v. 51, no. 3, p. 645-659.
- Carpenter, R. H., 1974, Pyrrhotite isograd in southeastern Tennessee and southwestern North Carolina: *Geological Society of America Bulletin*, v. 85, no. 3, p. 451-456.
- Cloud, P. E., 1968, Atmospheric and Hydrospheric Evolution on the Primitive Earth: *Science*, v. 160, no. 3829, p. 729-736.
- Craig, J. R., and Vokes, F. M., 1993, The metamorphism of pyrite and pyritic ores: an overview: *Mineralogical Magazine*, v. 57, no. 1, p. 3-18.
- Cressman, E. R., 1989, Reconnaissance stratigraphy of the Prichard Formation (Middle Proterozoic) and the early development of the Belt Basin, Washington, Idaho, and Montana: United States Geological Survey, Professional Paper, v. 1490, p. 80.
- Dahlstrom, C. D., 1970, Structural geology in the eastern margin of the Canadian Rocky Mountains: *Bulletin of Canadian Petroleum Geology*, v. 18, no. 3, p. 332-406.

Day, R., Fuller, M., and Schmidt, V., 1977, Hysteresis properties of titanomagnetites: grain-size and compositional dependence: *Physics of the Earth and Planetary Interiors*, v. 13, no. 4, p. 260-267.

Dong, L., Xiao, S., Shen, B., and Zhou, C., 2008, Silicified *Horodyskia* and *Palaeopascichnus* from upper Ediacaran cherts in South China: tentative phylogenetic interpretation and implications for evolutionary stasis: *Journal of the Geological Society*, v. 165, no. 1, p. 367-378.

Duke, E. F., and Lewis, R. S., 2010, Near infrared spectra of white mica in the Belt Supergroup and implications for metamorphism: *American Mineralogist*, v. 95, no. 7, p. 908-920.

Dunlop, D. J., 2002, Theory and application of the Day plot (Mrs/Ms versus Hcr/Hc) 1. Theoretical curves and tests using titanomagnetite data: *Journal of Geophysical Research: Solid Earth*, v. 107, no. B3, p. EPM 4-1-EPM 4-22.

Dunlop, D. J., and Özdemir, Ö., 1997, *Rock magnetism: fundamentals and frontiers*, Cambridge University Press.

Elston, D., Enkin, R., Baker, J., and Kisilevsky, D., 2002, Tightening the Belt: Paleomagnetic-stratigraphic constraints on deposition, correlation, and deformation of the Middle Proterozoic (ca. 1.4 Ga) Belt-Purcell Supergroup, United States and Canada: *Geological Society of America Bulletin*, v. 114, no. 5, p. 619-638.

Eslinger, E. V., and Savin, S. M., 1973, Oxygen isotope geothermometry of the burial metamorphic rocks of the Precambrian Belt Supergroup, Glacier National Park, Montana: *Geological Society of America Bulletin*, v. 84, no. 8, p. 2549-2560.

Evans, K. V., Aleinikoff, J. N., Obradovich, J. D., and Fanning, C. M., 2000, SHRIMP U-Pb geochronology of volcanic rocks, Belt Supergroup, western Montana: evidence for rapid deposition of sedimentary strata: *Canadian Journal of Earth Sciences*, v. 37, no. 9, p. 1287-1300.

Fedonkin, M. A., and Yochelson, E. L., 2002, Middle Proterozoic (1.5 Ga) *Horodyskia moniliformis* Yochelson and Fedonkin, the oldest known tissue-grade colonial eucaryote: *Smithsonian Contributions to Paleobiology*, v. 94, p. 29.

Ferry, J. M., 1984, A biotite isograd in south-central Maine, USA: mineral reactions, fluid transfer, and heat transfer: *Journal of Petrology*, v. 25, no. 4, p. 871-893.

-, 2007, The role of volatile transport by diffusion and dispersion in driving biotite-forming reactions during regional metamorphism of the Gile Mountain Formation, Vermont: *American Mineralogist*, v. 92, no. 8-9, p. 1288-1302.

Fleet, M. E., 2005, XANES spectroscopy of sulfur in earth materials: The Canadian Mineralogist, v. 43, no. 6, p. 1811-1838.

Frey, M., 1987, Low temperature metamorphism, Glasgow, Blackie.

Fuller, M., Cisowski, S., Hart, M., Haston, R., Schmidtke, E., and Jarrard, R., 1988, NRM-IRM(s) Demagnetization Plots - an Aid to the Interpretation of Natural Remanent Magnetization: *Geophysical Research Letters*, v. 15, no. 5, p. 518-521.

Fuller, M., Kidane, T., and Ali, J., 2002, AF demagnetization characteristics of NRM, compared with anhysteretic and saturation isothermal remanence: an aid in the interpretation of NRM: *Physics and Chemistry of the Earth*, v. 27, no. 25-31, p. 1169-1177.

Gellatly, A. M., and Lyons, T. W., 2005, Trace sulfate in mid-Proterozoic carbonates and the sulfur isotope record of biospheric evolution: *Geochimica et Cosmochimica Acta*, v. 69, no. 15, p. 3813-3829.

Gilleaudeau, G. J., and Kah, L. C., 2015, Heterogeneous redox conditions and a shallow chemocline in the Mesoproterozoic ocean: evidence from carbon-sulfur-iron relationships: *Precambrian Research*, v. 257, p. 94-108.

González-Álvarez, I., and Kerrich, R., 2010, REE and HFSE mobility due to protracted flow of basinal brines in the Mesoproterozoic Belt-Purcell Supergroup, Laurentia: *Precambrian Research*, v. 177, no. 3, p. 291-307.

González-Álvarez, I., Kusiak, M. A., and Kerrich, R., 2006, A trace element and chemical Th-U total Pb dating study in the lower Belt-Purcell Supergroup, Western North America: provenance and diagenetic implications: *Chemical Geology*, v. 230, no. 1, p. 140-160.

Graham, G., Hitzman, M. W., and Zieg, J., 2012, Geologic Setting, Sedimentary Architecture, and Paragenesis of the Mesoproterozoic Sediment-Hosted Sheep Creek Cu-Co-Ag Deposit, Helena Embayment, Montana: *Economic Geology*, v. 107, no. 6, p. 1115-1141.

Grey, K., and Williams, I. R., 1990, Problematic bedding-plane markings from the Middle Proterozoic Manganese Subgroup, Bangemall Basin, Western Australia: *Precambrian Research*, v. 46, no. 4, p. 307-327.

Griffith, E. M., and Paytan, A., 2012, Barite in the ocean—occurrence, geochemistry and palaeoceanographic applications: *Sedimentology*, v. 59, no. 6, p. 1817-1835.

Hall, A. J., 1986, Pyrite-pyrrhotine redox reactions in nature: *Mineralogical Magazine*, v. 50, p. 223-229.

Hamilton, J., Bishop, D., Morris, H., and Owens, O., 1982, Geology of the Sullivan orebody, Kimberley, BC, Canada: *Precambrian Sulphide Deposits*, v. 25, p. 597-665.

Hanor, J. S., 2000, Barite–celestine geochemistry and environments of formation: *Reviews in Mineralogy and Geochemistry*, v. 40, no. 1, p. 193-275.

Harrison, J. E., 1972, Precambrian Belt basin of northwestern United States: Its geometry, sedimentation, and copper occurrences: *Geological Society of America Bulletin*, v. 83, no. 5, p. 1215-1240.

Harrison, J. E., Whipple, J. W., Lidke, D. J., Helen, Z., and Miller, R. J., 1998, Geologic map of the western part of the Cut Bank 1 degree by 2 degrees Quadrangle, northwestern Montana, scale 1:250,000.

Heslop, D., Dekkers, M., Kruiver, P., and Van Oorschot, I., 2002, Analysis of isothermal remanent magnetization acquisition curves using the expectation-maximization algorithm: *Geophysical Journal International*, v. 148, no. 1, p. 58-64.

Hoffman, P. F., 1988, Belt basin: a landlocked remnant oceanic basin? (Analogous to the south Caspian Sea and Black Seas). *Geol. Soc. Am. Ann. Mtg. Abst. Prog. 20, A50.*, Geological Society of America Annual Meeting, Abstracts, Volume 20, p. A40.

Hofmann, H. J., Ediacaran enigmas, and puzzles from earlier times, *in* *Proceedings Geological Association of Canada - Mineralogical Association of Canada, Joint Annual Meetings, Abstracts.*, St. Johns, 2001, Volume 26, p. 64-65.

Holland, H. D., 1984, *The chemical evolution of the atmosphere and oceans*, Princeton University Press.

-, 2006, The oxygenation of the atmosphere and oceans: *Philosophical Transactions of the Royal Society B: Biological Sciences*, v. 361, no. 1470, p. 903-915.

Horng, C.-S., and Roberts, A. P., 2006, Authigenic or detrital origin of pyrrhotite in sediments?: Resolving a paleomagnetic conundrum: *Earth and Planetary Science Letters*, v. 241, no. 3, p. 750-762.

Horodyski, R. J., 1982, Problematic bedding-plane markings from the middle Proterozoic Appekunny argillite, Belt Supergroup, northwestern Montana: *Journal of Paleontology*, p. 882-889.

-, 1993, Paleontology of Proterozoic shales and mudstones: examples from the Belt Supergroup, Chuar Group and Pahrump Group, western USA: *Precambrian Research*, v. 61, no. 3, p. 241-278.

Horodyski, R. J., Winston, D., and Whipple, J. W., 1989, Paleontology of the middle Proterozoic belt supergroup, *in* Winston, D., Horodyski, R. J., and Whipple, J. W., eds., *Middle Proterozoic Belt Supergroup, Western Montana: Great Falls, Montana to Spokane, Washington: 28th International Geological Congress, Field Trip Guidebook T334*, p. 7-26.

Hrouda, F., 2003, Indices for numerical characterization of the alteration processes of magnetic minerals taking place during investigation of temperature variation of magnetic susceptibility: *Studia Geophysica et Geodaetica*, v. 47, no. 4, p. 847-861.

Huebschman, R. P., 1973, Correlation of fine carbonaceous bands across a Precambrian stagnant basin: *Journal of Sedimentary Research*, v. 43, no. 3, p. 688-699.

Johnson, H. P., Lowrie, W., and Kent, D. V., 1975, Stability of anhysteretic remanent magnetization in fine and coarse magnetite and maghemite particles: *Geophysical Journal of the Royal Astronomical Society*, v. 41, no. 1, p. 1-10.

Johnson, J. E., Gerpheide, A., Lamb, M. P., and Fischer, W. W., 2014, O<sub>2</sub> constraints from Paleoproterozoic detrital pyrite and uraninite: *Geological Society of America Bulletin*, v. 126, no. 5-6, p. 813-830.

Kendall, B., Creaser, R. A., Gordon, G. W., and Anbar, A. D., 2009, Re–Os and Mo isotope systematics of black shales from the Middle Proterozoic Velkerri and Wolllogorang formations, McArthur Basin, northern Australia: *Geochimica et Cosmochimica Acta*, v. 73, no. 9, p. 2534-2558.

Kirschvink, J. L., Kopp, R. E., Raub, T. D., Baumgartner, C. T., and Holt, J. W., 2008, Rapid, precise, and high-sensitivity acquisition of paleomagnetic and rock-magnetic data: Development of a low-noise automatic sample changing system for superconducting rock magnetometers: *Geochemistry Geophysics Geosystems*, v. 9, no. 5.

Klein, F., Bach, W., Humphris, S. E., Kahl, W.-A., Jöns, N., Moskowitz, B., and Berquó, T. S., 2014, Magnetite in seafloor serpentinite—Some like it hot: *Geology*, v. 42, no. 2, p. 135-138.

Knoll, A. H., Javaux, E. J., Hewitt, D., and Cohen, P., 2006, Eukaryotic organisms in Proterozoic oceans: *Philosophical Transactions of the Royal Society B: Biological Sciences*, v. 361, no. 1470, p. 1023-1038.

Koski, R. A., and Hein, J. R., 2004, Stratiform barite deposits in the Roberts Mountains Allochthon, Nevada: a review of potential analogs in modern sea-floor environments, US Department of the Interior, US Geological Survey Bulletin, 17 p.:

Kozłowski, A., Kakol, Z., Kim, D., Zalecki, R., and Honig, J., 1996, Heat capacity of  $\text{Fe}_{3-\alpha}\text{M}_{\alpha}\text{O}_4$  ( $\text{M} = \text{Zn, Ti}$ ,  $0 \leq \alpha \leq 0.04$ ): *Physical Review B*, v. 54, no. 17, p. 12093.

Larrasoana, J. C., Roberts, A. P., Musgrave, R. J., Gràcia, E., Piñero, E., Vega, M., and Martínez-Ruiz, F., 2007, Diagenetic formation of greigite and pyrrhotite in gas hydrate marine sedimentary systems: *Earth and Planetary Science Letters*, v. 261, no. 3, p. 350-366.

Li, H. Y., and Zhang, S. H., 2005, Detection of Mineralogical Changes in Pyrite Using Measurements of Temperature - Dependence Susceptibilities: *Chinese Journal of Geophysics*, v. 48, no. 6, p. 1454-1461.

Lowrie, W., and Fuller, M., 1971, Alternating field demagnetization characteristics of multidomain thermoremanent magnetization in magnetite: *Journal of Geophysical Research*, v. 76, no. 26, p. 6339-&.

Luepke, J. J., 1999, Geochemical trends in shales of the Belt Supergroup, Northwestern US: a marine model for the evolution of the Mesoproterozoic western Laurentian Margin [M.S. thesis: University Missouri-Columbia, 133 p.

Luepke, J. J., and Lyons, T. W., 2001, Pre-Rodinian (Mesoproterozoic) supercontinental rifting along the western margin of Laurentia: geochemical evidence from the Belt-Purcell Supergroup: *Precambrian Research*, v. 111, no. 1, p. 79-90.

Lyons, T. W., Luepke, J. J., Schreiber, M. E., and Zieg, G. A., 2000, Sulfur geochemical constraints on Mesoproterozoic restricted marine deposition: lower Belt Supergroup, northwestern United States: *Geochimica et Cosmochimica Acta*, v. 64, no. 3, p. 427-437.

Lyons, T. W., and Severmann, S., 2006, A critical look at iron paleoredox proxies: new insights from modern euxinic marine basins: *Geochimica et Cosmochimica Acta*, v. 70, no. 23, p. 5698-5722.



- Maxwell, D., and Hower, J., 1967, High-grade diagenesis and low-grade metamorphism of illite in Precambrian Belt Series: *American Mineralogist*, v. 52, no. 5-6, p. 843-857.
- Minyuk, P., Subbotnikova, T., and Plyashkevich, A., 2011, Measurements of thermal magnetic susceptibility of hematite and goethite: *Izvestiya, Physics of the Solid Earth*, v. 47, no. 9, p. 762-774.
- Minyuk, P., Tyukova, E., Subbotnikova, T., Kazansky, A. Y., and Fedotov, A., 2013, Thermal magnetic susceptibility data on natural iron sulfides of northeastern Russia: *Russian Geology and Geophysics*, v. 54, no. 4, p. 464-474.
- Moreau, M., Ader, M., and Enkin, R., 2005, The magnetization of clay-rich rocks in sedimentary basins: low-temperature experimental formation of magnetic carriers in natural samples: *Earth and Planetary Science Letters*, v. 230, no. 1, p. 193-210.
- Moskowitz, B. M., Jackson, M., and Kissel, C., 1998, Low-temperature magnetic behavior of titanomagnetites: *Earth and Planetary Science Letters*, v. 157, no. 3, p. 141-149.
- Mudge, M. R., Erickson, R. L., Kleinkopf, M. D., and Zartman, R. E., 1968, Reconnaissance geology, geophysics, and geochemistry of the southeastern part of the Lewis and Clark Range, Montana: US Government Print Office.
- O'Reilly, W., 1984, *Rock and Mineral Magnetism*, New York, Chapman and Hall.
- O'Day, P. A., Rivera, N., Root, R., and Carroll, S. A., 2004, X-ray absorption spectroscopic study of Fe reference compounds for the analysis of natural sediments: *American Mineralogist*, v. 89, no. 4, p. 572-585.
- Peters, C., and Dekkers, M., 2003, Selected room temperature magnetic parameters as a function of mineralogy, concentration and grain size: *Physics and Chemistry of the Earth*, v. 28, no. 16, p. 659-667.
- Piatak, N. M., Seal, R. R., Sanzolone, R. F., Lamothe, P. J., Brown, Z., and Adams, M., 2007, Sequential extraction results and mineralogy of mine waste and stream sediments associated with metal mines in Vermont, Maine, and New Zealand: US Geological Survey Open-File Report, v. 1063, p. 34.
- Planavsky, N. J., McGoldrick, P., Scott, C. T., Li, C., Reinhard, C. T., Kelly, A. E., Chu, X., Bekker, A., Love, G. D., and Lyons, T. W., 2011, Widespread iron-rich conditions in the mid-Proterozoic ocean: *Nature*, v. 477, no. 7365, p. 448-451.

Potter, D., and Stephenson, A., 1986, The detection of fine particles of magnetite using anhysteretic and rotational remanent magnetizations: *Geophysical Journal International*, v. 87, no. 2, p. 569-582.

Poulton, S. W., and Canfield, D. E., 2011, Ferruginous conditions: a dominant feature of the ocean through Earth's history: *Elements*, v. 7, no. 2, p. 107-112.

Pratt, B. R., 2001, Oceanography, bathymetry and syndepositional tectonics of a Precambrian intracratonic basin: integrating sediments, storms, earthquakes and tsunamis in the Belt Supergroup (Helena Formation, ca. 1.45 Ga), western North America: *Sedimentary Geology*, v. 141, p. 371-394.

Price, R., 1964, The Precambrian Purcell System in the Rocky Mountains of southern Alberta and British Columbia: *Bulletin of Canadian Petroleum Geology*, v. 12, no. 2, p. 399-426.

Raiswell, R., and Canfield, D. E., 1998, Sources of iron for pyrite formation in marine sediments: *American Journal of Science*, v. 298, no. 3, p. 219-245.

Raub, T., Johnson, S. C., and Raub, T. D., 2012, Rock magnetic detection of the pyrite-to-pyrrhotite reduction: applications to hydrocarbon maturity, mineral resources, and biogeochemistry, American Geophysical Union, Fall Meeting: San Francisco, CA, p. GP34A-08.

Retallack, G. J., Dunn, K. L., and Saxby, J., 2013, Problematic Mesoproterozoic fossil *Horodyskia* from Glacier National Park, Montana, USA: *Precambrian Research*, v. 226, p. 125-142.

Robertson, D., and France, D., 1994, Discrimination of remanence-carrying minerals in mixtures, using isothermal remanent magnetisation acquisition curves: *Physics of the Earth and Planetary Interiors*, v. 82, no. 3, p. 223-234.

Ross, C. P., 1959, Geology of Glacier National Park and the Flathead region, northwestern Montana: US Geological Survey Professional Paper, 2330-7102.

Ross, G. M., and Villeneuve, M., 2003, Provenance of the Mesoproterozoic (1.45 Ga) Belt basin (western North America): Another piece in the pre-Rodinia paleogeographic puzzle: *Geological Society of America Bulletin*, v. 115, no. 10, p. 1191-1217.

Schieber, J., 1989, Pyrite mineralization in microbial mats from the mid-Proterozoic Newland Formation, Belt Supergroup, Montana, USA: *Sedimentary geology*, v. 64, no. 1, p. 79-90.

Sears, J., Chamberlain, K., and Buckley, S., 1998, Structural and U-Pb geochronological evidence for 1.47 Ga rifting in the Belt basin, western Montana: *Canadian Journal of Earth Sciences*, v. 35, no. 4, p. 467-475.

Shannon, R. D., and White, J. R., 1991, The selectivity of a sequential extraction procedure for the determination of iron oxyhydroxides and iron sulfides in lake sediments: *Biogeochemistry*, v. 14, no. 3, p. 193-208.

Shen, Y., Knoll, A. H., and Walter, M. R., 2003, Evidence for low sulphate and anoxia in a mid-Proterozoic marine basin: *Nature*, v. 423, no. 6940, p. 632-635.

Skomurski, F. N., Kerisit, S., and Rosso, K. M., 2010, Structure, charge distribution, and electron hopping dynamics in magnetite ( $\text{Fe}_3\text{O}_4$ )(100) surfaces from first principles: *Geochimica et Cosmochimica Acta*, v. 74, no. 15, p. 4234-4248.

Slack, J., Grenne, T., Bekker, A., Rouxel, O., and Lindberg, P., 2007, Suboxic deep seawater in the late Paleoproterozoic: evidence from hematitic chert and iron formation related to seafloor-hydrothermal sulfide deposits, central Arizona, USA: *Earth and Planetary Science Letters*, v. 255, no. 1, p. 243-256.

Slotznick, S. P., Zieg, J., Webb, S. M., Kirschvink, J. L., and Fischer, W. W., 2015, Iron Mineralogy and Redox Chemistry of the Mesoproterozoic Newland Formation in the Helena Embayment, Belt Supergroup, Montana: *Northwest Geology*, v. 44, p. 55-72.

Snowball, I. F., 1997, The detection of single-domain greigite ( $\text{Fe}_3\text{S}_4$ ) using rotational remanent magnetization (RRM) and the effective gyro field ( $B_g$ ): mineral magnetic and palaeomagnetic applications: *Geophysical Journal International*, v. 130, no. 3, p. 704-716.

Sperling, E., Rooney, A., Hays, L., Sergeev, V., Vorob'eva, N., Sergeeva, N., Selby, D., Johnston, D., and Knoll, A., 2014, Redox heterogeneity of subsurface waters in the Mesoproterozoic ocean: *Geobiology*, v. 12, no. 5, p. 373-386.

Sperling, E. A., Wolock, C. J., Morgan, A. S., Gill, B. C., Kunzmann, M., Halverson, G. P., Macdonald, F. A., Knoll, A. H., and Johnston, D. T., 2015, Statistical analysis of iron geochemical data suggests limited late Proterozoic oxygenation: *Nature*, v. 523, no. 7561, p. 451-454.

Stanley, A., and Davies-Vollum, K., 2000, A Detailed Sedimentary Analysis of the Middle Part of the Grinnell Formation, near Going-to-the-Sun Mountain, Glacier National Park, Montana, National Park Service Investigator's Annual Report 19879.

Stewart, J. H., 1972, Initial deposits in the Cordilleran geosyncline: Evidence of a late Precambrian (< 850 my) continental separation: *Geological Society of America Bulletin*, v. 83, no. 5, p. 1345-1360.

Stüeken, E. E., 2013, A test of the nitrogen-limitation hypothesis for retarded eukaryote radiation: nitrogen isotopes across a Mesoproterozoic basinal profile: *Geochimica et Cosmochimica Acta*, v. 120, p. 121-139.

Suzuki, Y., Kopp, R. E., Kogure, T., Suga, A., Takai, K., Tsuchida, S., Ozaki, N., Endo, K., Hashimoto, J., and Kato, Y., 2006, Sclerite formation in the hydrothermal-vent “scaly-foot” gastropod—possible control of iron sulfide biomineralization by the animal: *Earth and Planetary Science Letters*, v. 242, no. 1, p. 39-50.

Thomson, G. F., 1990, The anomalous demagnetization of pyrrhotite: *Geophysical Journal International*, v. 103, no. 2, p. 425-430.

Vitarello, I., and Van der Voo, R., 1977, Late Hadrynian and Helikian pole positions from the Spokane formation, Montana: *Canadian Journal of Earth Sciences*, v. 14, no. 1, p. 67-73.

Walcott, C. D., 1899, Pre-Cambrian fossiliferous formations: *Geological Society of America Bulletin*, v. 10, no. 1, p. 199-244.

Walter, M., Oehler, J. H., and Oehler, D. Z., 1976, Megascopic algae 1300 million years old from the Belt Supergroup, Montana: a reinterpretation of Walcott's *Helminthoidichnites*: *Journal of Paleontology*, v. 50, p. 872-881.

Walter, M., Rulin, D., and Horodyski, R. J., 1990, Coiled carbonaceous megafossils from the Middle Proterozoic of Jixian (Tianjin) and Montana: *American Journal of Science*, v. 290, p. 133-148.

Weaver, R., Roberts, A. P., and Barker, A. J., 2002, A late diagenetic (syn-folding) magnetization carried by pyrrhotite: implications for paleomagnetic studies from magnetic iron sulphide-bearing sediments: *Earth and Planetary Science Letters*, v. 200, no. 3, p. 371-386.

Webb, S. M., 2005, SIXPACK: A graphical user interface to XAS analysis using IFEFFIT: *Physica Scripta*, v. T115, p. 1011-1014.

-, 2011, The MicroAnalysis Toolkit: X-ray Fluorescence image processing software: *AIP Conference Proceedings*, v. 1365, p. 196-199.

Whipple, J., Binda, P., and Winston, D., *Geologic guide to Glacier National Park, Montana and areas adjacent to Waterton, Alberta. Belt Symposium III, in Proceedings Geologic Guidebook to the Belt-Purcell Supergroup, Glacier*

National Park and Vicinity, Montana and Adjacent Canada. Field Trip Guidebook for the Belt Symposium III. Belt Association, Pocatello, Idaho 1997, p. 125-155.

Whipple, J. W., Connor, J. J., Raup, O. B., and McGimsey, R. G., Preliminary report on the stratigraphy of the Belt Supergroup, Glacier National Park and adjacent Whitefish Range, Montana, *in* Proceedings Northwest Montana and adjacent Canada. In: McBane, JD, Garrison, PB (Eds.), Guidebook, Field Conference and Symposium, Belt Association, Pocatello, Idaho, Montana Geol. Soc. 1984, p. 33-50.

Whipple, J. W., Donatich, A. J., and Williams, H. F., 1992, Geologic Map of Glacier National Park, Montana: US Geological Survey, scale 1:100000.

Wilkin, R., Barnes, H., and Brantley, S., 1996, The size distribution of framboidal pyrite in modern sediments: an indicator of redox conditions: *Geochimica et Cosmochimica Acta*, v. 60, no. 20, p. 3897-3912.

Willis, B., 1902, Stratigraphy and structure, Lewis and Livingston ranges, Montana: Geological Society of America Bulletin, v. 13, no. 1, p. 305-352.

Winston, D., 1986a, Belt supergroup stratigraphic correlation sections, western Montana and adjacent areas, Montana Bureau of Mines and Geology.

Winston, D., 1986b, Sedimentation and Tectonics of the Middle Proterozoic Belt Basin and Their Influence on Phanerozoic Compression and Extension in Western Montana and Northern Idaho: Part II. Northern Rocky Mountains, *in* Peterson, J. A., ed., Paleotectonics and sedimentation in the Rocky Mountain region, United States. American Association of Petroleum Geologists, Memoir 41, p. 87-118.

-, 1986c, Sedimentology of the Ravalli Group, middle Belt carbonate, and Missoula Group, Middle Proterozoic Belt Supergroup, Montana, Idaho and Washington: Belt Supergroup: A guide to Proterozoic rocks of western Montana and adjacent areas: Montana Bureau of Mines and Geology Special Publication, v. 94, p. 85-124.

-, 2007, Revised Stratigraphy and Depositional History of the Helena and Wallace Formations, Mid-Proterozoic Piegan Group, Belt Supergroup Montana and Idaho: SPECIAL PUBLICATION-SEPM, v. 86, p. 65.

Winston, D., 2016, Sheetflood sedimentology of the Middle Proterozoic Revett Formation, Belt Supergroup, Montana, USA: Geological Society of America Special Papers, v. 522.

Winston, D., and Link, P., 1993, Middle Proterozoic rocks of Montana, Idaho and eastern Washington: the Belt Supergroup: Precambrian: Conterminous US: The Geology of North America, v. 2, p. 487-517.

Xu, S., and Dunlop, D. J., 1995, Toward a better understanding of the Lowrie - Fuller test: *Journal of Geophysical Research: Solid Earth* (1978-2012), v. 100, no. B11, p. 22533-22542.

Zhang, C., Paterson, G. A., and Liu, Q., 2012, A new mechanism for the magnetic enhancement of hematite during heating: the role of clay minerals: *Studia Geophysica et Geodaetica*, v. 56, no. 3, p. 845-860.

Zhou, T., Phillips, G. N., Dong, G., and Myers, R. E., 1995, Pyrrhotite in the Witwatersrand gold fields, South Africa: *Economic Geology*, v. 90, no. 8, p. 2361-2369.